Elastic properties and electron transport in InAs nanowires

Dissertation

zur Erlangung des akademischen Grades

Doktor der Naturwissenschaften

an der Fakultät für Physik

der Universität Duisburg-Essen

vorgelegt von

Vadim Migunov

Sarov, Russian Federation

Dezember 2012

Referent: Prof. Dr. Michael Farle

Koreferent: Prof. Dr. Rafal Dunin-Borkowski

Tag der mündlichen Prüfung: 22 Feb. 2013

To my parents, who were always supporting me in my decision to become a physicist.

To my wife, whose presence in my life is invaluable.

Dreams are often most profound
when they seem the most crazy.

Sigmund Freud

Not a computer but Internet may lash a person. The remarkable Russian psychologist Alexei Leontiev said in 1965: ”Too much information leads to the impoverishment of the soul.” These words should be written on each website.

Sergei Kapitsa

Abstract

The electron transport and elastic properties of InAs nanowires grown by chemical vapor deposition on InAs (001) substrate were studied experimentally, in-situ in a transmission electron microscope (TEM). A TEM holder allowing the measurement of a nanoforce while simultaneous imaging nanowire bending was used. Diffraction images from local areas of the wire were recorded to correlate elastic properties with the atomic structure of the nanowires. Another TEM holder allowing the application of electrical bias between the nanowire and an apex of a metallic needle while simultaneous imaging the nanowire in TEM or performing electron holography was used to detect mechanical vibrations in mechanical study or holographical observation of the nanowire inner potential in the electron transport studies. The combination of the scanning probe methods with TEM allows to correlate the measured electric and elastic properties of the nanowires with direct identification of their atomic structure. It was found that the nanowires have different atomic structures and different stacking fault defect densities that impacts critically on the elastic properties and electric transport. The unique methods, that were applied in this work, allowed to obtain dependencies of resistivity and Young's modulus of $\langle 111 \rangle$-oriented InAs nanowires on defect density and diameter. It was found that the higher is the defect density the higher are the resistivity and the Young's modulus. Regarding the resistivity, it was deduced that the stacking faults increase the scattering of the electrons in the nanowire. These findings are consistent with the literature, however, the effect described by the other groups is not so pronounced. This difference can be attributed to the significant incompleteness of the physical models used for the data analysis. Regarding the elastic modulus, there are several mechanisms affecting the elasticity of the nanowires discussed in the thesis. It was found that the lattice distortion due to stacking fault does not affect the Young's modulus significantly. The effect of electron density redistribution is suggested as the main aspect which is responsible for an enhancement of the Young's modulus by up to 200%. This study suggests that both electrical and elastic properties of the InAs nanowires can be tuned by changing the defect density.

Zusammenfassung

Der Elektronentransport und die elastischen Eigenschaften von InAs Nanodrähten, die durch chemische Gasphasenabscheidung auf einem InAs (001) Substrat gewachsen worden sind, wurden experimentell, in-situ in einem Transmissionselektronenmikroskop (TEM) untersucht. Ein TEM-Probenhalter ermöglicht die Messung einer Nanokraft während der gleichzeitigem Abbildung der Biegung eines Nanodrahts. Beugungsbilder aus lokalen Bereichen eines Drahtes wurden aufgezeichnet, um elastische Eigenschaften mit der atomaren Struktur der Nanodrähte zu korrelieren. Ein anderer TEM-Halter erlaubt das Anlegen einer elektrischen Spannung, bei gleichzeitiger Abbildung des Nanodrahts im TEM bzw. der Durchführung von Elektronenholographie. Mit diesem TEM-Halter wurden mechanische Schwingungen sowie in einer Elektronentransportuntersuchung mittels Holographie das innere Potential des Nanodrahts beobachtet. Diese Kombination der Rastersondenmethoden mit einem TEM ermöglicht es, die gemessenen elektrischen und elastischen Eigenschaften der Nanodrähte mit der direkten Identifizierung ihrer atomaren Struktur zu korrelieren. Es wurde festgestellt, dass die Nanodrähte verschiedene atomare Strukturen und verschiedene Stapelfehlerdefektdichten haben, die sich kritisch auf die elastischen und elektrischen Eigenschaften auswirken. Die Methoden, die in dieser Arbeit angewendet wurden, ermöglichen es, Abhängigkeiten des elektrischen Widerstandes und des Elastizitätsmoduls von Defektdichte und Durchmesser von $\langle 111 \rangle$-orientierten InAs-Nanodrähten zu erhalten. Es stellte sich heraus, dass je höher die Defektdichte ist, umso höher sind der Widerstand und der Young-Modulus. Hinsichtlich des Widerstandes wurde gefolgert, dass die Stapelfehler die Streuung der Elektronen im Nanodraht erhöhen. Diese Ergebnisse stimmen mit der Literatur überein, jedoch wird der Effekt durch die anderen Gruppen nicht so ausgeprägt beschrieben. Dieser Unterschied kann auf die nicht hinreichende Kombination und Korrelation der physikalischen Modelle, die für die Datenanalyse verwendet wurden, zurückgeführt werden. Hinsichtlich des Elastizitätsmoduls gibt es verschiedene Mechanismen, die die Elastizität der Nanodrähte beeinflussen und in dieser Dissertation diskutiert werden. Es wurde herausgefunden, dass Gitterverzerrungen aufgrund von Stapelfehlern den Elastizitätsmodul nicht entscheidend beeinflussen. Der Effekt der Umverteilung der Elektronendichte wird als Hauptaspekt vorgeschlagen, der für eine Verstärkung des Young-Moduls von bis zu 200 % verantwortlich ist. Diese Arbeit zeigt, dass sowohl elektrische als auch elastische Eigenschaften der Nanodrähte durch Ändern der Defektdichte eingestellt werden können.

List of Abbreviations

1D	one-dimensional
2D	two-dimensional
2DEG	two-dimensional electron gas
3D tomography	three-dimensional electron tomography
AC	alternating current (or voltage)
AFM	atomic force microscopy
BF	bright field
bond-OLS	bond-orientation-bond-length-bond-strength model
cAFM	conductive atomic force microscopy
CBED	convergent beam electron diffraction
CCD	charge-coupled device
CNT	carbon nanotube
CTF	contrast transfer function
CVD	chemical vapor deposition
DEP	dielectrophoretic deposition
EAM	embedded atom method
ECR	electron counting rule
EDX	energy dispersive X-Ray (spectroscopy)
EDXS	energy dispersive X-Ray spectroscopy
F-d	force-displacement

FEA	finite element analysis (method)
FEG	field emission gun
FFT	fast Fourier transformation
GIF	Gatan image filter
HAADF	high-angle annular dark-field
HR-TEM	high resolution transmission electron microscopy
I-V	current-voltage
InAs	Indium arsenide
IPA	isopropanol (alcohol)
L-J potential	Lennard-Jones potential
MFP	mean free path
MIP	mean inner potential
MR	magnetoresistance
NEMS	nano electromechanical systems
QD	quantum dots
SAED	selected area electron diffraction
SCLC	space charge limited current
SE	secondary electron
SEM	scanning electron microscope
SF	stacking fault
SIRT	simultaneous iterative reconstruction technique
SO	spin-orbit (coupling)
STEM	scanning transmission electron microscopy
STM	scanning tunneling microscopy
TBAs	tertiarybuthylarsin

TEM	transmission electron microscopy (microscope)
TLM	transfer length method
TMIn	trimethylindium
VLS	vapor-liquid-solid
WZ	Wurtzite
ZB	Zinc Blende

Contents

1. Introduction

Recent progress in the fabrication methods of semiconductor nanowires allows to fabricate the nanowires with a very high crystalline quality, high aspect ratios (up to several thousands) and smallest diameters of 3 nm [1]. Vapor-liquid-solid (VLS) growth techniques allow to produce the nanowires combining several different semiconductor materials in either axial or radial heterojunctions (p-n junctions) [2–5]. The possibility to combine materials with a high lattice mismatch (up to 10 % for InAs nanowires grown on silicon substrate [6]) makes the nanowires very attractive for integration into the silicon based electronics. Utilizing catalytic growth mechanisms the nanowires can be positioned precisely in a specially designed arrangement on the substrate or on the prefabricated steps or other structures. Moreover, junctions between the nanowires can be grown by deposition of additional catalytic particles at the side facets of the nanowires and repeating the synthesis [7]. Recent development of several temperature syntheses, supply interruption and impurity doping processes allow to control the planar defect formation in the nanowires creating either defect free wires or perfect super lattices which can be used to tune the material properties [8–10].

The described advantage and the corresponding low cost of the nanowire production and their low electrical power consumption make semiconductor nanowires very attractive for applications in both: electronic circuit interconnection and electronic functional elements. The nanowires can be used to build high efficiency field effect transistors [11, 12], single electron transistors [13], cross-bar electrical switches [14] and even nanoprocessors[1] [15]. Due to high surface-to-volume ratios the nanowires deliver high efficiency in photovoltaic [16], and bio- and chemical sensor applications [17]. Moreover, different kinds of optoelectronic, electrochemical, biological, and electromechanical nanowire devices have successfully demonstrated their high performance and the advantage of nanoscale miniaturization.

From a fundamental physics point of view the nanowires represent one-dimensional (1D) nanostructures which is a very attractive system to study size effect on electron transport or mechanical properties. They allow to access such phenomenas as: quantized or ballistic conductivity [12], Coulomb blockade [18], single electron tunneling [13], metal/insulator transitions [19]. The nanowires can have atomic structures or crystallographic defects which do not exist in bulk materials. Currently, new research projects, as well as this thesis, are directed at a better

[1] A nanoprocessor is a logical processing unit constructed from intrinsically nanoscale building blocks [15].

quantitative understanding of the role of these defects for which sometimes observed dramatic changes of electrical and mechanical properties in nanowires compared to bulk properties.

Due to their narrow direct band gap (0.354 eV at 300 K), high carrier concentration and carrier mobility, low effective mass of electron, InAs nanowires are especially interesting for high frequency [20] and low power operating devices [21]. The electronic properties of the nanowires were intensively studied during the last two decades. In most of the studies the field effect transistor (FET) geometry is utilized to extract transport coefficients [11, 22]. However, the reproducibility of the result is highly affected by the surface states in the nanowires and variations in their atomic structure (i.e. Zinc Blende / Wurtzite polymorphism). Regarding the surface states, InAs is the only III-V semiconductor which has natural electron accumulation layer at the surface, thus, the transport in the nanowires is highly dominated by the surface states. The studies of the size dependent transport in the nanowires have been inconclusive because the observed size correlations have either a huge error [22] or other issues distorting the results (e.g. tapering of the nanowires, which drastically impacts the reliability of the data analysis) [23]. Also, the formation of planar defects in the nanowires affects the properties of the wires and, thus, the device reproducibility [11]. The impact of the defects on the electron transport was studied by several groups [12, 18, 24]. The last two groups have found a small decrease of the electron mobility for the nanowires with the defects. However, this findings are not consistent with the high degree of degeneracy of the electrical properties of the nanowires observed in those studies.

In this PhD work electron transport and elastic properties of InAs nanowires were studied using novel in-situ (TEM) techniques. The electron transport in the nanowires was measured using a two-point contact method with simultaneous structural characterization of the nanowire in the TEM. An increase of the nanowire resistance with increasing stacking fault density was observed. To investigate its origin electron holography combined with electrical current application was performed in-situ in the TEM. This method allows to directly observe the electrical potential variations inside a nanowire with nanometer or even sub-nanometer resolution when the current is flowing. However, the potential variations could not be detected in this experiment. This indicates that either the variations are too small (smaller than 0.15 V, when 2 V is applied to a nanowire) to be detected using this technique or they do not exist. Since no charge separation was detected at the stacking faults, these findings contradict the suggestion of Dayeh [12] that the stacking faults possess relatively high spontaneous polarization. As expected I can confirm that the increase of electron scattering due to stacking faults decreases the electron mobility. This effect was not confirmed by FET measurements [12, 23] either due to absence of the direct correlation of the transport measurements with the crystal structure [2] or because of the

[2] In these references the crystal structure data (i.e. information about the presence of the defects) was taken from the TEM investigations of the nanowire sample. However, the nanowires grown at the same conditions are not usually identical.

uncertainties in the data analysis of the FET experiment utilizing the back gate geometry [12].

The studies to correlate directly elastic and transport properties of semiconductor nanowires with their atomic structure has attracted up to now only limited interest of researchers. However, this is an important aspect, since the nanowires are very good candidates for applications in nano electromechanical systems (NEMS) due to their high quality factors (> 1000) and super elasticity [25]. There are several examples: nanoresonators for acceleration and mass sensors; nanotransducers for energy conversations; nanoactuators for mechanical or optical switching. Moreover, the elastic strain changes electrical and optic properties of the nanowires, that is of the devices. The knowledge of the elastic properties of the nanowires might be significant for designing new applications.

From a fundamental perspective, the nanowires give access to elastic properties at the nanoscale. One of the first and most important question is if the surface is elastically stiffer or softer than the bulk. Some theoretical studies suggested that the surface is softer than the bulk [26–28], however, others suggested that the surface is stiffer than the bulk [29–31]. Also the experimental works do not agree. One group of studies is showing a decrease of Young's modulus with the nanowire size [32, 33], and the other group is showing an increase [25, 34, 35]. Both theoretical and experimental studies will be discussed in details in section 2.3.

As mentioned above, the InAs nanowire is usually full of stacking fault defects. There are only very few studies that investigate elastic properties of semiconductor nanowires with this type of defects [33, 36]. Those works, however, are far from answering the question, how the stacking faults affect the elastic properties of the nanowires. This question is addressed in this thesis, and it is shown that the stacking faults can be used to tune the elastic properties.

The in-situ TEM methods were used for the electromechanical investigation and the analysis of the bending behavior of the InAs nanowires. My investigation suggests that:

- the nanowire electromechanical resonators have high quality factors;
- indeed, the defects play an important role in the enhancement of Young's modulus of the nanowires by up to 200%;
- the electric and elastic properties of the nanowires may have a direct link to each other (see chapter 5 for the details).

Furthermore, a new method to directly visualize and quantify the elastic strain when a force applied to the nanowires will be demonstrated.

2. Theoretical background: Elastic properties of semiconductors

The present chapter contains: a) an introduction to elastic theory; b) fundamentals of mechanical vibrations, which will be used for analyses of the experimental data; c) a review of elastic properties of nanoobjects.

2.1. Classical elasticity theory

Elasticity is the property of a material to return to its original shape after the force (stress) causing a deformation is removed. The origin of elasticity is the small change (< 1-3 % typically) of the interatomic distances which causes small restoring interatomic forces. As long as the atomic arrangement is not changed, the atoms can return to their original unstrained equilibrium position after the external force (load) is removed. Depending on the nature of the interatomic forces, the elastic properties of materials can change significantly [29, 37]. We can divide the forces in two types: i) van der Waals forces or ii) the forces which are the result of (partial) electron redistribution between binded atoms. In the first case of interaction of a pair of the same neutral atoms, the forces can be well approximated by Lennard-Jones potential (L-J potential) . This types of bonds will be weaker than the other once (ionic, covalent, metalic). Since ionic and covalent bonds are directional, the additional (to crystaline) anisotropy of the elastic properties will apear. Opposite to ionic and covalent bonds, metalic bonds are non-directional and normally weaker than the first two.Assuming a linear response to a "small" elastic deformations (infinitesimal[1] strains) has been found to be a good approximation for all types of chemical bonds. For example, figure 2.1 *a* shows two Lennard-Jones potentials V for different depths of the potential well ϵ, according to the equation:

$$V = \epsilon \left[\left(\frac{r_m}{r} \right)^{12} - 2 \left(\frac{r_m}{r} \right)^{6} \right], \tag{2.1}$$

where r is the distance between the atoms and r_m is its equilibrium value. The first derivative of the potential with minus sign is equal to the force acting on the atom (figure 2.1 *b*). One sees

[1] ones which are so small that can not be measured with any means.

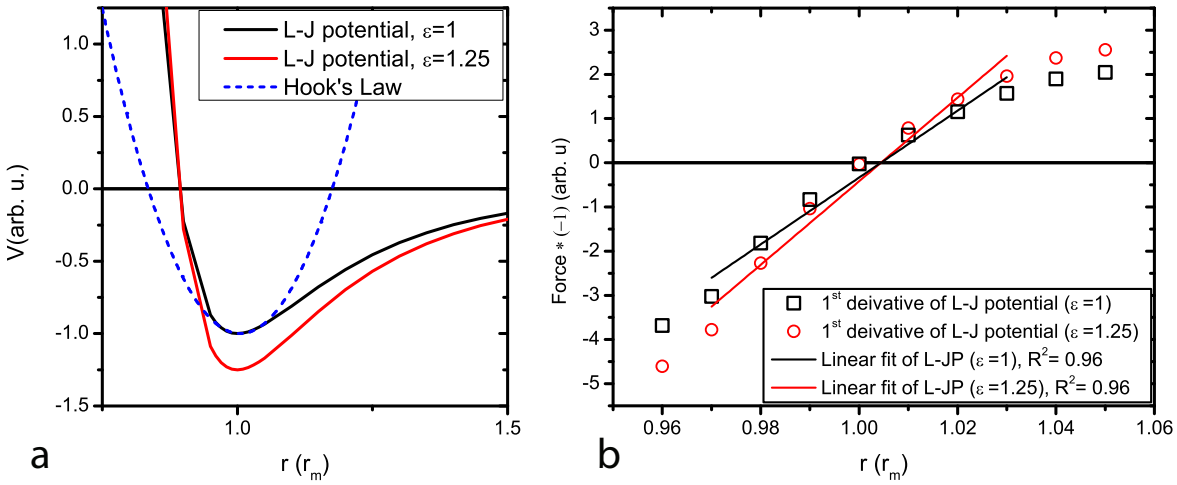

Figure 2.1.: (a)L-J potential (solid lines) for different values of the parameter ϵ. A parabolic fit according to Hook's law for the L-J potential ($\epsilon = 1$), fitting it close to energetic minimum, is shown with the blue dashed line. Corresponding derivatives (b) of the L-J potential representing interatomic force (black squares and red circles). Linear fits of the force are shown with the solid lines which represent Hook's law.

that the linear relation fits the force quite well if the relative change of the interatomic distance does not exceed a few percent. It is important to notice that the deeper is the potential well the higher is the spring constant k (slope of the linear fits in figure 2.1 *b*). Thus the response to the forces, which cause small deformations, can be approximated by Hook's law. The present section deals with the linear elastic theory only. The non-linear theory of elasticity is described elsewhere [38, 39].

The linear elastic theory can be applied only on the length scales greater than interatomic distances, that is for continuous body. There are two main characteristics of a deformation process: stress and strain. Stress is a measure of internal forces acting in the deformed body. Strain is a normalized measure of the body deformation.

Let us consider a solid body (figure 2.2) which is deformed by an external force. The deformation will result in internal forces in the body which in thermodynamic equilibrium should compensate each other. Stress vector $\vec{T}^{(n)}$ in a point *P* upon a surface *AB* with normal vector $\vec{n}$ can be defined as $T_i^{(n)} = \frac{dF_i}{dS}$, where $\vec{dF}$ is a force acting on element of area dS around point *P*. The stress vector does not depend on selection of the plane *AB* (it is a statement of Cauchy's postulate [40]) and, thus, equal to the stress vector acting on the other surface of the plane *AB* ($\vec{T}^{(n)} = -\vec{T}^{(-n)}$). The general consequence of Cauchy's postulate is Cauchy's stress theorem which states on existence of second order symmetric stress tensor $\hat{\sigma}$:

$$\vec{T}^{(n)} = \hat{\sigma} \cdot \vec{n}, \text{ where } \hat{\sigma} = \begin{bmatrix} \sigma_{11} & \sigma_{12} & \sigma_{13} \\ \sigma_{21} & \sigma_{22} & \sigma_{23} \\ \sigma_{31} & \sigma_{32} & \sigma_{33} \end{bmatrix} \text{ and } \sigma_{ij} = \sigma_{ji} \tag{2.2}$$

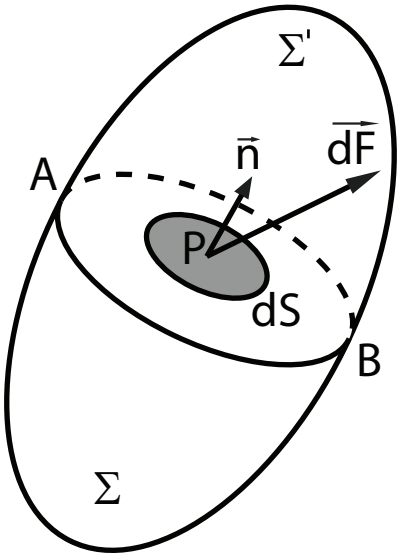

Figure 2.2.: A schematic representation of a deformed body which is in thermodynamic equilibrium. Plane AB divides it in two parts Σ and Σ'. An element of area of a surface AB around point P is denoted with dS, $\vec{n}$ is its normal vector and $\vec{dF}$ is an internal force acting in point P.

Since the tensor can be diagonalized, the Eigenvalues of the stress vector can be found as the diagonal elements of the stress tensor and they are equal to so called principal stress. Thus, there always exist three planes (principal planes) where the stress (principal stress) acts orthogonal to them.

To define the strain in a body one should associate position of each point of the body with its radius vector $\vec{r}$ with coordinates x_i (i = 1, 2, 3). During the deformation each point is shifted and its new position is defined by the radius vector $\vec{r}'$ with coordinates x_i'. The deformation vector $\vec{u}$ can be defined as: $u_i = x_i' - x_i$ [41]. During the deformation the distance dl between two infinitely close points of the body changes in the following way:

$$dl = \sqrt{\sum_{i=1}^{3} dx_i^2}, \text{ and } dl' = \sqrt{\sum_{i=1}^{3} dx_i'^2} \text{ or shortly:} \tag{2.3}$$

$$dl^2 = dx_i^2, \text{ and } dl'^2 = dx_i' = (dx_i + du_i)^2 \tag{2.4}$$

where dx_i and dx_i' are coordinates of radius vectors between the points before and after deformation respectively, $u_i = dx_i' - dx_i$ are coordinates of the deformation vector [41]. Substituting $du_i = \frac{\partial u_i}{\partial x_k} dx_k$ one ends up with:

$$dl'^2 = dl^2 + 2\frac{\partial u_i}{\partial x_k} dx_i dx_k + \frac{\partial u_i}{\partial x_k}\frac{\partial u_i}{\partial x_l} dx_k dx_l \tag{2.5}$$

Since in the second term of the equation indices i and k are dummy indices we can rewrite the

term in decisive symmetric form [41]:

$$\left(\frac{\partial u_i}{\partial x_k} + \frac{\partial u_k}{\partial x_i}\right) dx_i dx_k$$

Interchanging i and l in the third term of equation 2.5 one ends with the following [41]:

$$dl'^2 = dl^2 + 2u_{ik}dx_i dx_k, \text{ where} \tag{2.6}$$

$$u_{ik} = \frac{1}{2}\left(\frac{\partial u_i}{\partial x_k} + \frac{\partial u_k}{\partial x_i} + \frac{\partial u_l}{\partial x_i}\frac{\partial u_l}{\partial x_k}\right) \tag{2.7}$$

The tensor $\hat{u}$ is defined as symmetric therefore it can be diagonalized. It is not difficult to show that principle components of the tensor are equal to the relative length change along the principal axes [41]. Thus, the principal components represent the strain in the body. Since we deal with infinitesimal deformations the second-order infinitesimal in equation 2.7 can be neglected. Thus, the strain tensor $\hat{\epsilon}$ can be defined as:

$$\hat{\epsilon} = \begin{bmatrix} \epsilon_{11} & \epsilon_{12} & \epsilon_{13} \\ \epsilon_{21} & \epsilon_{22} & \epsilon_{23} \\ \epsilon_{31} & \epsilon_{32} & \epsilon_{33} \end{bmatrix} = \begin{bmatrix} \epsilon_{11} & \frac{1}{2}\gamma_{12} & \frac{1}{2}\gamma_{13} \\ \frac{1}{2}\gamma_{21} & \epsilon_{22} & \frac{1}{2}\gamma_{23} \\ \frac{1}{2}\gamma_{31} & \frac{1}{2}\gamma_{32} & \epsilon_{33} \end{bmatrix}, \text{ where } \epsilon_{ik} = \frac{1}{2}\left(\frac{\partial u_i}{\partial x_k} + \frac{\partial u_k}{\partial x_i}\right) \tag{2.8}$$

One should mention here, that **the linear elastic theory does not work in the materials with reduced dimensionality**, since the infinitesimal u_i results in the finite partial derivative by the coordinate of the reduced dimension. Thus, the response of a such body to the "small" deformation will not be linear.

As it was shown in the beginning of the section the Hook's Law is a good approximation of the stress-strain relation of the isotropic body. More general, the free energy of elastically deformed crystal can be written as [41]:

$$F = \frac{1}{2}C_{iklm}\epsilon_{ik}\epsilon_{lm}, \tag{2.9}$$

where C_{iklm} is components of the stiffness tensor. Since $\sigma_{ik} = \frac{\partial F}{\partial \epsilon_{ik}}$ [41], the stress-strain relation for anisotropic case can be written in the following way:

$$\sigma_{ik} = C_{iklm}\epsilon_{lm}, \text{ or } \hat{\sigma} = \hat{C} : \hat{\epsilon} \tag{2.10}$$

Symmetry of both stress and strain tensors allow to make a transition to Voigt notations using the following index transformation:

ij	=	11	22	33	23,32	13,31	12, 21
$\Downarrow$		$\Downarrow$	$\Downarrow$	$\Downarrow$	$\Downarrow$	$\Downarrow$	$\Downarrow$
$\alpha\beta$	=	1	2	3	4	5	6

In the Voigt notations the stress and the strain tensors will be transformed into vectors, and the rank 4 stiffness tensor transforms into rank 2, 6x6 tensor. Depending on the symmetry of the matter the stiffness tensor can have different amount of independent components. For cubic crystals the stiffness tensor is symmetric and has only three independent components:

$$\hat{C}_{cubic} = \begin{bmatrix} C_{11} & C_{12} & C_{12} & 0 & 0 & 0 \\ C_{12} & C_{11} & C_{12} & 0 & 0 & 0 \\ C_{12} & C_{12} & C_{11} & 0 & 0 & 0 \\ 0 & 0 & 0 & C_{44} & 0 & 0 \\ 0 & 0 & 0 & 0 & C_{44} & 0 \\ 0 & 0 & 0 & 0 & 0 & C_{44} \end{bmatrix} \tag{2.11}$$

Applying an uniaxial force along [111] direction of cubic crystal, the stress and the strain can be written as:

$$\vec{\sigma}_{[111]} = \begin{bmatrix} \sigma \\ 0 \\ 0 \\ 0 \\ 0 \\ 0 \end{bmatrix}, \text{ and } \vec{\epsilon}_{[111]} = \begin{bmatrix} \epsilon_1 \\ \epsilon_2 \\ \epsilon_3 \\ \epsilon_4 \\ \epsilon_5 \\ \epsilon_6 \end{bmatrix} = \hat{C}^{-1}_{[111]} \cdot \vec{\sigma}_{[111]}, \tag{2.12}$$

where x-axis of the system coordinate oriented along [111] direction and the y-axis along [1-10] direction. Thus, the stiffness tensor $\hat{C}_{cubic}$ in equation 2.11 should be rotated. Since the Young's modulus can be defined as coefficient of proportionality between uniaxial strain and uniaxial stress and disregarding calculation, the following formula represents Young's modulus of the crystal in [111] direction:

$$E_{[111]} = \frac{\sigma}{\epsilon_1} = \frac{3C_{44}(C_{11} + 2C_{12})}{C_{11} + 2C_{12} + C_{44}} \tag{2.13}$$

2.2. Fundamentals of mechanical vibrations

Modeling of an oscillatory body utilizes rigid body mechanics. The equations of motion can be derived using Newton Laws. Basically the equations of motion should be written for each point of the body, however, the simplification of the modeling can be done if the body is considered as different subsystems in which points of the body acting as a one point. The interaction of the subsystems and their response to the external stimuli will be the main subject of the modeling.

The excitations of a system can be divided in two classes: i) initial excitations and ii) applied force or applied momentum excitations. The first one is an initial displacement or initial velocity which has a system in the moment when the time t is equal to zero. Since in all other moments ($t > 0$) the system responses freely, the vibrational movement in this case is called free vibrations,

and can be described by the homogeneous equation of motion (for conservative and dissipative system):

$$M\ddot{x}(t) + f_c(\dot{x}(t)) + f_k(x(t)) = 0, \tag{2.14}$$

where x is displacement of the system from the equilibrium position, M is effective mass of the system, f_c and f_k are the functions defining nature of viscosity and response to deformations respectively[2]. When there is a force $F(t)$ acting on the system the oscillatory movement is called forced vibrations and the equation of the motion will be non-homogeneous:

$$M\ddot{x}(t) + cf_c(\dot{x}(t)) + kf_k(x(t)) = F(t). \tag{2.15}$$

The system response $x(t)$ to the excitations $F(t)$ depends on the nature of excitations and on the system characteristics. All excitations can be deterministic or non-deterministic. Disregarding initial excitations, other deterministic excitations can be divided in two classes: periodic and arbitrary (non-periodic) excitations. Among periodic excitations, the most interesting for us are harmonic excitations. In this case the force (or moment) is proportional to the combination of trigonometric functions $sin(\omega t)$ and $cos(\omega t)$. Any complex harmonic excitation can be represented as a Fourier series where each harmonic function is an integer multiple of the lowest frequency, which is called **fundamental frequency** [42]. The main system characteristic is its linearity or non-linearity. In the case of the linear systems the functions $f_c(\dot{x}(t))$ and $f_k(x(t))$ are linear and equal to $c\dot{x}(t)$ and $kx(t)$ respectively, where c is a coefficient of viscous damping and k is an effective spring constant. As it was shown in the previous section, the linearity of the system can be consequence of the smallness of the motion of the system, in particular of the terms $\dot{x}(t)$ and $x(t)$. In linear systems the response to the combination of individual excitations is a superposition of individual responses to each excitation (superposition principle) [42]. Thus the response to the excitation F_1 and F_2 can be written as:

$$x(t) = c_1x_1(t) + c_2x_2(t), \tag{2.16}$$

where $x_1(t)$ and $x_2(t)$ are responses to excitations F_1 and F_2 respectively, c_1 and c_2 are constants [42].

In equations 2.14 and 2.15 functions f_c and f_k are time independent. Thus the system response to the periodical excitation will not depend on time. This type of systems called **time-invariant systems**. In general there exist time-varying systems which can be modeled using $f_c(\dot{x}(t), t)$ and $f_k(x(t), t)$ functions. It is not difficult to prove that the response of linear time-invariant system to a harmonic excitation is harmonic as well. Let us consider a single degree

[2]Being more precise, the equations 2.14 an 2.15 are written for a system with a single degree of freedom. In general case such an equation should be written for each degree of freedom.

of freedom linear time invariant system under harmonic exciting force:

$$F(t) = kf(t) = kAe^{i\omega t}, \tag{2.17}$$

where ω is the excitation frequency. Since the system is linear equation 2.15 can be rewritten to the following:

$$m\ddot{x}(t) + c\dot{x}(t) + kx(t) = F(t). \tag{2.18}$$

Replacing c and k with the viscous damping factor $\zeta = c/(2\omega_n m)$ and natural frequency $\omega_n = \sqrt{k/m}$ we end up with [42]:

$$\ddot{x}(t) + 2\zeta\omega_n\dot{x}(t) + \omega_n^2 x(t) = \omega_n^2 Ae^{i\omega t}. \tag{2.19}$$

Since the response of the linear system to harmonic excitation is harmonic, we search the solution in the form of $x(t) = X(i\omega)e^{i\omega t}$":

$$(\omega_n^2 - \omega^2 + i2\zeta\omega\omega_n)X(i\omega)e^{i\omega t} = \omega_n^2 Ae^{i\omega t}, \text{ and thus:} \tag{2.20}$$

$$X(i\omega) = \frac{\omega_n^2 A}{\omega_n^2 - \omega^2 + i2\zeta\omega\omega_n} = \frac{A}{1 - (\omega/\omega_n)^2 + i2\zeta\omega/\omega_n}. \tag{2.21}$$

For the convenience the non-dimensional **frequency response** function can be introduced [42]:

$$G(i\omega) = \frac{X(i\omega)}{A} = \frac{1}{1 - (\omega/\omega_n)^2 + i2\zeta\omega/\omega_n}, \text{ hence:} \tag{2.22}$$

$$x(t) = AG(i\omega)e^{i\omega t}, \text{ or:} \tag{2.23}$$

$$x(t) = A\,|G(i\omega)|\,e^{(i\omega t - \phi(\omega))}, \text{ where} \tag{2.24}$$

$$\phi(\omega) = arctan\left(\frac{-\mathrm{Im}G(i\omega)}{\mathrm{Re}G(i\omega)}\right) \tag{2.25}$$

Obviously, the magnitude of the frequency response $|G(i\omega)|$ determines the amplitude of the system response to the harmonic excitations. Figure 2.3 shows amplitude-frequency response of the system to harmonic excitations for different values of the parameter ζ. When the excitation frequency approaches the natural frequency of the system, the resonance vibrations take place. The hight of the resonance and hence the quality factor Q increase with the decrease of the damping. The hight of the maxima can be found as [42]:

$$|G(i\omega)|_{max} = \frac{1}{2\zeta\sqrt{1-\zeta^2}} \tag{2.26}$$

Since quality factor Q is a two pi multiplied by the relation between energy stored in the oscillator to energy dissipated in the cycle for the low damping the Q-factor can be written as

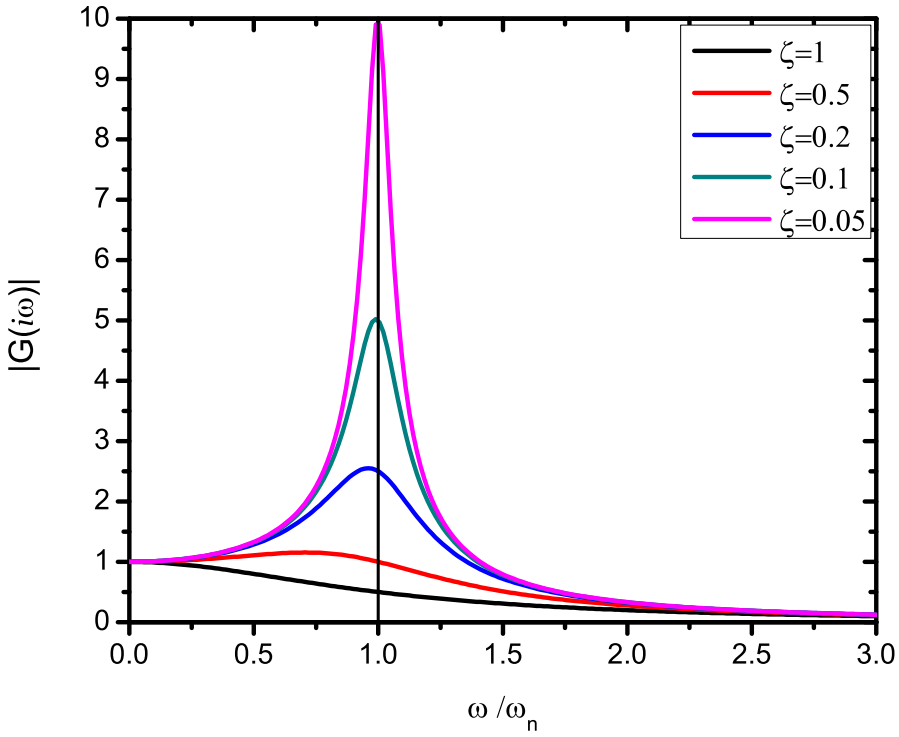

Figure 2.3.: Dependence of the magnitude of the frequency response on the excitation frequency. Different curves correspond to different values of the damping parameter ζ (see legend).

[42]:

$$Q \cong |G(i\omega)|_{max} =\cong \frac{1}{2\zeta}. \tag{2.27}$$

Here we can conclude that for high quality factors ($Q \gg 1$)the vibrations of a system can be approximated as undamped and, thus, the resonance frequency can be approximated by the natural frequency of the system (see figure 2.3).

Let us now consider a bending vibration of an elastic beam which is shown in figure 2.4. The beam has uniform cross section which area is A and the second moment of inertia I upon the axis normal to the sketch plane. The deferential element of the beam is shown in figure 2.4 *b*. It suffers from bending moment $M(x,t)$ and shearing force $Q(x,t)$. We restrict the model of the beam to the following assumptions:

- the rotation of the differential element is small compared with the translational movement;
- the angular distortion because of shear deformation, compared to bending deformation, can be neglected;
- the aspect ratio of the beam is relatively large (> 10 [42]);
- the deformations are small enough that the beam responds linearly;
- the elastic moduli for tensile and contractive deformations are equal.

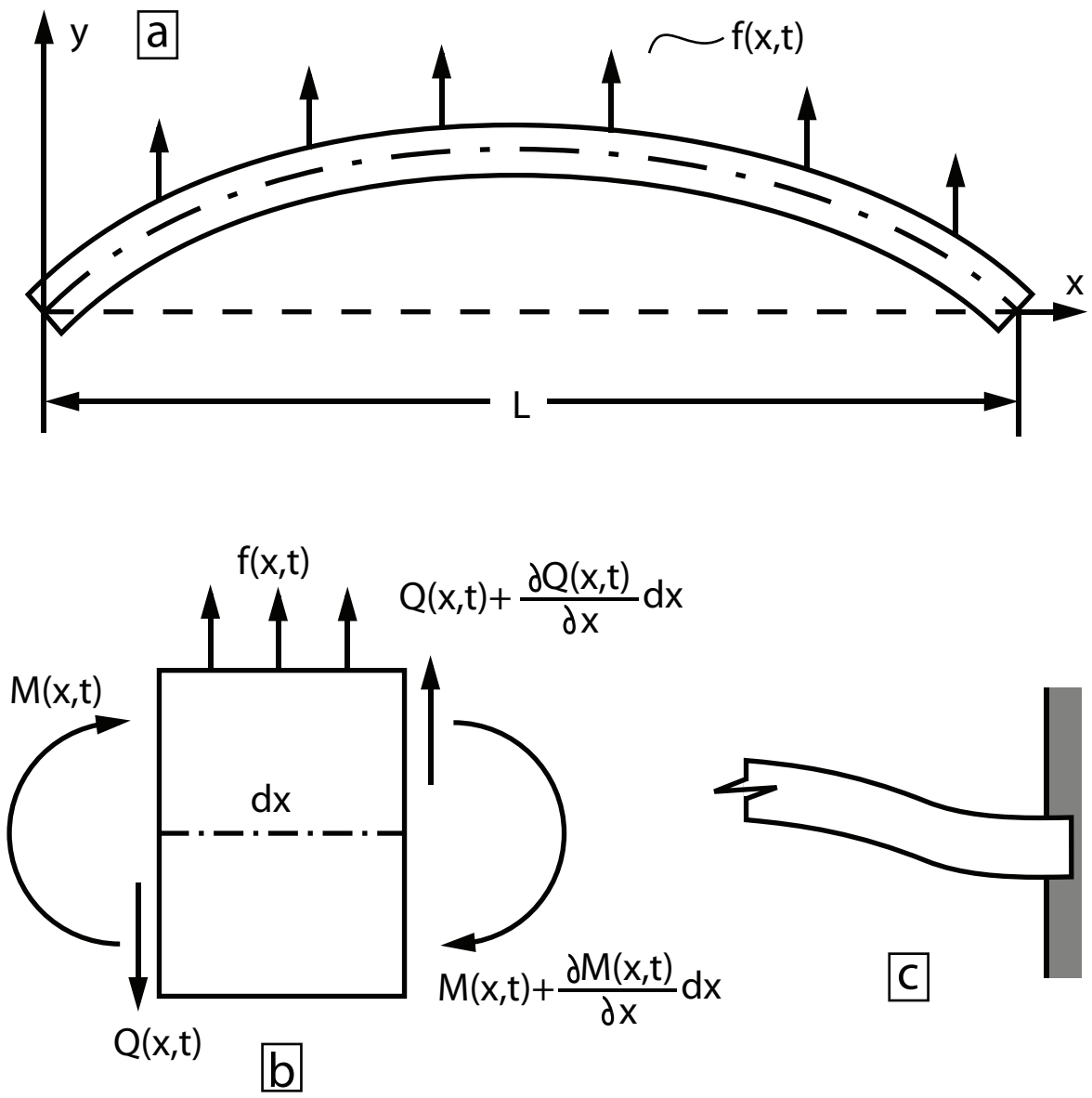

Figure 2.4.: (a) Scheme of vibrational bending of a beam (adopted from [42]). (b) A cross sectional view of the beam element (adopted from [42]). (c) Scheme representing geometrical boundary conditions of the one end clamped beam.

Within the described model the Euler-Bernoulli beam theory can be applied, thus, the Euler-Lagrange equation represents the vibrations of the beam [43]:

$$-\frac{\partial^2}{\partial x^2}\left(EI(x)\frac{\partial^2 y(x,t)}{\partial x^2}\right)+f(x,t)=\rho(x)A(x)\frac{\partial^2 y(x,t)}{\partial t^2}, 0<x<L, \tag{2.28}$$

where x and y are coordinates of the deferential element, E is its Young's modulus, ρ is its mass density. Since the assumption of a homogeneous beam was made, the following terms can be reduced to constants: $I(x)=I$, $\rho(x)=\rho$ and $A(x)=A$. In the following we consider a one end clamped beam (figure 2.4 *c*), therefore the geometric boundary conditions can be formulated as:

$$y(0,t)=0, \text{ and } \left.\frac{\partial y(x,t)}{\partial x}\right|_{x=0}=0 \tag{2.29}$$

Considering free vibrations of the beam ($f(x,t)$=0 in equation 2.28) the solution for natural frequency of i-th harmonic is given by:

$$f_i=\frac{\omega_i}{2\pi}=\frac{\beta_i^2}{2\pi L^2}\sqrt{\frac{EI}{\rho A}}, \tag{2.30}$$

where β_i is a constant which is equal to 1.875 for the 1st harmonic.

The forced vibrations of the beam at frequencies around the natural frequency can be described using the theory of forced vibrations presented above. For example, one can use equation 2.24 to describe qualitatively the response of the beam end.

2.3. Elastic properties of nanoscaled objects

The elastic theory presented in section 2.1 works well for the volume materials. In this section I arise a question how the elastic properties change in nanoscaled materials. There are several reasons, why the classical elastic theory can not be applied to nanostructures:

- Main assumption of classic elastic theory is that deforming body is continuous, the discrete (atomic) structure of the body is neglected. When the body dimensions are comparable with interatomic distances a discrete theory should be developed to describe the elastic behavior.

- A lower coordination at the surface results in surface tension forces, which can be neglected in case of bulk material but should be taken into account for the nanomaterials. In materials with reduced dimensionality surface effects can play a dominative role. Furthermore, strain $\epsilon_{ik}=\frac{1}{2}\left(\frac{\partial u_i}{\partial x_k}+\frac{\partial u_k}{\partial x_i}\right)$ can not be defined for the material reduced in dimension k for example.

- Elastic properties are sensitive to atomic structure. Some structural transitions occur only in nanomaterials.

- Since the nature of interatomic forces can change in nanostructures, their elastic properties may also be affected.

It is possible to build a semicontinuum model as it was done by C. T. Sun and coworkers [26]. The model describes a nanoplate material (thin film) continuous in lateral x and y and discrete along the plate normal in z direction (figure 2.5 *a*). The atoms in the model are considered as non-deformable balls connected with ideal elastic springs. The atomic positions are defined by the integers i, j and l in x, y and z directions respectively. Than the displacements u, v and w of the atoms in layer l can be written as discrete functions and substituted by continuous functions of x_i and y_j [26]:

$$u_{i,j}^{(l)} = u^{(l)}(x_i, y_j), \tag{2.31}$$

$$v_{i,j}^{(l)} = v^{(l)}(x_i, y_j), \tag{2.32}$$

$$w_{i,j}^{(l)} = w^{(l)}(x_i, y_j). \tag{2.33}$$

The corresponding strain than can be formulated as [26]:

$$\epsilon_{xx}^{(l)} = \frac{\partial u^{(l)}}{\partial x}, \text{ and } \gamma_{xy}^{(l)} = \frac{\partial u^{(l)}}{\partial y} + \frac{\partial v^{(l)}}{\partial x}, \tag{2.34}$$

$$\epsilon_{yy}^{(l)} = \frac{\partial v^{(l)}}{\partial y}, \text{ and } \gamma_{yz}^{(l)} = \frac{\partial w^{(l)}}{\partial y} + \frac{v^{(l+1)} - v^{(l)}}{a}, \tag{2.35}$$

$$\epsilon_{zz}^{(l)} = \frac{w^{(l+1)} - w^{(l)}}{a}, \text{ and } \gamma_{xz}^{(l)} = \frac{\partial w^{(l)}}{\partial x} + \frac{u^{(l+1)} - u^{(l)}}{a}, \tag{2.36}$$

where a is a lattice spacing in z direction. Implementing strain energy density function W the authors find Young's modulus in x direction as $E = \sigma_{xx}/\epsilon_{xx}$, where $\sigma_{xx} = \partial W/\partial \epsilon_{xx}$ [26]. Figure 2.5 *b* shows dependence of Young's modulus on the atomic layer number in z direction. The Young's modulus decreases at the surface, however, the effect is noticeable only for the plate with thickness of less than 10 atomic layers. For lager materials one can approximate the surface contribution using a rule of the effective stiffness constant.

Another interesting study [30] compares Young's modulus of copper film obtained by *ab-inito* simulations based on Lennard-Jones (L-J) potential and embedded atom method[3] (EAM) potential. The model build by the authors is fully discrete. The simulations based on the L-J potential (figure 2.6 *a*, dash-dotted line) shows the same trend for the Young's modulus as in semicontinuum model described above (figure 2.5 *b*). However, the result obtained using the

[3] It is a method which considers each atom as it is embedded in a host matrix of atoms (with their electrons). The potential consists of the pair interaction potential and a potential which is a function of electron density.

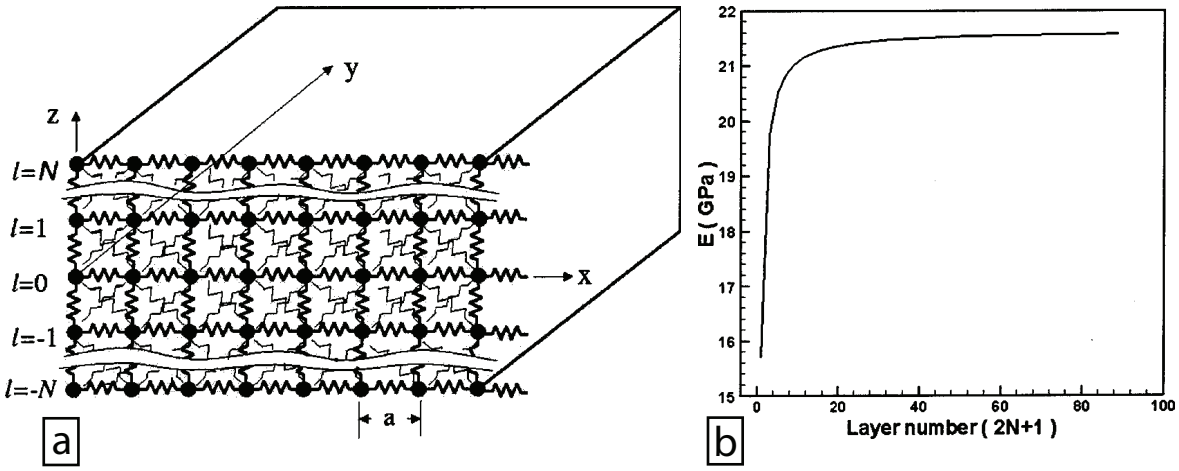

Figure 2.5.: (a) Model of nanoplate material with a cubic structure: black balls represent atoms, springs between balls represent atomic bond. The model is discontinuous in x and y directions and has $2N$+1 atomic layers in z direction, which numbers are denoted with l (adopted from [26]). (b) Dependence of Young's modulus on number of layers $2N$+1 (adopted from [26]).

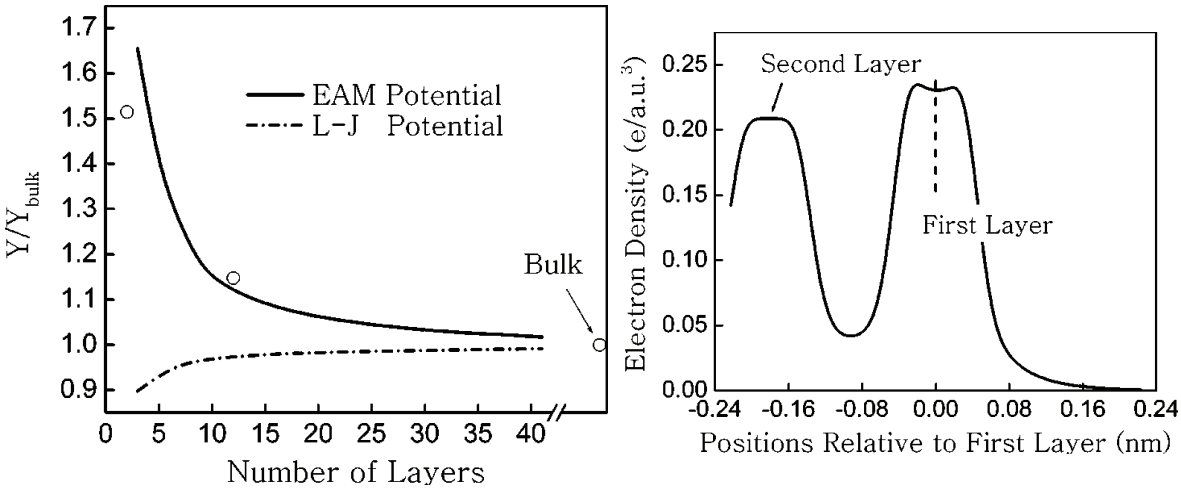

Figure 2.6.: (a) Dependence of Young's modulus normalized by the bulk value on number of atomic layers simulated for a copper thin film using: Lennard-Jones (L-J) potential (dashed-dotted line) and EAM potential (solid line). (b) Dependence of electron density in the copper thin film on position relative to the first atomic layer. Both graphs are adopted from [30].

EAM potential is opposite - the Young's modulus increases at the surface and the effect is much stronger as in the case of pair interactions. The authors attribute this effect to the increase of the electron density in the surface layers (figure 2.6), which leads to the stronger bonding. This study is an example that in nanoscale structures the origin of interatomic forces can be different and because of that the elastic properties can be changed significantly.

Another factor which can affect elastic properties of the surface is the surface relaxation. Again, for nanostractures the surface contribution is much higher than for the volume material, therefore, the contribution of the surface relaxation to the elastic properties can be significant. The bond-orientation-bond-length-bond-strength (bond-OLS) model proposed by C. Q. Sun

and coworkers [29] considers change of the bond energy due to contraction or expansion of the bonds. The authors propose a parameter c_i which is equal to relative change of bond length and describe its dependence on the coordination number of atoms in i^{th} layer [29]. The authors derive a formula which links the parameter c_i with the relative change of Young's modulus [29]:

$$\frac{\Delta E_i}{E} = c_i^{-m} - 3c_i + 2, \tag{2.37}$$

where m is a parameter which describes bond length dependence of the binding energy. For elemental solids $m \approx 1$ and for alloys $m \approx 4$ [29]. One sees that **bond contraction** ($c < 0$) **leads to hardening** of the material, whereas bond expansion leads to its softening.

The elastic properties of nanowires are mostly affected by their surface, since their surface-to-volume ratios can be very high for small diameters. The surface relaxation might be the dominating effect, which influences the elasticity of the nanosized structures. Figure 2.7 shows the experimentally obtained dependence of Young's modulus of different semiconductor nanowires on their diameters. The majority of the systems show increase of the Young's modulus with the decrease of the diameter. For all of them (ZnO [34], CuO [35], GaAs [25]) authors attribute this increase to the formation of the relaxed layer at the surface, where bond contraction and consequent hardening take place. C. Q. Chen and coworkers [34] estimated the thickness of relaxation layer in ZnO nanowires as 4.4 nm, and the relaxation in the outmost layer as 0.13 Å(2.5 %). For GaN [32] and InAs [33] nanowires the decrease of Young's modulus with decrease of diameter was found. In both cases the authors propose the surface tension effects as one of dominative phenomenas affecting the elasticity of the nanowires. Indeed, the followed molecular dynamic simulations of the Young's modulus of GaN nanowires [44] shows its decrease with diameter. However, the simulations were done for ultrathin nanowires (d < 4 nm) and surface relaxation effects were not taken into account. The data for InAs nanowires (figure 2.7 blue line) were obtained by resonance method, and relatively thick nanowires posses significant (more than 20 %) decrease of Young's modulus comparing to the bulk value. This behaviour can hardly be atributed to the surface tension effects. This could be either a systematic error in detection of eigen frequencies of the nanowires which arises due to high damping or effect of structural polytypism (alternation of Wurtzite and Zinc Blende structures). This study and the study by K. H. Liu and coworkers (figure 2.7 magenta line) on tungsten oxide nanowires [36] are good examples that defects (e.g. stacking faults) can significantly change elastic properties of nanowires. Moreover, the lateral orientation of the defects results in such an unusual trend which represents magenta line in the figure 2.7. The nature of the impact of the stacking faults on elastic properties of nanowires remains, however, unclear.

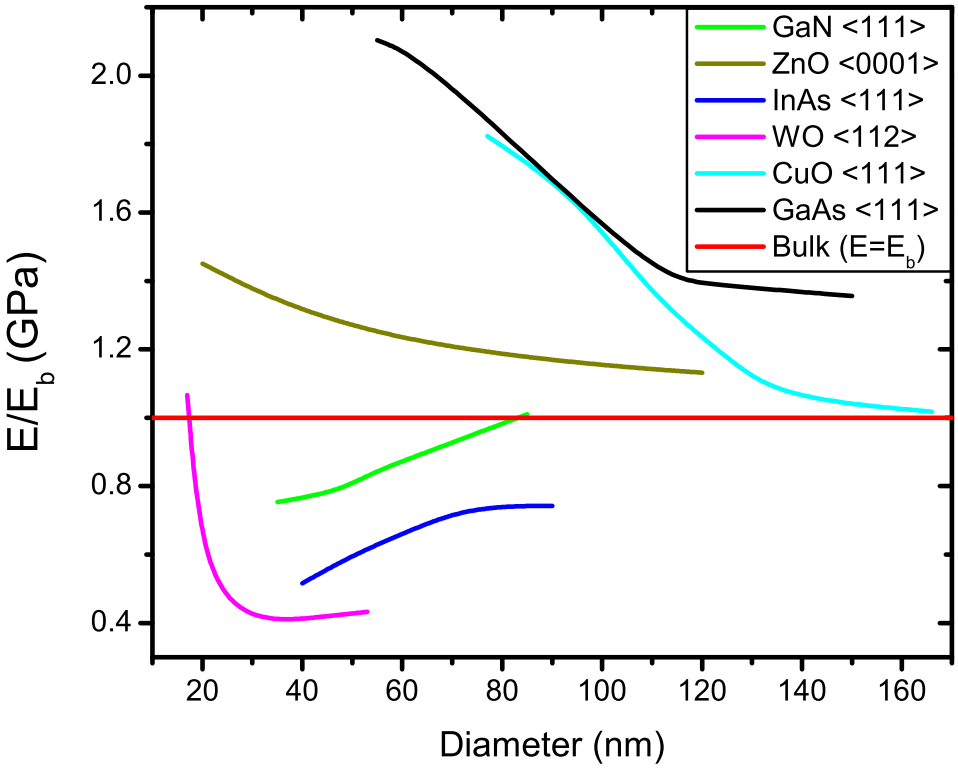

Figure 2.7.: Dependence of Young's modulus of nanowires normalized by their bulk values on the diameter of the nanowires. Different materials and growth directions shown with different colors (see legend). The sources of the plotted data are listed in the text.

3. Theoretical background: Electron transport

3.1. Electronic properties of InAs and its surface

Bulk InAs has a Zinc Blende crystal structure and is a material with high electron mobility of up to 4x10^4 cm^2(V s)$^{-1}$ (hole mobility up to 5x10^2 cm^2(V s)$^{-1}$), high intrinsic electron concentration ($\sim 10^{15}$ cm^{-3}) and, thus, low intrinsic resistivity of 0.16 Ω cm. Figure 3.1 schematically shows the band structure of InAs. One sees that InAs is a direct band semiconductor with a band gap of 0.354 eV at room temperature. The asymmetry of indirect gaps of 1.08 eV and 1.37 eV at L and X points respectively results in an anisotropy of the charge transport. The effective electron mass at the Γ-valley point is $m^* = 0.023m_0$.

The InAs surface has a natural electron accumulation layer due to the formation of donor surface states which pin the Fermi level above the conduction band [45]. The area concentration of the electron in the surface layer is on the order of 10^{12} cm^{-2} [46], whereas the thickness of the layer is on the order of the electron wave length. The accumulation layer has the properties of a two-dimensional electron gas (2DEG), and it shows Shubnikov-de Haas oscillations of magnetoconductance at low temperatures [47]. The donor states in the accumulation layer give rise to the ionized impurity electron scattering mechanism. The roughness scattering is another dominating factor limiting the electron mobility in InAs, and its overall effect is increased for the accumulation layer. Due to these scattering mechanisms, InAs surface has a much lower electron mobility than the bulk ($\approx$ 5x10^3 cm^2(V s)$^{-1}$)[48, 49]. The adsorbates at the InAs surface can change the surface states and, thus, change the electronic properties of the accumulation layer (e.g. positions of the Fermi level pinning) [50, 51]. A passivation of the InAs surface with sulfur atoms is commonly used to suppress the surface donor states and unpin the Fermi level [52].

3.2. Band gap broadening in Wurtzite InAs

The Wurtzite phase of InAs does not exists in bulk form, but it can be stabilized in nanostructures. Due to the lack of experimental data on the electronic properties of the Wurtzite phase theoretical calculations have been performed. The different lattice parameter of Wurtzite InAs

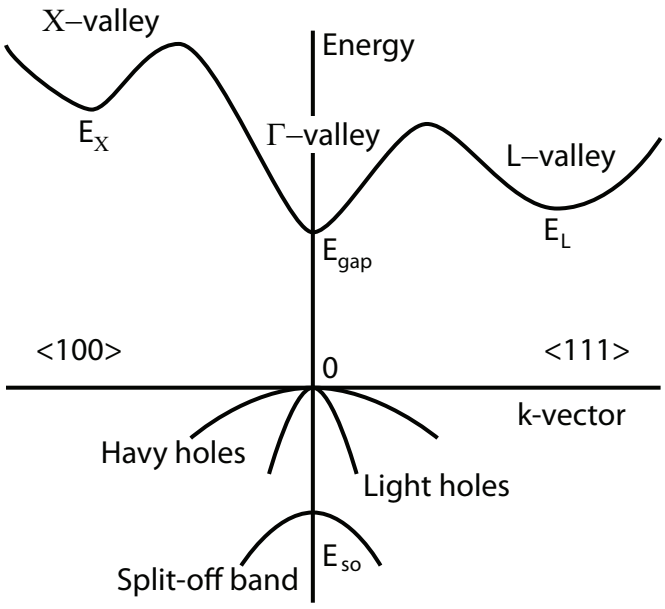

Figure 3.1.: Scheme of the band structure of InAs. Adopted with changes from [53].

(a_{WZ} = 4.2839 Å and c = 6.9954 Å compared to a_{ZB} = 6.0542 Å in Zinc Blende phase) results in the increase of the band gap [54]. DFT calculations revealed the significant broadening of the band gap in the Wurtzite direct band gap semiconductors [55]. More recent ab-inito calculations of the band structure of Wurtzite InAs [56] over-estimated the band gap, since the effect of spin-orbit (SO) coupling was not considered. Based on the assumption that the SO coupling is the same for the Wurtzite and the Zinc Blende phase, one calculated a band gap broadening of 55 meV at 0 K for Wurtzite InAs[56]. This value is consistent with the result published by A. De and C. E. Pryor who used transferable empirical pseudopotentials and included spin-orbit coupling [57]. Finally, the band gap of the Wurtzite InAs at 0 K is generally assumed to be 0.47-0.48 eV [56, 57], whereas the band gap of the Zinc Blende phase is 0.415 eV at 0 K [58].

The change of the stacking sequence (A B C for Zinc Blende structure and A B A B for Wurtzite) affects the size of the unit cell in $\langle 111 \rangle$ direction, decreasing it by the factor of 1.5 for the Wurtzite compared to the Zinc Blende phase. This modifies the phonon wave lengths and, thus, changes the scattering rate of the electrons. This indicates that not only the band gap of Wurtzite InAs is different from the Zinc Blende one, but also other transport parameters (e.g. electron mobility) might change. The discussion of the electron transport in Wurtzite and Zinc Blende nanowires will be continued in the next section.

3.3. Electron transport in InAs nanowires

Obviously, InAs nanowires should show different properties compared to bulk due to strong reduction of one of the dimensions. It was often reported in the literature that the re-

duction in the size in semiconductors leads to confinement effects characterized by the broadening of the band gap. Indeed, the theoretical calculations on InAs nanowires show an increase of the band gap and electron effective mass which increases for thinner nanowires [59–61]. E. Lind and coworkers performed atomistic simulations using $sp^3d^5s^*$ tight-binding method[1] [62] for $\langle 111 \rangle$-oriented cylindric nanowires with a surface passivated by hydrogen atoms [60]. The study revealed that the nanowires possess a direct band gap at the Γ-point. Figure 3.2 shows the dependence of the energies of the conduction and valence subbands on the nanowire diameter. These results, however, are not fully consistent with the results of the same kind of simulations performed by M. P. Persson and H. Q. Xu for $\langle 100 \rangle$-oriented nanowires with square and rectangular cross sections [59]. The valence band for a 13 nm square nanowire possesses complex non-parabolic structure with double maxima and band anticrossings (figure 3.3). Moreover, the nanowire shows indirect band gap, which is surprising and has never been reported for InAs before. Opposite to this result, smaller (3 nm) nanowires with a square cross section, studied using the same method, show a direct band gap [61]. The difference in those studies is that in the first one, the spin orbit coupling was included, and the nanowires have, probably, $\{100\}$[2]-type facets [59] against $\{110\}$-facets in the second case [61]. I consider those results as a direct theoretical evidence that different faceting may result in a significant change of the transport properties of the nanowires. The crystallographic orientation of the wire axis is another important factor affecting the electronic structure of the nanowires. The same $sp^3d^5s^*$ simulations by Alam et al. show that the $\langle 111 \rangle$- and $\langle 110 \rangle$-oriented InAs nanowires (with a square cross section) behave very similar, whereas the $\langle 100 \rangle$-oriented nanowires have a larger band gap and effective mass of electrons (figure 3.4) [61]. However, this effect is significant only for nanowires with a diameter below 10 nm. The theoretically obtained trends of the increase of the band gap with the decrease of the nanowire diameter were confirmed by F. Wang and coworkers in a photoluminescence study of InAs quantum wires (5-14 nm in diameter) [63]. Before reviewing the experimental studies on the electron transport in InAs nanowires I should mention that the $sp^3d^5s^*$ tight binding model tends to overestimate the $\Gamma - L$ separation. However, this does not affect the trends shown in figures 3.2-3.4 and discussed above.

In reality, the transport in InAs nanowires is dominated by their surface. Since the thickness of the electron accumulation layer t_{acc} is in the order of the electron wave length (see section 3.1), one can estimate it using the simple equation: $t_{acc} \sim \lambda = h/\sqrt{2m^* E_f}$, where h is Planck's constant, m^* is electron effective mass and E_f is the Fermi energy. Using the parameters discussed in section 3.3, the accumulation layer thickness is on the order of 15 nm[3], thus

[1] Tight-binding method based on description of crystals in terms of chemical bonds and computation of the set of approximate atomic wave functions and consequent overlap matrices [62]. The term "$sp^3d^5s^*$" shows which orbitals are considered in the calculation.

[2] Authors write $\{110\}$-facets in the body of the article whereas in the figure, which shows the nanowire model used for the simulations, the wire is decorated with $\{100\}$-facets.

[3] for the nanowires thicker than 30 nm. For the thinner nanowires the effective mass increases with the diameter

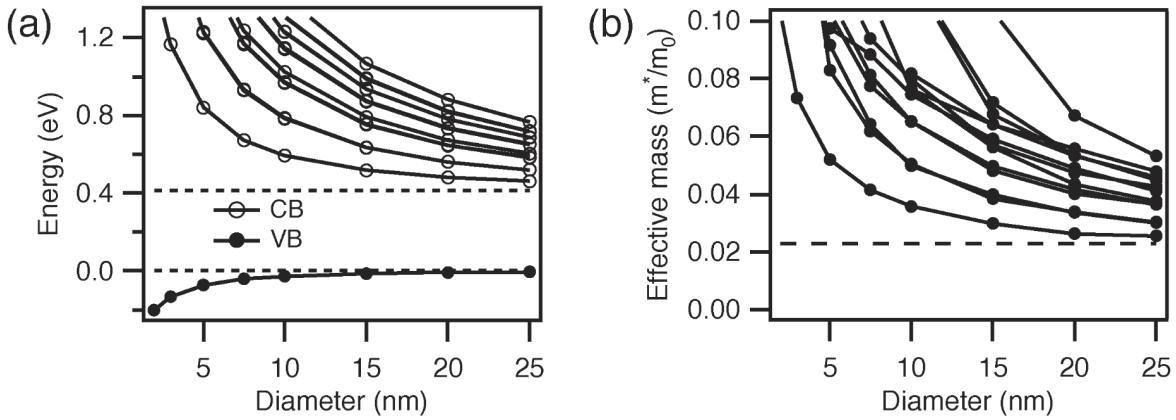

Figure 3.2.: (a) Dependence of the energies of the conduction bands (CB) and the top of the valence (VB) bands on the diameter of Zinc Blende InAs nanowires. (b) Diameter dependence of the corresponding electron effective mass m^* presented in the units of the steady electron mass m_0. Adopted from [60].

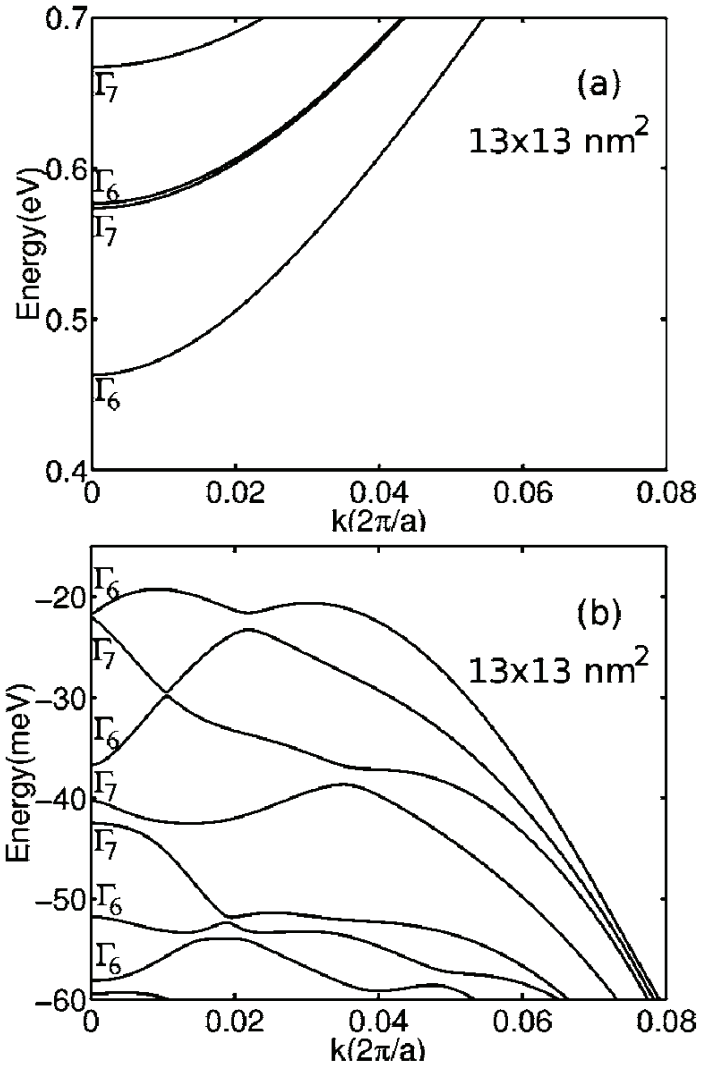

Figure 3.3.: Band structure of a Zinc Blende InAs nanowire with a square cross section (13 nm x 13 nm). The conduction band is shown in (a) and the valence band in (b). Adopted from [59].

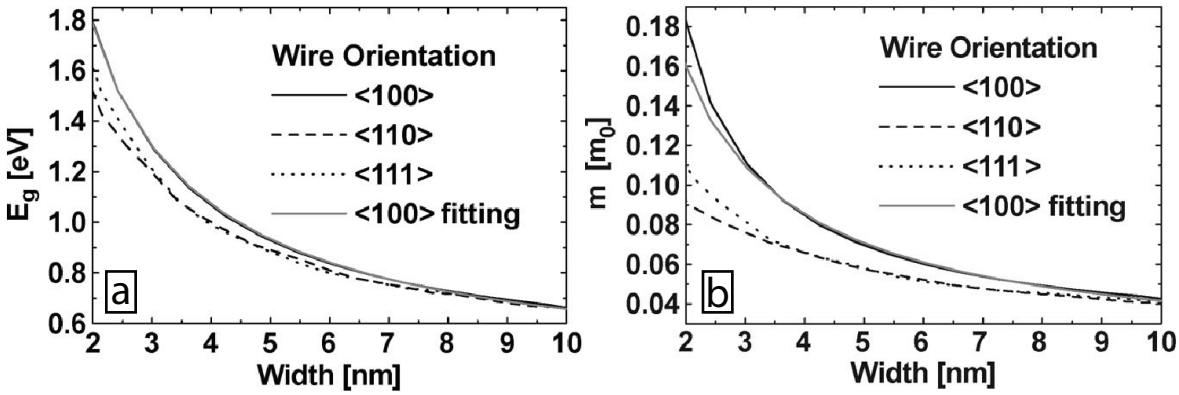

Figure 3.4.: Diameter and orientation dependence of the band gap (a) and effective mass (b) of the Zinc Blende InAs nanowires. Adopted from [61].

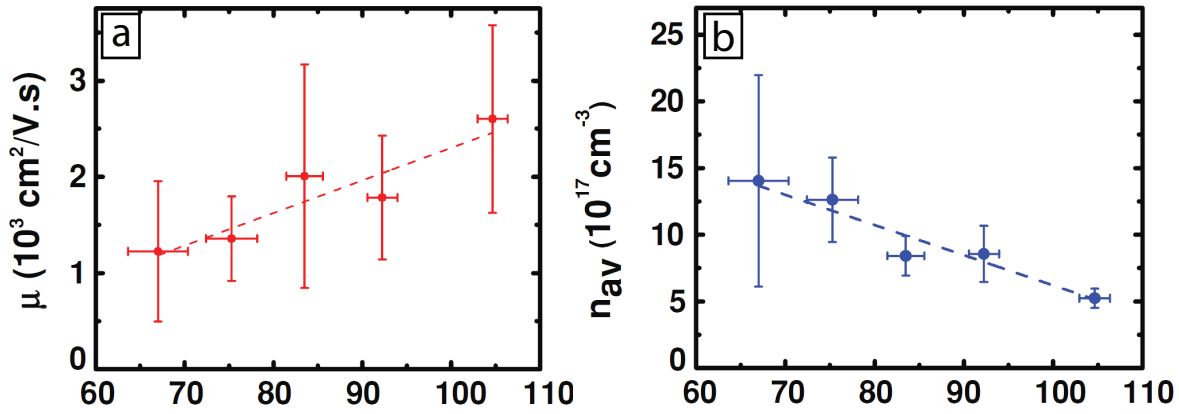

Figure 3.5.: Dependence of (a) electron mobility μ and (b) average electron concentration n_{AV} on the diameter (in nanometers) of InAs nanowires. Adopted from [12].

the surface effects should be pronounced even for nanowires thicker than 100 nm. Indeed, the study of Talin and coworkers shows that the change of the surface states by surface contamination results in the change of the transport properties of the nanowire field effect transistor (FET) [23]. Furthermore, the nanowires show n-type conductivity which is caused by the accumulation layer at the surface [22, 23, 64, 65]. The measurement of the transport coefficients (carrier mobility and concentration) performed by Dayeh and coworkers utilizing FET geometry shows that the electron mobility decreases and the carrier concentration increases with the decrease of the nanowire diameter (figure 3.5) [22]. The study of Talin and coworkers shows similar behavior of the transport coefficients, however, the shapes of the curves are different [23]. Since the accumulation layer should possess decreased electron mobility and increased carrier concentration, these dependences confirm that, indeed, the charge transport in the InAs nanowires occurs mostly at the surface in the electron accumulation layer.

Since the nanowires can be heated during the electrical characterization, it is important to have information about thermoelectric properties of the nanowires. Mavrokefalos with cowork-

(figure 3.2), thus the accumulation layer will be thinner.

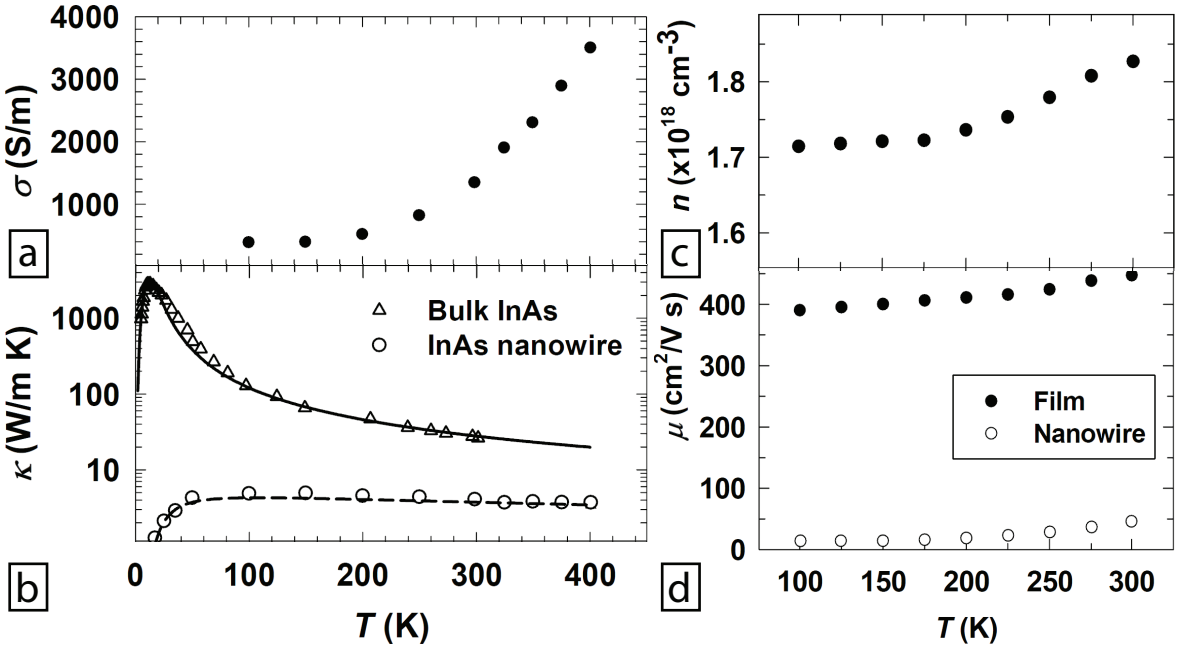

Figure 3.6.: Dependencies of (a) conductance σ, (b) thermal conductivity κ, (c) electron concentration n and (d) electron mobility μ on the temperature for the patterned InAs nanowire with the rectangular cross section 40 nm x 150 nm. Adopted from [65].

ers studied the dependence of the conductance σ, thermal conductivity κ, electron concentration n and electron mobility μ on the temperature (figure 3.6) for the patterned InAs nanowires with a rectangular cross section of 150 nm x 40 nm [65]. One sees that the electrical conductance has a very strong temperature dependence around room temperature (figure 3.6 *a*). Thermal conductivity at the room temperature is six times lower than the corresponding bulk value (figure 3.6 *b*) [65]. The authors attribute this behavior to the increase of the role of the high frequency phonons in the nanowires compared to the bulk. The phonons suffer from boundary scattering, and, thus, the mean free path of the phonons should be on the order of the nanowire thickness (40 nm) [65]. Interesting is that both electron concentration (3.6 *c*) and mobility (figure 3.6 *d*) increase with increasing temperature, whereas in the bulk InAs the electron mobility decreases with increasing temperature [66]. This effect is quite surprising, since the phonon scattering, reducing the electron mobility, should increase with temperature even for the 2DEG at the nanowire surface [67, 68]. The same result was obtained for InAs thin films which were used to fabricate the nanowires (figure 3.6 *d* solid circles). But, the mobility in the nanowires is an order of magnitude lower [65], which is attributed to an increase of electron scattering due to a bending of the nanowire during sample preparation.

Before proceeding with the effect of planar defects on the electron transport in InAs nanowires, it is worth to discuss the mean free path (MFP) of the electrons. If the defects act like scattering centers, the comparison of the defect separation and the MFP can give an idea on the impact of the defects on the electron transport. X. Zhou and coworkers observed two regimes of

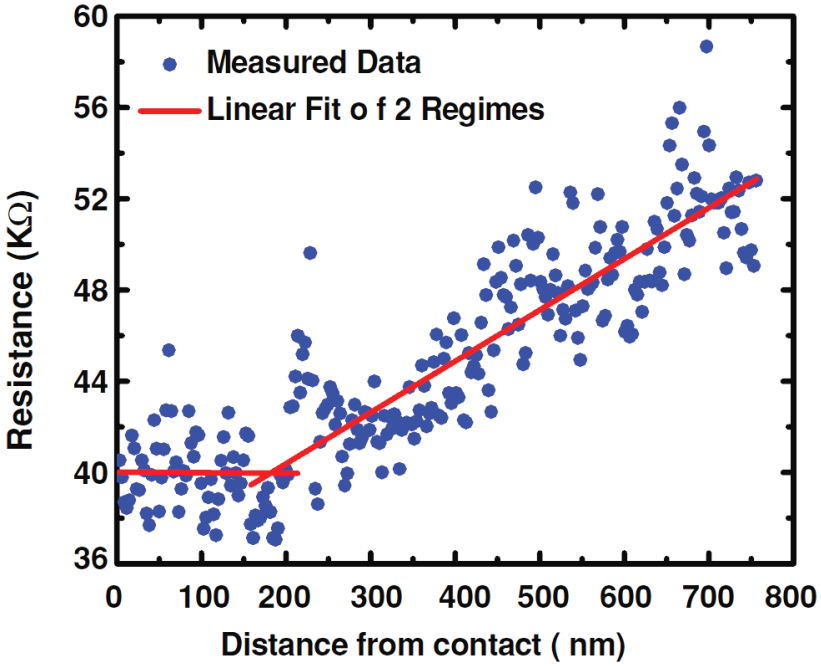

Figure 3.7.: Dependence of the resistance of an InAs nanowire on the distance between the cAFM tip and another electrical contact used for the resistance measurement. Adopted from [12].

electron transport in the InAs nanowires by using conductive atomic force microscopy (cAFM) [64]. Figure 3.7 shows the dependence of the nanowire resistance on the distance between the cAFM tip and the contact which was deposited on one end of the nanowire. The resistance does not change between 0 and 200 nm. After 200 nm it depends linearly on the distance. The first regime can be attributed to the ballistic transport in the nanowire, when the electrons are not scattered between the terminals. The second regime shows drift-diffusion conductance. Since the length of the distance-independent transport region (200 nm) is equal to several MFP, the authors estimated the mean free path of the electrons L_m ~ 55nm [12].

The structural polymorphism in the InAs nanowires is another factor which plays a significant role in the electron transport. Since the formation energies of the Zinc Blende and Wurtzite phases are very close for the nanowires with a diameter below 100 nm, the presence of both structures in the nanowires is common [12, 69–71]. The structural changes in the ⟨111⟩-oriented nanowires appear through the planar stacking defects, which are perpendicular to the wire axis and expected to possess the band offset [72]. Dayeh and coworkers studied transport in Zinc Blende (ZB) nanowires without defects and Wurtzite (WZ) nanowires with planar defects [73]. They found that the resistance of a ZB nanowire is an order of magnitude higher than that of a WZ nanowire with stacking faults. In their later study, however, they attribute this difference to the change of contact resistance and extract very close values for the average transport coefficients: n_{ZB} = 6.4 x 10^{17} cm^{-3} vs n_{WZ} = 8.5 x 10^{17} cm^{-3} and μ_{ZB} = 2200 cm^2 $(V\ s)^{-1}$ vs μ_{WZ} = 1700 cm^2 $(V\ s)^{-1}$ [12]. The authors also observed a significant enhancement of the sub-threshold characteristics of the FET for the nanowires with defects and attributed it

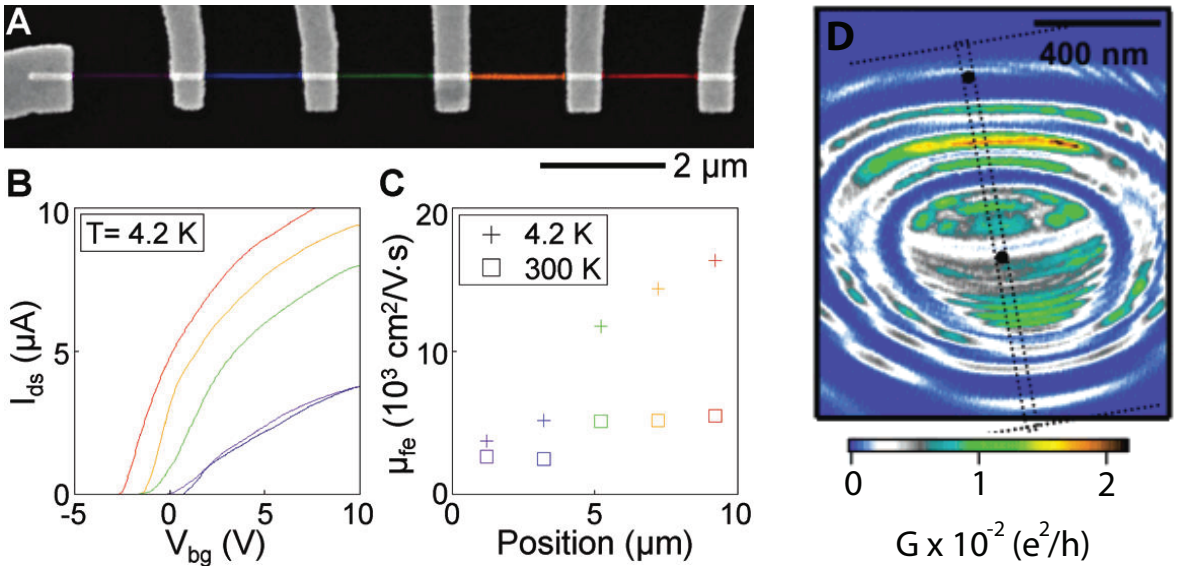

Figure 3.8.: (a) Scanning electron micrograph of an InAs nanowire with six drain-source contacts. The colors in the segments are artificial, and they indicate the nominal defect density in the nanowire: from violet to red (from left to right) the defect density decreases. (b) Dependence of the drain-source current I_{ds} on the gate voltage V_{bg} and (c) the dependence of the electron mobility μ_{fe} on the position (c) have the same color code as (a). (d) A scanning gate microscopy image of an InAs nanowire showing in color code the dependence of the nanowire conductance G on the local gate (tip) position. Dotted lines show positions of the nanowire, and drain and source electrodes. Black dots show the positions of quantum dots inside the nanowire. (a-c) Adopted from [24], (d) adopted from [18].

to the spontaneous polarization of the ZB/WZ interface when a gate voltage is applied [12].

Another evidence of the impact of the stacking faults on the electron transport is the observation of quantum dots (QD) inside the nanowire at liquid helium temperatures by Bleszynski and coworkers [18]. The Coulomb blockade conductance peaks associated with the quantum dots were imaged using scanning gate microscopy and are shown in figure 3.8 *d*. The formation of the QD in the nanowire is probably a result of the electron scattering along the nanowire axis induced by the stacking faults. The observed formation of the quantum dots is random and can be rather correlated with the defect positions since the defect density is high.

Schroer and coworkers attempted to correlate the defect density in InAs nanowires with electron mobility [24]. The experiment was done in the FET geometry with several drain-source contacts deposited on the nanowire (figure 3.8 *a*). The stacking fault density depends nominally on the position. The authors measured dependencies off the drain-source current on the gate voltage at different positions (figure 3.8 *b*). The corresponding electron mobilities are shown in figure 3.8 *c*. At 4.2 K the electron mobility decreases with increasing defect density: the mobility is about 4 times lower in the region with high defect density than in the nominally defect free region [24]. At room temperature, however, there are essentially only two distinct regions where the mobilities differ by approximately 100%. ”This suggests that while the room temperature mobility is close to being limited by phonon scattering, the planar defects are the

dominant factor limiting mobility at low temperatures."[4]

In summary, the following peculiarities of electron transport in InAs nanowires should be underlined:

- Quantum confinement effects results in the broadening of the band gap and in the increase of electron effective mass for the thinner nanowires;
- The electron transport in the nanowires is dominated by surface conductance through natural electron accumulation layer, which thickness is estimated to 15 nm for the diameters above 30 nm. The surface effects result in an increase of the effective electron concentration and a decrease of the effective electron mobility;
- A strong temperature dependence of conductance can be expected around room temperature;
- There are experimental evidences that the Zinc Blende/Wurtzite polymorphism influence the electron transport.

However, the question, how does the stacking faults in the nanowires affect the electron transport in the nanowires, remains open.

3.4. Electrical contact theory and its application for InAs nanowires

An electrical contact between two solid bodies can consist of one or several contact spots so called "a-spots". The electrical current is compressed to a smaller volume around the a-spots [74]. Due to the constriction, less material contributes to the electrical current transport, and the resistance of the system increases by the contact resistance. The contact resistance theory described bellow is applicable for the ohmic contacts (e.g. metal-metal contacts). In the classical theory the constriction resistance R_C in a circular a-spot is given by:

$$R_C = \frac{\rho_1 + \rho_2}{4a}, \tag{3.1}$$

where ρ_1 and ρ_2 are electric resistivities of the material, which are in contact, and a is a radius of the a-spot [75]. The equation is a simple electrodynamic solution of the current constriction problem which is based on the following assumptions: i) a-spot is a disc; ii) the current flow is continuous through the contact point. If the size of the a-spot is in the order of the electron mean free path, the current is not continuous any more, and only few electrons can pass through

[4] [24]

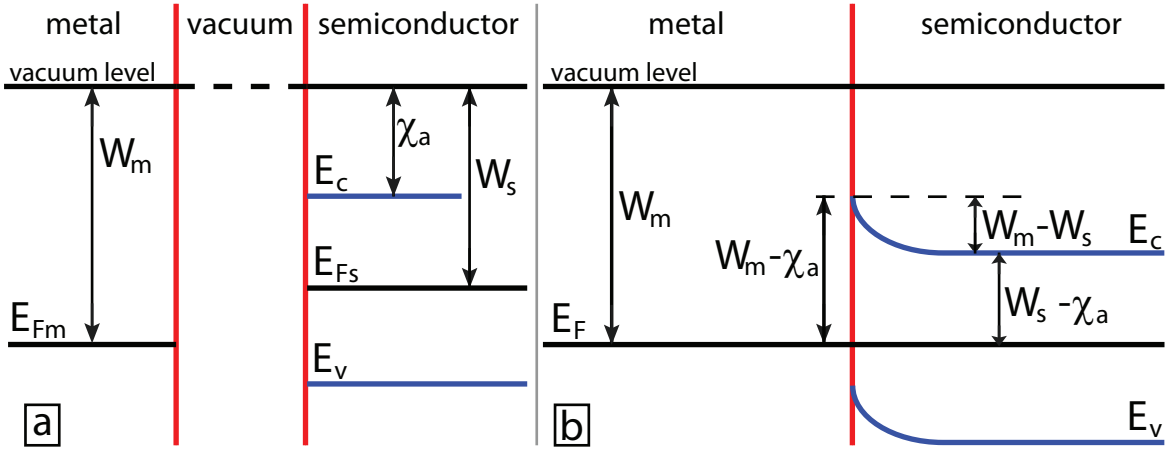

Figure 3.9.: (a) Band diagram of a metal and a semiconductor separated from each other. (b) Band diagram of the metal and the semiconductor in contact. The Fermi levels of metal and semiconductor are shown with black lines (E_{Fm} and E_{Fs} respectively). The conduction and valence bands of the semiconductor are shown with blue lines (E_c and E_v respectively).

the constriction. In this case, the electrons do not diffuse through the contact area but pass through it ballistically. Sharvin in 1965 solved the problem of ballistic transport through a small constriction and obtained the Sharvin resistance term:

$$R_S = \frac{4mV_F}{3\pi ne^2a^2}, \tag{3.2}$$

where m is the electron mass, e is the electron charge, V_F is the velocity of Fermi electrons, n is the electron concentration [76]. Alternatively, equation 3.2 can be reduced to $R_S = C/a^2$, where $C = 4mV_F/(3\pi ne^2)$. The total contact resistance, therefore, can be written as $R_{cont} = R_C + R_S$.

A metal-semiconductor interface can show, however, a non-ohmic behavior due to a potential barrier. If the Fermi level of the metal and the semiconductor have different positions (figure 3.9 *a*), after the contact is established, electron density redistribution takes place in the semiconductor in a way that the Fermi level on both sides of the interface is equal (figure 3.9 *b*) [77]. Thus, the semiconductor Fermi level changes its position by the difference between the metal and semiconductor work functions $W_m - W_s$. Far from the semiconductor surface, the conduction and valence bands (E_c and E_v) will maintain their original separation with the Fermi level (e.g. $W_s - \chi_a$ for the conduction band, where χ_a is the electron affinity). At the interface, the conduction band bends in a way that the semiconductor has the original electron affinity. Therefore, both bands possess their original positions at the interface [77]. To be injected into the semiconductor, the electron has to overcome a potential barrier between the Fermi level and the conduction band at the interface. The barrier height is equal to $W_m - \chi_a$ (see figure 3.9), and in the case of intrinsic semiconductors it is called the Mott barrier. In the case that the semiconductor contain donor or acceptor states, it is called Schottky barrier [78, 79].

InAs nanowires are often grown by gold catalyzed chemical vapor deposition (CVD)

method. These nanowires have a gold nanoparticle which remains on the top of a wire. The interface between the gold nanoparticle and the InAs nanowire may show a potential barrier (Mott barrier) with a height of 0.2 - 0.57 eV, since the electron affinity of bulk InAs is equal to 4.9 eV, and the work function of gold is between 5.1 eV and 5.47 eV. Due to quantum effects, however, the electron affinity of the nanowires can be different. Moreover, the gold particle often forms an alloy with As [80] which also changes the work function of the nanoparticle.

In the thesis, the electron transport of the InAs nanowires is investigated using a two-point contact method with a gold tip to contact the nanowire to the gold nanoparticle which is on top of the wire. I estimate the resistance of the interface between the gold tip and the gold nanoparticle, using equations 3.1 and 3.2. Inserting the resistivity of gold as ρ_{Au}=2.2 x 10^{-8} Ω x cm $\equiv$ $\rho_1 \equiv \rho_2$, C = 3.58 x 10^{-16} Ω m^2 [76] and a-spot radius a = 5 nm, we find the tip-nanoparticle contact resistance R_{cont} = 16.5 Ω. For the smaller contact spot with radius a = 2 nm, the contact resistance will be 95 Ω.

4. Experimental techniques and sample preparation

4.1. Growth of InAs nanowires by chemical vapor deposition

InAs nanowires were grown by chemical vapor deposition (CVD) in a hot wall reactor in the group of Professor F.-J. Tegude (University of Duisburg-Essen). Colloidal gold nanoparticles with diameters of 50 nm were first deposited on InAs (100) substrates. Prior to the nanowire growth the substrate with particles was annealed at 620 °C for 2 minutes under As flow. The wires were grown at 420 °C and 400 °C using a V/III precursor ratio of 6. Tertiarybuthylarsin (TBAs) was used as a group-V precursor and trimethylindium (TMIn) as a group-III precursor. The resulting diameter of the nanowires depends on the size of the gold seeds and deviates from the diameter of the catalyst nanoparticles by 10-15% in both directions. The length of the nanowires depends on the growth time, which was set to 10 minutes, and on the pressure of the precursors. However, even for the same growth time and precursor pressure the length of the wires varied from sample to sample. It was shown previously that the growth rate is affected by the spacing of the nanowires: the growth rate increases with the spacing up to a maximal value and decreases again down to a growth rate of thin films with further increase of the spacing [81]. Thus, the variation of the nanowires length can be explained by the variation of the nanoparticles density which was not controlled.

4.2. Electron microscopy techniques for the analysis of morphology, composition and atomic structure

4.2.1. Scanning electron microscopy (SEM)

In a scanning electron microscope (SEM) a focused electron beam with an energy typically within 5-30 keV is used to scan across the sample surface to obtain a micrograph of the sample with a resolution down to several nanometers. A secondary electron detector or back scattered electron detector is normally used to collect a signal from each point of the scanned area. The signal is used to form a micrograph, where the intensity of a pixel is proportional to the signal. A principal scheme and more detailed description of an SEM can be found elsewhere [82].
In this work a Leo 1530 SEM equipped with a field emission gun (FEG) operated at 10-20 kV and utilizing an in-lens secondary electron detector was used to investigate the morphology of as grown InAs nanowire samples. The substrates with the nanowires were installed parallel to the electron beam (using special sample holder) on an SEM stage which was tilted by 5 °. Under this condition the nanowires can be viewed from the side and the angles between nanowires and substrate can be measured.

4.2.2. Conventional and high resolution transmission electron microscopy (HR-TEM)

In a transmission electron microscope (TEM) the electron beam is accelerated to high energies (typically between 80 and 400 keV) towards a thin sample, which is transparent for the electrons (less than 300 nm thick, depending on the material). The electrons go through the sample and are elastically or inelastically scattered. Electrons, which passed through the sample, are focused and magnified by electromagnetic lenses, and form an image on a fluorescent screen. The areas of the screen which are hit with more electrons will appear brighter than the ones which have receive a lower electron dose. There are three mechanisms of contrast formation:

1. **Mass-thickness** contrast. Electrons are more strongly scattered by atoms with higher atomic number (Z) (Rutherford scattering). Since the image is formed by electrons scattered at low angles ($< 5°$), thicker parts of the sample or parts with heavier atoms will scatter more electrons at high angles, thus, will appear darker;

2. **Diffraction** contrast. The formation of the diffraction contrast is related to the orientation of the crystalline sample. Since, in diffraction scattering of electrons occurs at specific Bragg's angles, the intensity of the objects which fulfill Bragg's conditions is strongly reduced;

3. **Phase** contrast. The phase contrast, is a result of the interference of electron waves after they passed through the sample. The electron waves are affected by different parameters like thickness, diffraction, electrical and magnetic fields.

High resolution TEM (HR-TEM) uses interference of the electron waves, which passed through the sample, for image formation. The interference will contain information of the phase of the waves (refer to phase contrast above). The phase imaging can be done on weak phase objects, that should be thin enough to deliver small variations of electron phase (less than $\pi/2$). The electron wave, right after it passed through the sample, called electron exit wave. The exit wave exhibits peaks at atom position. Propagating further, the electron wave is transformed by lenses of a TEM into so-called image wave. The relation between exit wave and image wave is defined by contrast transfer function, which depends on microscope parameters (e.g. defocus) and spatial frequency [83]. Depending on defocus the image wave appears differently: it can have either maxima or minima at the corresponding maxima of the exit wave. At Scherzer defocus the CTF has a wide plateau at low spatial frequencies, resulting in a wide region where the information on an exit wave is included into image wave.
Technically, high resolution TEM images can be obtained by orienting the electron beam along one of zone axes of the sample and increasing the magnification to 300-600 thousand times. More information about TEM and HR-TEM imaging can be found in [83].
In this work an FEI Tecnai F20 TEM operated at 200 kV was used to study morphology, chemical composition and crystalline structure of the nanowire samples. The microscope is equipped with a Schottky FEG, a super twin lens which results in a point resolution of 0.23 nm, an energy dispersive X-Ray (EDX) detector, high-angle annular dark-field (HAADF) detector and Gatan image filter (GIF) system. For the TEM studies the nanowires were transfered onto a copper grid (3.05 mm in diameter) coated with holey amorphous carbon by touching the nanowire sample with the grid. The grid was installed in the FEI double tilt TEM sample holder which can be tilted ± 45 degrees along it axis. A sample in the holder can be tilted by ± 20 degrees along the perpendicular axis. By tilting the sample different orientations of a selected nanowires were achieved, and HR-TEM images for different zone axes could be recorded. Bright spots on the images represent atomic columns. Fast Fourier transformation (FFT) of the images shows a reciprocal lattice.

4.2.3. Selected area electron diffraction (SAED)

Selected area electron diffraction (SAED) was performed on the nanowires inside TEM by setting the selected area aperture of the TEM on the region of interest (mostly in the middle of a selected nanowire) and switching the microscope into the diffraction mode with parallel illumination. The direct beam was always closed with a beam stop, the diffraction patterns were recorded with a charge-coupled device (CCD) camera and indexed by measuring the reflex spacing ratios and angles between them, as described elsewhere [84]. By indexing of diffraction patterns the crystal structure could be determined. To correlate real space images with crystallographic orientations the selected area aperture was retracted and the electron beam was

unfocused until the shadow of the nanowire was seen in the primary beam (the microscope remained in the diffraction mode). This imaging condition allowed to overcome the problem of image rotation due to switching to the diffraction mode and allowed to determine the growth direction of the nanowire by comparison of the indexed diffraction pattern with the unfocused diffraction image.

4.2.4. Z-contrast imaging with high resolution scanning transmission electron microscopy

In scanning transmission electron microscopy (STEM) the electron beam of TEM is to be focused in a fine spot (probe) by utilizing condenser lenses. A scan generator signal drives beam deflection coils which enable movement of the beam across the sample surface. Simultaneously with the scan different detectors can be used to obtain spatially resolved information (e.g. chemical composition, crystal misorientation). The spatial resolution of STEM depends on the size of the probe, its aberrations, scan parameter and microscope stability. The electrons that scattered at high angles (>50 mrad [83]) contain information about the atomic number of the atoms of the sample. The electrons can be detected by a high-angle annular dark-field (HAADF) detector. The signal is proportional to the average Z-number of the corresponding area.

An FEI Titan 80-300 STEM operating at 300 keV equipped with electron beam monochromator and probe aberration corrector was used for high resolution STEM (HR-STEM) imaging of the InAs nanowires using HAADF detector.[1] Prior to the experiment the spot size was set to 6 and the electron beam was focused to the smallest possible probe size. The aberration corrector was setup the way to maximize the central area of the probe which does not posses drastic aberrations (i.e. spherical and higher order). The performed alignment of the microscope allowed to achieve sub-angstrom resolution. During the experiment the microscope was kept in STEM mode to prevent instrumental instabilities.

The nanowires were transfered from the substrate onto a copper TEM grid covered with a holy amorphous carbon film by touching the substrate surface with the grid. The grid was installed in a double-tilt TEM sample holder and transfered into the microscope column. Single nanowires with thickness below 50 nm were selected for the experiment and positioned with their zone axis parallel to the electron. Convergent beam electron diffraction was used to check the orientation of the nanowire with respect to the electron beam. In the next step high magnification (about 2 Mx) images were acquired and processed using FFT to identify the nanowire zone axis. Since twin defects are of particular interest in this experiment the further experiments were done on the wires oriented with their $\langle 110 \rangle$ zone axis parallel to the electron beam. The acquisition of the HR-STEM micrographs was done setting the magnification above 10 Mx,

[1] The experiment was done in Ernst Ruska-Centre (ER-C) for Microscopy and Spectroscopy with Electrons in Jülich, Germany.

camera length to 0.077 m, dwell time to 22 μs.

4.2.5. Energy dispersive X-Ray spectroscopy (EDXS) line scans and mapping

In energy dispersive X-Ray spectroscopy (EDX or EDXS) characteristic X-Rays are detected, that are emitted by a sample after high energy electron excitation. An EDX spectrum consists of characteristic peaks which represent specific electron transitions in the atoms, yielding quantitative information on the chemical composition as described by Williams and Carter [83] for example.
The chemical analysis in this work were performed by EDXS in scanning transmission electron microscopy (STEM) mode in the FEI Tecnai F20 TEM. In the STEM mode the electron beam is focused with a diameter of a spot of about 1 nm. The focused electron beam was scanned across the sample (mapping) or along a predefined line (line scan). Only X-Ray counts for the selected elements were recorded during the mapping and line scans. To control the position of the sample prior and during[2] a line scan or EDXS mapping a scan with simultaneous HAADF detection was performed.

4.2.6. Three-dimensional electron tomography (3D tomography)

In conventional transmission electron microscopy the micrographs only show two-dimensional (2D) projections of nanoobjects. Three-dimensional (3D) electron tomography (3D tomography) is required to analyze the three dimensional morphology, cross sections and faceting. The TEM or STEM images of an object are acquired at different angles with subsequent reconstruction of the 3D shape of the object (see scheme in figure 4.1). A special TEM holder is used to acquire a set of images by tilting the sample holder at different angles. It is important to acquire images with large tilting angles (about 70 °) to reduce a so-called "missing wedge", which is illustrated in figure 4.1 *b*. "Such missing information can lead to artifacts, and reconstructions can be elongated in the direction of the missing wedge."[3] The reconstruction is typically done by "back-projecting" the acquired images. Sampling rate is determined by angle θ between two nearest projections (see figure 4.1 *b*). Figure 4.1 *b* shows schematically central slices in a reciprocal space, that correspond to the projections. The scheme helps to understand that the high spatial frequency tends to be undersampled compared to the the low frequency. This results in blurring of the reconstruction. Therefore, the resolution can be increased by increasing the number of the images in the tilting series (decreasing θ). However, the decrease

[2] So called drift correction. After each EDX acquisition performed at a single point of the sample a HAADF image of a reference object was recorded. Mechanical drift of the stage was corrected by adding a lateral displacement of the reference object to coordinates of the next acquisition point.
[3] From [85]

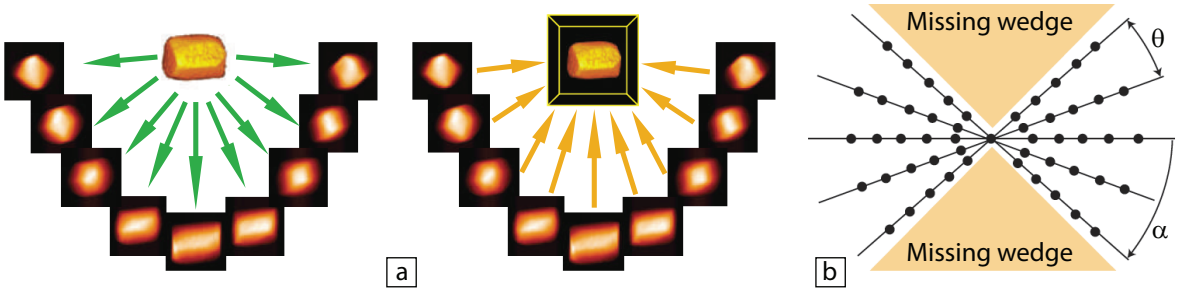

Figure 4.1.: Scheme (a) of two stage electron tomography. It consists of acquisition (left) of tilt series of TEM (STEM) micrographs rotating an object about a single axis (the sample holder axis) and transfer of the images back into 3D space (right) with consequent reconstruction of the 3D shape of the object [85]. (b) Representation in Fourier space of the data set of the projections. The projections are shown as the central slices (black lines) with black dots that correspond to the data points. The restriction of maximal tilt angle α and angle between projections θ results in a missing wedge and undersampling of the information with high spatial frequencies respectively [85]. The images are adopted from Midgley et al. [85].

of θ leads to an increase of acquisition time and thus irradiation time, which can lead to sufficient electron beam damages of a sample. In practice, recording images every 1-2° results in a sufficient resolution and negligible electron beam damage [85]. Another way to overcome the blurring is the iterative reconstruction procedure in which the result of a reconstruction is re-projected and compared with the original series. The reconstruction is to be improved until the best fit of the original data set and the re-projected images is achieved.

Three dimensional electron tomography was performed on InAs nanowires in the Tecnai F20 TEM. Tilt-series were recorded automatically using the ”xplore 3D” software with the TEM operating in STEM mode and using a HAADF detector for acquisition (refer to section 4.2.5). A ”Fischione Instruments” single-tilt tomography holder was used to acquire images either at tilt intervals of 2° within a tilting range of -60° to 60° or intervals of 1° within the range of ±(61 to 75)° [86]. The InAs nanowire was aligned parallel to the holder rotation axis by rotating a TEM grid on which the nanowire was placed. This alignment was necessary to minimize a variation of height along the nanowire axes at high tilt angles which results in different focus conditions for different parts of the nanowire and subsequent loss of resolution. The 3D shape of the nanowires was reconstructed with the ”FEI Inspect 3D” software which utilizes a simultaneous iterative reconstruction technique (SIRT) described in detail in [87].

4.2.7. High resolution transmission electron microscopy image simulations.

The analysis of HR-TEM contrast is not straight forward due to the contribution of variations of thickness, scattering factors, imaging conditions and electromagnetic fields to the phase shift of electron waves. Therefore, simulations of HR-TEM images are often required to inter-

pret experimental data correctly.

In this work all HR-TEM simulations were performed using an QSTEM software which employs a multislice algorithm [88]. In the models for the simulations the relative coordinates of the atoms in a box with defined size and their scattering parameters are set as described in detail in appendix D. Due to the computational limitations the box for the simulations can not exceed 10 nm in one dimension. Consequently, the atomic models represent only a part of the samples which listed bellow:

- A segment of Zinc Blende InAs with a para-twin (see section 5.1.4 for twin defect classifications).
- A segment of Zinc Blende InAs with an ortho-twin.
- Bended segments of Zinc Blende InAs with different bending strain.

The parameters of the FEI Tecnai F20 TEM used for the simulations are listed in appendix D. The images were simulated for different focus conditions: in a range of several tens of nanometer for twin segments and at Scherzer focus[4] for the bended segment. For additional structural analysis the FFT of the simulated images was performed.

4.3. In-situ transmission electron microscopy techniques

In this section the main experimental techniques which were used in the work are discussed. All the methods are a combination of a conventional method with transmission electron microscopy, which results in the unique possibility to determine elastic or electrical properties of a single nanoobject and correlate them with the morphology and the atomic structure directly.

4.3.1. Electromechanical resonance

The elastic properties of InAs nanowires were studied utilizing the electromechanical resonance technique in-situ in a Phillips CM12 TEM. A "Nanofactory^{TM} Instruments" scanning tunneling microscopy (STM) holder was used [89]. The holder is shown in figure 4.2. The main part of the holder is a piezo driven STM tip which is inserted into a "hat". The hat has legs to fix it on a ball attached directly to the piezo tube. This type of connection allows slip-and-slide movement of the hat against the ball when the piezo is electrically shaken, allowing a rough

[4] defined by the formula: $\Delta f_{Scherzer} = -1.2\sqrt{C_s\lambda}$, where C_s is the spherical aberration, λ is the wave length of the electrons. At Scherzer CTF has a long plateau resulting in maximal information transfer from the exit wave to the image wave (section 4.2.2).

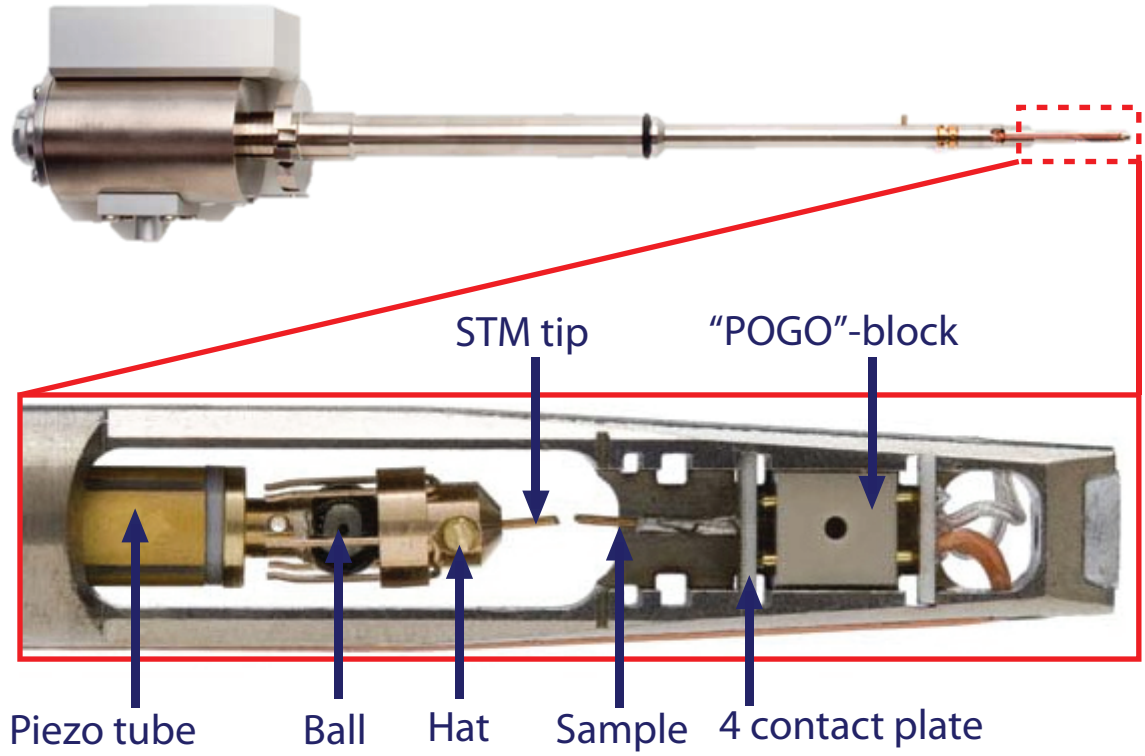

Figure 4.2.: Nanofactory^{TM} STM-TEM holder for FEI microscopes. Marked area (dashed line) on the side-view (top image) is shown magnified in the top view (bottom image). The electron beam direction is perpendicular to the figure plane. The pictures adopted from [89].

movement of the STM tip. The fine movement can be achieved by bending the piezo tube. On the opposite side a sample is mounted on a ceramic plate with 4 electric contacts. The plate can be changed after retracting a so-called POGO-block. Voltage signals can be applied between the sample and the STM tip.

The idea of the electromechanical resonance technique lies in the excitation of the resonant vibrations of a nanowire by applying an alternating electrical field between the nanowire (clamped at one or two ends) and an STM tip. The frequency of the excitation is set to be the same as the Eigen vibration frequency of the nanowire in the case of soft damping. The resonance frequency of the fundamental resonance can be used to calculate Young's modulus of the nanowire with the help of equation 2.30.

The following requirements should be met to employ the electromechanical resonance method:

- The area of interest of the sample should be transparent for the electron beam.
- The nanowires must be fixed with at least one end to the substrate.
- The size of the sample (with a substrate) should not exceed 3 mm in lateral directions and 2 mm in the direction of the electron beam.

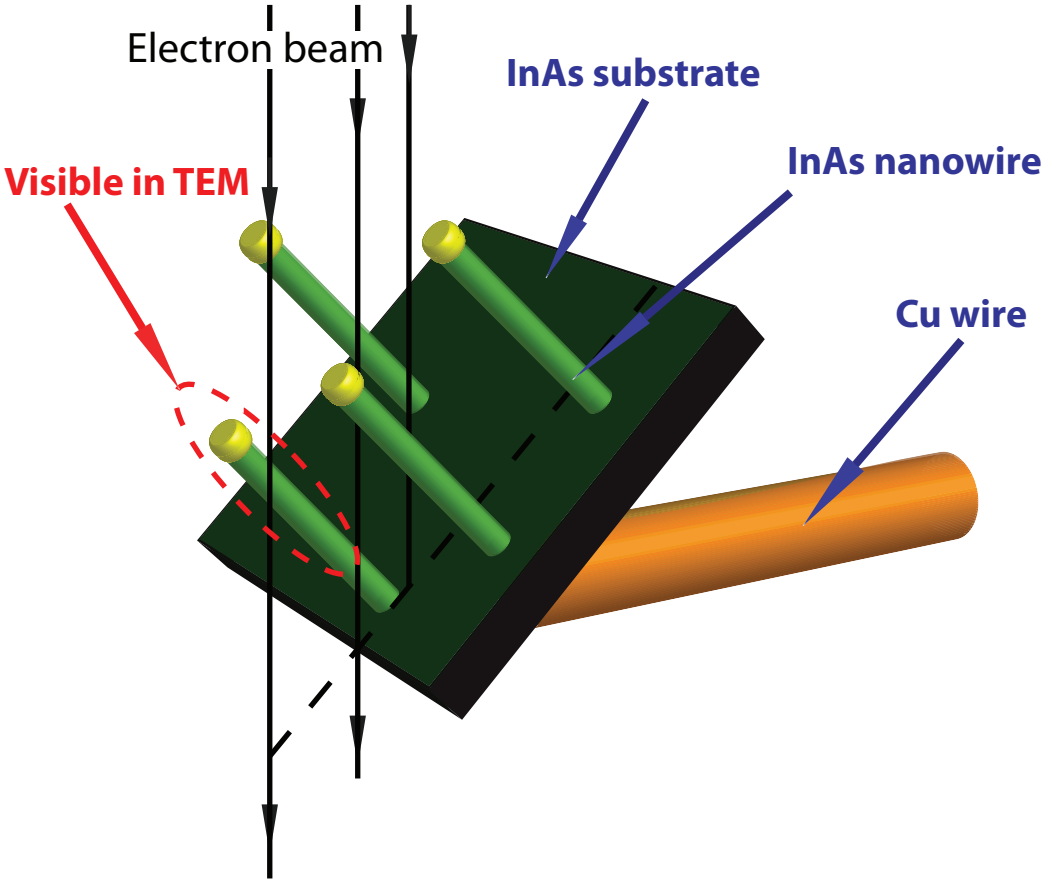

Figure 4.3.: A scheme of the nanowire sample for electromechanical measurements. The nanowires are investigated at the edge of the substrate which produces a shadow in the bright field TEM micrograph. The visible part of the nanowire is marked with the dashed red ellipse.

- The nanowires should be aligned so that one of their zone axes is parallel to the electron beam.[5]

- It should be possible to approach the nanowire with the STM tip of the STM-TEM holder.

To fulfill these requirements a piece (2 x 2 mm^2) was cut from the substrate with the as-grown nanowires. This piece was glued with conductive epoxy to a copper wire with a diameter of 0.25 mm and length of about 4 mm. The angle between the wire and the substrate was set either to 45 ° or to 63°. This increased the probability to find a nanowire "in Bragg condition" (see appendix C for more details on sample preparation). The copper wire has to be inserted in the housing on the ceramic plate of the holder in a way that, the nanowires, which are at the edge of the substrate, are visible in the TEM (see figure 4.3). Due to the epitaxial growth of the nanowires on the InAs substrate their attachment is strong enough to consider them fixed with one end to the substrate.

[5]This requirement is essential to allow structural characterization of the nanowire when elastic properties are investigated in-situ in parallel.

Gold STM tips with an apex diameter between 10 and 200 nm were used as counter-electrodes to produce an alternating electrical field. The detailed description of the STM tip preparation process can be found in appendix C.
The electromechanical resonance experiment was performed with the following steps:

1. Selection of a single standing nanowire which can be tilted so that one of its zone axes is parallel to the electron beam;
2. Structural investigation of the nanowire;
3. Determination of the length of the nanowire;
4. Approaching the nanowire with the STM tip and establishing a physical contact;
5. Positioning of the STM tip at a distance of 0.2 - 1 μm from the nanowire;
6. Sweeping the bias voltage frequency (0.1 - 20 MHz) with simultaneous visual detection of the nanowire vibrations in the TEM until the resonance is found;
7. Checking other harmonics, determination of the fundamental resonance, recording the amplitude-frequency characteristics of the nanowire vibrations close to the resonance.

For **step 1** it is important to use electron diffraction (either SAED or convergent beam electron diffraction (CBED)[83]) to check the orientation of the nanowire at different tilt angles and select only those nanowires which can be oriented almost parallel to electron beam with one of their zone axes. After that, the SAED pattern is recorded (**step two**). When possible a bright field image of a nanowire oriented so that stacking faults are visible should be recorded.

The measurement of the nanowire length (**step 3**) is complicated due to the following reasons: a part of the nanowire is shadowed by the substrate (see figure 4.3); the nanowire is not parallel to the imaging plane, and its projection does not give its true length. The secondary electron (SE) detector in STEM mode in the Phillips CM12 TEM was used to acquire micrographs on which the entire nanowire is visible (figure 4.4 a).[6] The real length of the nanowire was obtained by fitting the projection length L_S as a function of the tilt angle α with the equation:

$$L_s = L\sqrt{1 - \varphi sin^2(\alpha + \theta)}, \text{ where } \varphi = sin\beta, \tag{4.1}$$

β is the angle between the nanowire and tilting axis, θ is a phase, L is the nanowire length. L, φ and θ are fitting parameters which are restricted to the intervals $[max(L_S); \infty)$, $[-1; 1]$ and $[-\pi; \pi]$ respectively. A tilting series of SE micrographs in the range of ±45° was acquired, and the lengths of the projections were measured directly from the micrographs. Figure 4.4 b shows

[6] In this case the principle of image acquisition is the same as in SEM but it is done in-situ in the TEM. Transparency of the sample for electrons in this case is not necessary.

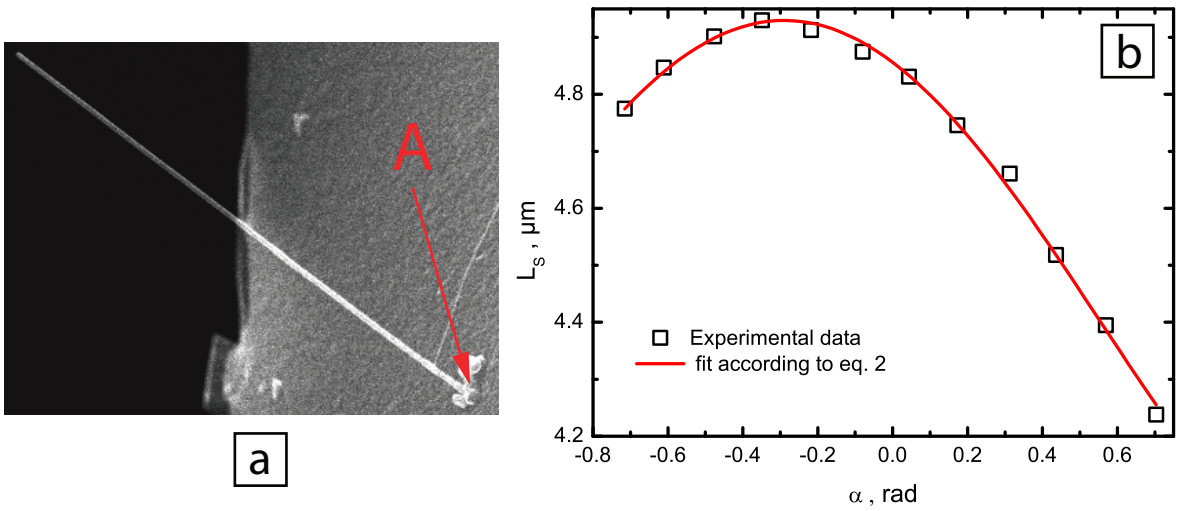

Figure 4.4.: STEM micrograph of an InAs nanowire sticking out from the substrate (a). Black area on the left is empty space, the nanowire base at the substrate is marked with "A". The part of the nanowire which is shadowed in bright field TEM micrograph by the substrate is twice brighter than the other part. Graph b shows the dependence of the projection length of the nanowire on tilt angle α (black squares). The fit according to equation 4.1 is shown with the red line. The fitting parameter L (real length of the nanowire) is equal to (4.93±0.01) μm.

a typical dependence of the wire projection length on the tilting angle (black squares) and the fit (red line) according to equation 4.1.

The approach of the nanowire with an STM tip is difficult, since the TEM image shows only a 2D projection. It is most important in the **4th step** to place the tip at the same height as the nanowire and to bring the nanowire at the eucentric height of the microscope. After that one can use the "alpha-wobbler" in the microscope [7] to bring the tip at the eucentric height too. The fine adjustment can be done by focusing the microscope first on the nanowire and recording the defocus value Δf_{NW} than focusing the microscope on the tip and recording the defocus of the tip Δf_{tip}. The height difference between the nanowire and the tip will be $\Delta Z = \Delta f_{tip} - \Delta f_{NW}$ which can be added to the current position of the tip to set it at the same height as the nanowire. After the tip touched the nanowire, they should be separated laterally from each other (**step 5**). The alternating (AC) bias voltage[8] applied between the nanowire and the tip produces an AC electrical field which excites vibrations of the nanowire. During the frequency sweep (**step 6**) the increase of the vibration amplitude is observed by TEM imaging. After a resonance is found at the frequency f_{r0} the frequencies $2f_{r0}$ and $(1/2)f_{r0}$ should be checked also. The highest of those three frequencies which shows a resonant vibration should be used to confirm the fundamental resonance (**step 7**). At the fundamental Eigen resonance the amplitude of the nanowire vibrations should be proportional to the amplitude of the exciting

[7] Alpha-wobbling is a periodical change of a sample holder tilt angle (alpha) between +15° and -15° for example. At the eucentric height the movement of the sample projection during the wobbling vanishes.

[8] generated using Keithley 3390 Signal Generator

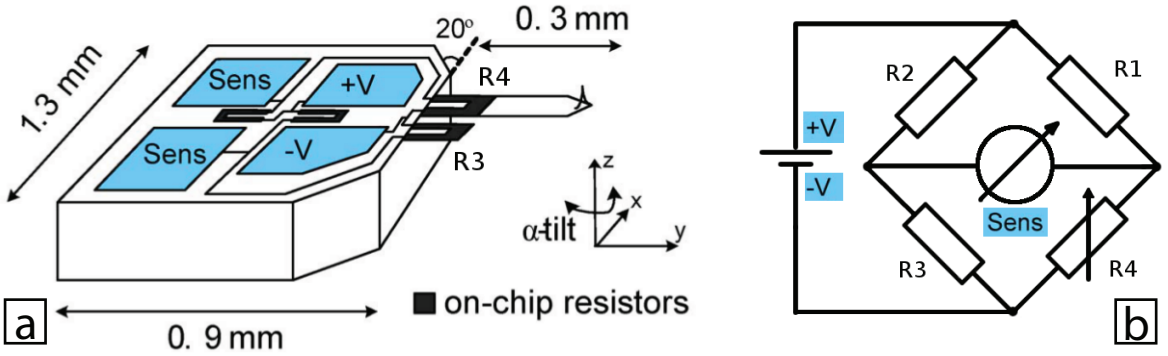

Figure 4.5.: A schematic view of the AFM sensor a. With black marked on-chip resistances: R_3 and R_4 built in a reference cantilever and an AFM cantilever respectively. Electrical contact pads marked with blue. The electron beam is along the X-axis, the Z-axis is parallel to the holder axis. Figure b shows the electrical circuit of the measurement technique. Resistances R_4 and R_3 are connected in a Wheatstone bridge so that they compensate each other when there is no load applied. When the AFM tip is loaded, the resistance R_4 changes, which can be detected as a disbalance of the bridge. Figure (a) is adopted from [90], figure (b) is adopted from [91].

field. The amplitude-frequency characteristics is recorded by sweeping the frequency around the fundamental resonance ±0.5 % and simultaneously recording the TEM micrographs. The frequency resolution of the experiment is limited by the accuracy of the amplitude measurement (≈ 10 %) but not by capatibilities of the signal generator. Therfore, 0.1 kHz was the maximal frequency resolution used in the experiment. Possible artifacts of the measurement (e.g. non-planar vibration of the nanowires) will be discussed together with results in section 5.2.

4.3.2. Bending method

Another method to study elastic properties of the nanowires which was implemented in this work is the analysis of the bending behavior of a single nanowire. A Nanofactory ^{TM} atomic force microscopy (AFM) sample holder for TEM was used to bend the nanowires and measure the load force. The AFM-TEM sample holder consists of the same parts as the STM-TEM holder (see figure 4.2 and section 4.3.1) but the sample is inserted into a movable hat and the 4-contact ceramic plate is substituted by an AFM chip. Figure 4.5 a shows the AFM sensor, which consists of the chip and two cantilevers (R_3 and R_4) which are sticking out of it. The reference cantilever R_3, which does not have a tip at the end, is connected opposite to the cantilever R_4 to minimize noise due to charging in the TEM or vibrations. The cantilever R_4 is used for measurement of the load force which should be applied perpendicular to its tip. Both cantilevers have implanted resistances which change when the cantilevers are bend (piezoresistive effect). The resistances are connected in the Wheatstone bridge circuit as it is shown in figure 4.5 b, and the signal can be detected only if a force is applied to one of the cantilevers, in this case to R_4.

The AFM tip in this experiment was used to apply a loading force to an InAs nanowire

by pressing the substrate with an attached nanowire against the cantilever. The bending of the wire and in certain cases also microscopic strain directly was observed using TEM imaging. The scheme of the experiment is shown in figure 4.6. To perform a successful experiment, the sample should fulfill the following requirements:

- The nanowires should be fixed with one end to the substrate;
- The complete nanowire should be visible in bright field TEM mode (from the free end till the fixation point);
- The sample should not exceed 2 mm in any dimensions;
- It should be possible to reach a nanowire with an AFM tip;[9]
- Ideally, the nanowires should be parallel to the holder axis, to make it easy to align different zone axes of a nanowire parallel to the electron beam.

The dielectrophoretic deposition (DEP)[92] was used to prepare the InAs nanowire samples. The idea of the method is to use an electrical gradient field to align the nanowires parallel to the field in a place with maximal gradient [92]. Pieces of copper TEM grids (size 1x2 mm) were used as the electrodes for DEP. The grids were glued to the copper wires (0.25 mm in diameter and about 4 mm long) with conductive epoxy so that the wire is parallel to the grid bars (see figure 4.7 a). The grids were aligned in an optical microscope so that the bars of one grid are opposite and parallel to the bars of the other grid. The distance between the bars should be limited to a few microns. The nanowires were cut from the substrate and dispersed in a dielectric solution (ethanol, isopropanol or deionized water, typically). The drop of the solution was placed on the parallel electrodes, and an alternating voltage was applied across the electrodes (6 V at 10 MHz) [93]. After deposition of the solution with nanowires the solution was dried with a flow of hot air which temperature is not higher than 70°C. A more detailed description of the DEP sample preparation can be found in appendix C. After DEP the ends of the TEM grid bars are coated with the nanowires that stick out parallel to the bars, thus, parallel to the sample holder axis (refer to figure 4.7 b). The nanowires were found to be strongly fixed by adhesion forces at the edge of the bars.

To analyze the mechanical properties of the nanowires following steps were taken:

1. Selecting a nanowire, structural investigation of the nanowire, approaching the wire to the AFM tip, establishing mechanical contact;[10]

[9] This requirement differs from its analogue in section 4.3.1 due to geometrical differences of the tips. The AFM tip is about 2-3 μm long, and it is attached to a cantilever. Therefore, objects longer than 3 μm will touch the cantilever before the nanowire will touch the tip when approaching the nanowire.

[10] This step is essentially the same as steps 1,2,4 in the electromechanical resonance experiment described in section 4.3.1. The only difference is that in the AFM-TEM sample holder the movable part is the sample, and the AFM tip is steady.

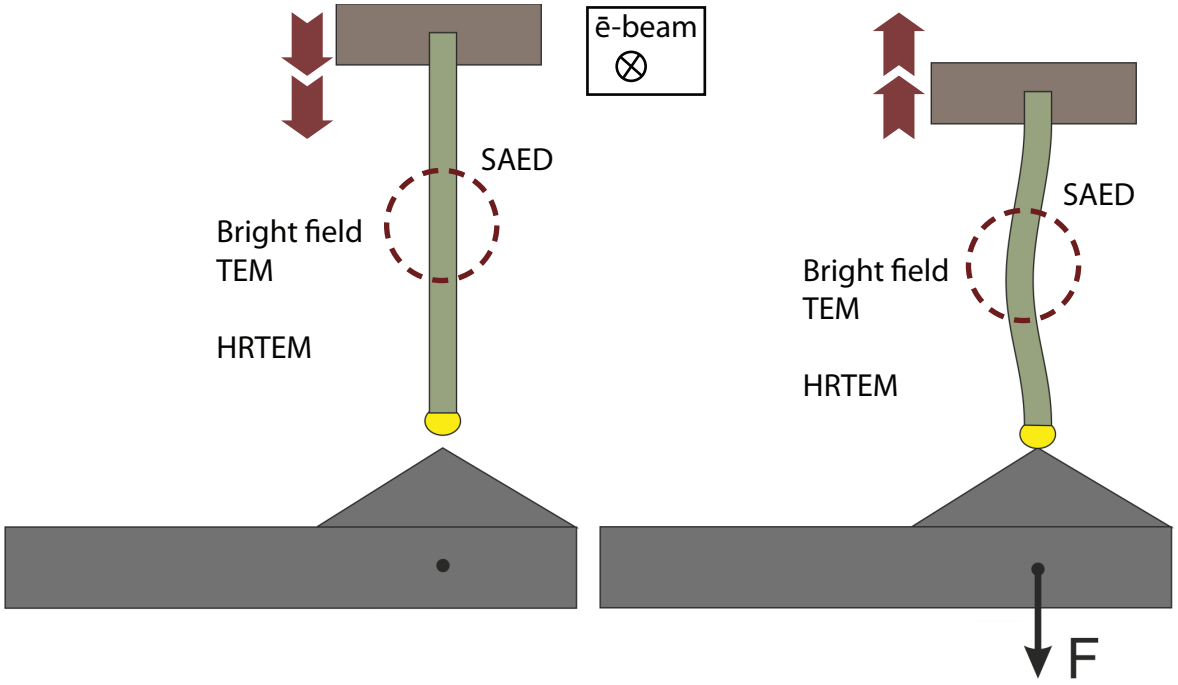

Figure 4.6.: Scheme of the AFM bending experiment in-situ in TEM. Initially (left) the AFM cantilever is not in contact with a nanowire, and the morphological and structural examinations are performed. The substrate with clamped nanowire is pushed against the AFM cantilever (right) and simultaneously morphological and structural characterizations are performed.

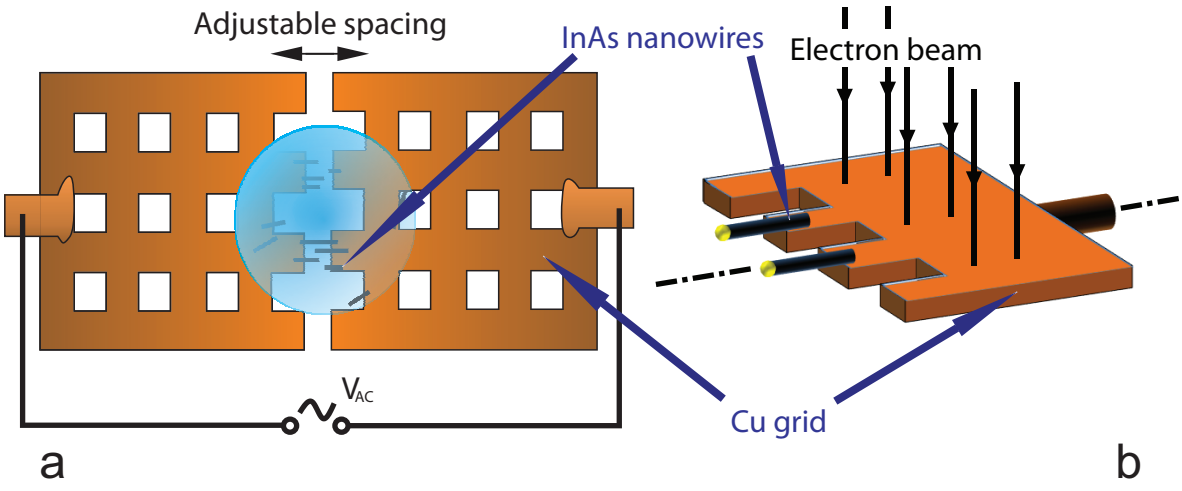

Figure 4.7.: (a) Dielectrophoretic deposition scheme. The drop of solution with InAs nanowires is deposited on Cu electrodes aligned parallel to each other. The alternating voltage is applied between the electrodes to produce electrical gradient field between the electrodes. (b) Scheme of the alignment of nanowires on the Cu grid with respect to the sample holder axis (dashed-dotted line) and the electron beam of the TEM.

2. Two direction force-displacement measurement with simultaneous video capture in TEM;

3. Acquisition of SAED pattern in the not loaded state, one direction force-displacement measurement, acquisition of SAED pattern at the loaded state, reversed force-displacement measurement.[11]

In the force-displacement (F-d) measurement the sample is moved against the AFM tip and the resulting force acting on the AFM cantilever is detected. In **step 2** the sample moves towards the AFM tip (”forward”) until it reaches a position defined by the user, and than it moves back until it reaches the original position. Since in this case the maximal load is defined by maximal displacement, the two direction F-d measurement was repeated every time increasing the maximal displacement until the force reached several hundreds of nN. The speed of the process is defined by the acquisition time which was normally set to 1800 ms for the full cycle. The video capture was performed with a TV camera which is installed at the entrance of the GIF system of the Tecnai F20 TEM. The start of the force-displacement experiment was synchronized with the start of the video capture to correlate the force acting on the AFM cantilever with the corresponding video frame. The analysis of the data requires the determination of the distance between two ends of the nanowire at a given force, which was easily performed on the video snapshots.

During the ”one direction” F-d measurement (**step 3**) the sample is moved towards the AFM tip until it reaches the maximal displacement defined by the user. This position is kept (the wire remained loaded) and the SAED pattern, HR-TEM image or low magnification TEM micrograph is acquired. For SAED imaging the selected area (SA) aperture was inserted in the TEM column before the start of the F-d experiment, to avoid vibrations which results in the loss of contact between a nanowire and the AFM tip. After the first F-d measurement the SA aperture was moved to the same position related to the wire as at the start of the experiment. After acquisition of the SAED pattern, the F-d measurement was repeated in the reversed direction: the sample moves backwards to the initial (not loaded) position. Again the SAED pattern was recorded to check for irreversible structural changes of the nanowire. A sample F-d curve is shown in figure E.2 *d*. During all F-d experiment the force is measured by the calibrated AFM cantilever. The displacement indicated in the graph is the total displacement of the piezo. Since the AFM cantilever bends during the loading, the total displacement d_{total} is the sample displacement with respect to the cantilever d_{sample} (which after contact is equal to sample deformation) plus the AFM tip displacement d_{cant}. More details about the bending experiment and data analysis can be found in appendix E.

[11] It also makes sense to perform the same step but replace the SAED by HR-TEM image acquisition or low resolution TEM imaging. One should note here that both SAED and HR-TEM acquisitions can be done only if the nanowire is oriented with its zone axis parallel to the electron beam.

4.3.3. Two-point contact technique for resistivity measurements

The electrical resistance of InAs nanowires was measured in-situ in a Philips CM12 TEM by a two-point contact technique. A bias voltage is applied at the ends of the nanowire and the electrical current flowing through the system is measured. This method can only give reasonable results if the total contact resistance is several orders of magnitude smaller than the resistance of the object. If the contact resistance is of the same order, the so called **transfer length method** (TLM) has to be used. The length L of the object is varied and the total resistance R_{total} is measured. Assuming that the total contact resistance R_c is not changing from one measurement to another, and the resistance depends linearly on the length (object resistivity ρ and its cross section area A are constant), the slope of $R_{total}(L)$ is equal to ρ/A. The extrapolated intersect of the $R_{total}(L)$ dependence at L=0 is equal to the total contact resistance. The application of these methods will be presented later in section 5.3.

The STM-TEM sample holder which is described in section 4.3.1 was used to establish a contact to a free end of a nanowire grown on a substrate and to measure its total resistance (including contact resistances). In this case the sample must be a good conductor (contact resistances should not exceed several tens of Ohms). The other requirements for the sample are essentially the same as in section 4.3.1. Thus, the nanowire sample was prepared utilizing the same method as for electromechanical resonance measurements, cutting a substrate with nanowire and investigating the wires grown on the edge of the substrate (refer to section 4.3.1 and appendix C). An electrochemically etched gold tip was used to contact the free end of a nanowire. The two point contact measurement was performed utilizing the following steps:

1. Selecting a nanowire, structural investigation of the nanowire, measuring the nanowire length, approaching the nanowire with an STM tip, establishing physical contact;[12]
2. Improvement of the electrical contact between the STM tip and the nanowire;
3. Acquisition of current-voltage (I-V) curves, while the TEM electron beam is switched off;
4. (Optional) Acquisition of I-V curves under different TEM illumination conditions and different magnetic fields (i.e. TEM objective lens current);
5. (Optional) Acquisition of I-V curves under different loads of the nanowire.

After the physical contact between a nanowire and an STM tip is established, it must be improved to achieve a contact with low electrical resistance (**step 2**). The electron beam of the TEM was focused (spot radius is about 15 nm, electron flux 4.4 x 10^7 $\bar{e}$/(nm^{2}s)) on the contact

[12] This step is identical to steps 1-4 in the electromechanical resonance experiment procedure (described in section 4.3.1).

area and voltage pulses (amplitude 3V, duration 10 ms, frequency about 0.1 Hz) were applied between the nanowire and the tip. This treatment results in a locally increased mobility and interdiffusion of gold atoms at the tip[13] of the nanowire and the STM tip. After 5-15 pulses the total resistance decreased drastically (several orders of magnitude).

To acquire the I-V curves (**step 3**) the bias voltage was swept starting from a minimal (negative) value up to maximal positive value (typically, the blue curve in graphs of section 5.3) and back to the minimal value (red curve). The resistance was calculated from the slope of the I-V curves. To avoid effects of electron irradiation, the electron beam was switched off by closing a shutter which was placed before the condenser lens system of the TEM.

To check the influence of the magnetic field and electron irradiation on electron transport (**step 4**) the I-V curves were recorded for different TEM magnifications and electron doses. In low magnification (LM) mode the magnetic field at the sample is approximately 70 mT [79] and experiments were performed at fluxes: 0 and 8800 $\bar{e}$/(nm^{2}s). In medium magnification (SA) mode the magnetic field is approximately 1 T [79] and the experiments were done at the same fluxes.

To record I-V curves of the InAs nanowires at different loads the STM tip was pushed against the nanowire (**step 5**). In this case the load can not be measured directly but it can be estimated using the results of the bending experiments described in sections 4.3.2 and 5.2.

4.3.4. Electron holography of InAs nanowires under applied bias voltage

The spatially resolved measurement of the electrical potential in the InAs nanowires was performed in-situ in a FEI Titan Analytical 80-300ST TEM operating at 120 kV employing an electron holography technique combined with electrical biasing of the sample.

The electron holography technique is a direct analogue of optical holography. Its basic idea is to combine two or more coherent electron waves to form an interference hologram [94, 95]. The hologram carries information on the complex electron wave function, whose phase and amplitude are changed by the sample. In off-axis electron holography (the most common holography type) a biprism located below the objective lens system of the TEM (figure 4.8 a) is used to overlap a reference (vacuum) electron wave with the one passing through an object. The biprism splits an electron beam into two halves, one wave passes through the sample the other through vacuum. The interference pattern can be recorded as usual TEM micrograph. It consists of fine fringes. The point resolution of normal magnification holography can reach 1 nm [96]. The phase shift of the electron wave after it has passed through a sample depends on

[13]The Au seed particles which are used in the nanowire synthesis (see section 4.1) remain on top of the nanowire. Further information about nanowire morphology and composition can be found in section 5.1

the mean inner potential[14] (MIP) of the specimen, in-plane magnetic field, electrical fields and dynamic diffraction effects. If the dynamic diffraction effects can be neglected, the phase shift ϕ can be written as:

$$\phi(x) = C_E \int V(x,z)dz - \frac{e}{\hbar} \int \int B_\perp(x,z)dxdz, \tag{4.2}$$

where x is a direction in the sample plane, z the electron beam direction, e the electron charge, $\hbar$ the reduced Planck constant, $B_\perp$ a component of the magnetic field induction perpendicular to x and z [96]. The inner electric potential of the sample $V(x,z)$ can be written as a sum of MIP and the external electrical potential $V(x,z) = V_0(x,z) + V_{ext}$. The interaction constant C_E depends on the kinetic and rest mass energy of the electrons, E and E_0, and on the wavelength λ [96]:

$$C_E = \frac{2\pi}{\lambda E} \frac{E + E_0}{E + 2E_0}. \tag{4.3}$$

For the situation when magnetic and electrical fields do not vary with z, and the MIP does not vary with z and x, the phase can be rewritten as:

$$\phi(x) = C_E(V_0 + V_{ext}(x))t(x) - \frac{e}{\hbar} B_\perp(x)t(x), \tag{4.4}$$

where $t(x)$ is the specimen thickness. From such holograms the magnetic and electric field distribution can be reconstructed. The reconstruction in the considered aberration free case would deliver the object modulated wave directly. In reality, due to coherent aberrations of the TEM lens, the hologram contains a modified object wave (so called image wave; see figure 4.8 *b*) [97]. The hologram, which contains the pure object wave, can be extracted by dividing the object hologram by the vacuum hologram. Both should be acquired at the same imaging conditions.

The electron holography was applied to study local variations of the resistance of a nanowire by detecting the electrical potential in the nanowires with an electrical current flowing inside. The experimental scheme is shown in figure 4.8 *c*. The only difference from conventional off-axis electron holography is that an electrical current is sent through the nanowire. The STM-TEM sample holder, which is described in section 4.3.1 was used for the measurement. The experiment was performed inside the Titan TEM[15] which is equipped with an electrostatic biprism. The biprism is installed in the place of the selected area aperture. It can be moved laterally and rotated. The nanowire sample was prepared using dielectrophoretic deposition on a copper TEM

[14] Mean inner potential is a volume average of the electrostatic potential of atoms in a solid: $V_0 = 1/\tilde{V} \int_{\tilde{V}} V_{atom} dxdydz$, where x, y, z are coordinates and $\tilde{V}$ is the volume. The physical meaning is an average electron scattering constant which is a direct analogue of the index of refraction in conventional optics.

[15] The experiment was done in Center for Electron Nanoscopy (CEN), Technical University of Denmark (DTU) in Kgs. Lyngby, Denmark.

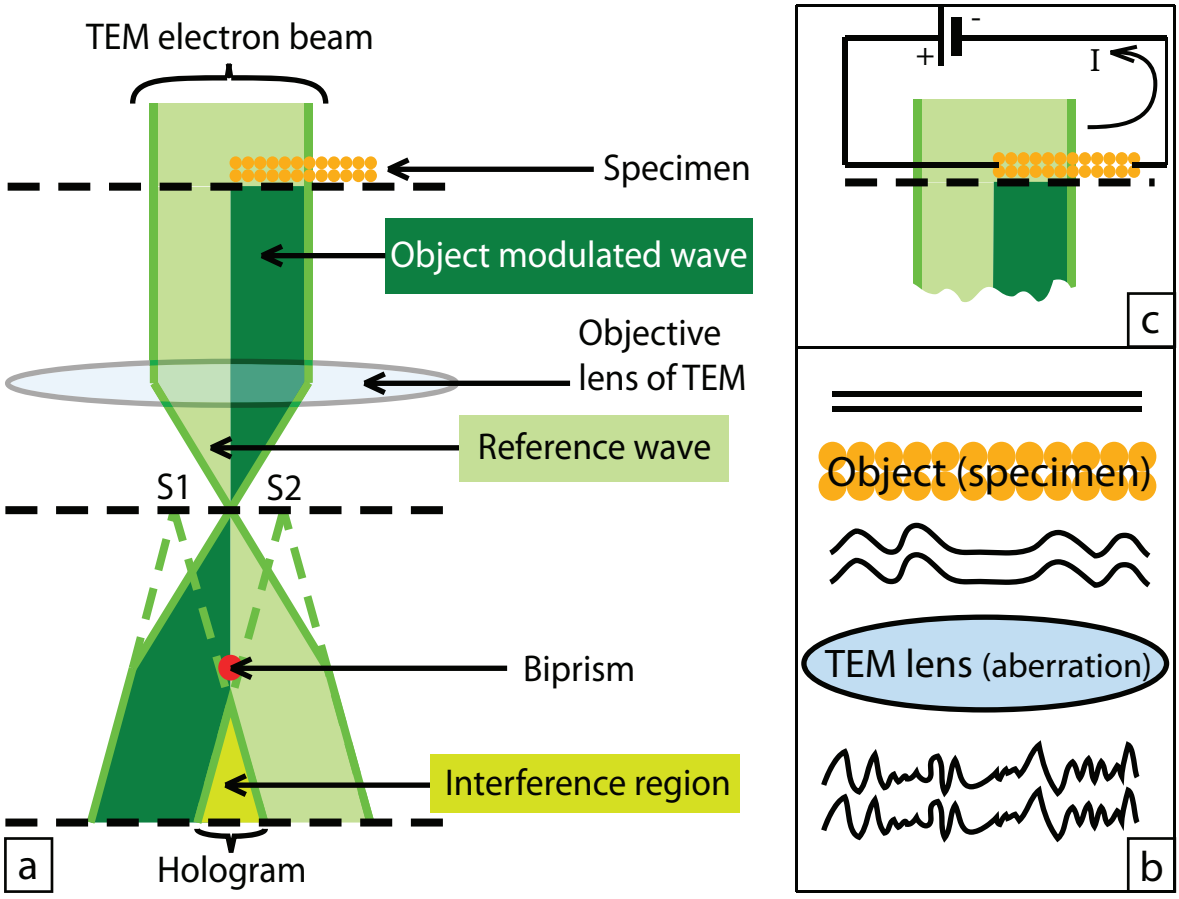

Figure 4.8.: (a) A scheme of off-axis electron holography in TEM. Half of the TEM electron beam penetrates the specimen and contains the object modulated wave, while the other half goes through vacuum and remains unchanged. The biprism situated under the objective lens overlaps those two beams. In the interference region a hologram can be detected. S1 and S2 show two sidebands in the back focal plane of the objective lens which corresponds to the object wave and reference wave respectively. The image is adapted from Lehmann. (b) Scheme shows the modulation of the object wave due to coherent aberrations of the TEM lens. From top to bottom: incident plane electron wave, specimen, object modulated wave, TEM lens which introduce coherent aberrations, image wave. (c) Schematic representation of the electron holography experiment with an electrically biased sample. Current I is flowing through the sample.

grid as described in section 4.3.2 and appendix C. Morphology and atomic structure of the samples were pre-characterized in the Philips CM12 and Tecnai F20 microscopes using the same sample holder. To maintain the same crystallographic orientation of each nanowire after the pre-characterization, the samples were permanently mounted on the 4-contact ceramic plate of the holder. The transport and exchange of the samples was performed together with the ceramic plates.

Before the experiment the microscope was switched into Lorentz mode, which provides an increased field of view. The electron beam of TEM was stigmatized by changing the condenser astigmatism to obtain an elliptic and highly elongated in one direction shape. The biprism was set perpendicular to the elongation direction. This configuration maximizes the overlapping area of the beams. A constant voltage of 80-140 V was applied to the biprism. The stigmators and biprism were set parallel or inclined with a small angle with respect to a nanowire, since only half of the electron beam should penetrate the object. Further, the experiment was performed in the following steps:

1. Selection of a nanowire, acquisition of bright field images;
2. Rotation of the nanowire to minimize diffraction contrast;
3. Acquisition of the wire hologram and reference hologram without applied bias voltage;
4. Approaching the nanowire with an STM tip and establishing physical contact between them;
5. Improvement of electrical contact between the STM tip and the nanowire;
6. Acquisition of the wire hologram and reference[16] hologram at different bias voltages and recording I-V curves;
7. Retraction of the STM tip and acquisition of reference holograms at 0 voltage and bright field images of the nanowire.

Since dynamic diffraction effects can affect phase shift and the goal was to measure the electrical potential at stacking fault defects in the nanowires, the wire was tilted away from the zone axes to minimize the contrast of stacking faults (**step 2**). Otherwise, small tilts of the electron beam due to the applied bias voltage could have resulted in a change of the diffraction contrast giving rise to dynamic diffraction effects, which could result in additional unwanted phase shifts. To acquire reference holograms (**steps 3** and **6**) the sample was shifted away from the electron beam. To approach the STM tip to the nanowire (**step 4**) the biprism was retracted and condenser stigmators were set so that the electron beam is circular. The contact was established

[16] In some experiments reference holograms were acquired only once during the step 3

and improved (**step 5**) the same way as described in section 4.3.3. The contact should be kept unchanged during all manipulations of **step 6**, since the data analysis required some reference points (to align an intensity profile) which are unchanged for different voltages. Since the microscope stage produced vibrations large enough to break the contact, the sample was not moved after that any more. Therefore, in most experiments in step 6 only holograms of a nanowire were acquired by changing the bias voltage in steps of 0.5 V between -2.5 V and +2.5 V without taking the reference holograms. The **step 7** was performed to compare the nanowire before and after the experiment to reveal any changes in nanowire morphology or crystal structure due to beam damage, for example.

The holograms were reconstructed by the following procedure.

- Prior to FFT a 3d order Hanning filter[17] was applied. Figure 4.9 *a* shows the original hologram and *b* the filtered image.

- FFT of the hologram is shown in figure 4.9 *c*. The object side band (marked with red) was selected and recentered for calculation of the inverse Fourier transformation which represents the image wave (figure 4.9 *d*).

- The vacuum reference wave (figure 4.9 *e*) reconstructed the same way as described above was subtracted from the image wave (figure 4.9 *f*).

- The complex image after inverse Fourier transformation contains both phase ϕ and amplitude A in its r real and i imaginary parts [96]:

$$\phi = arctan(i/r), A = \sqrt{r^2 + i^2} \tag{4.5}$$

  Amplitude and phase images are shown in figures 4.9 *g* and *h*, respectively.

- To change the appearance of the phase image it can be transformed into a contour map (figure 4.9 *i*) using the following equation:

$$I_{contour} = cos(4I_{phase}), \tag{4.6}$$

  where $I_{contour}$ is the intensity of the contour map and I_{phase} is the intensity of the original phase image. In the contour map image the phase shift between two closest black lines is equal to $\pi/2$.[18]

[17] Hanning filter is a so-called raised cosine filter which uses Hann window function, for more details please refer to [98].

[18] All data manipulations were done using Gatan DigitalMicrograph^{TM} software [99] with several self-made and open-source scripts.

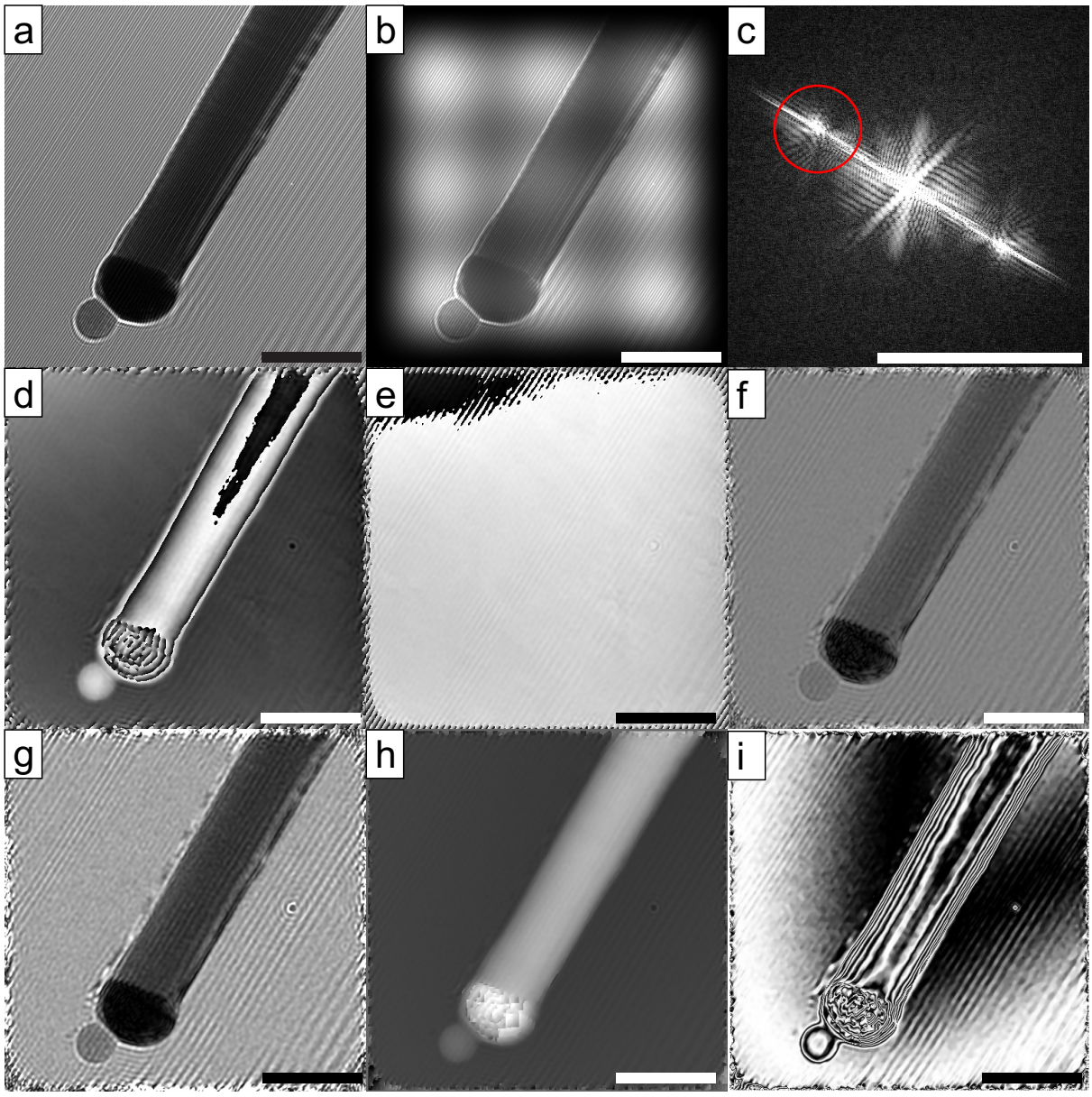

Figure 4.9.: (a) Hologram of an InAs nanowire; (b) filtered hologram using Hanning filter; (c) FFT of figure (b), the object side band is marked with red; (d) inverse FFT of the side band; (e) reference wave; (f) object wave which is a result of the division of the image wave (d) by the reference wave (e); (g) amplitude of the object wave (f), and (h) phase of the object wave; (i) contour map retrieved using equation 4.6. The scale bar at all real space images (a, b, d-i) is 100 nm and in the FFT (c) is 0.5 1/nm.

In some cases, when subtraction of external electrical fields is required, the phase images were processed in the following way: select the vacuum region in the image, interpolate this selection on the whole image, subtract interpolated image from the original one. The interpolation was done using the Delaunay triangulation[19] algorithm and linear interpolation method in MatLab.

[19] Is a triangulation method of an underlaying of a mesh for computations, which maximizes minimal angle of all triangles in the mesh [100].

5. Results and discussion

5.1. Morphology, composition, atomic structure, stacking fault defects of InAs nanowires

In this section I described the results of the experimental studies of two and three dimensional morphology, chemical composition and atomic structure of InAs nanowires. The study of the atomic structure reveals presence of twin defects in the nanowires. The precise atomic structure of the twin defects is discussed in the last subsection.

5.1.1. Morphology and chemical composition

The morphology of the nanowires was studied by SEM and TEM, as described in subsections 4.2.1, 4.2.2. Figure 5.1 *a* show typical SEM micrograph of InAs nanowires. About 70 % of the nanowires grow perpendicular to the substrate, while about 30 % grow in different directions. The perpendicular wires are expected to grow in the $\langle 100 \rangle$ direction on the (100) substrate. To determine the crystallographic direction and the atomic structure of the nanowires we performed structural studies in the TEM. Low magnification TEM images of the InAs nanowires (figure 5.1 *b*) confirm that the gold catalysts remain on top of the nanowire. For further mechanical and especially electrical characterization of the nanowires it is important to know if the gold is partly diffused into the nanowires which will be discussed in the next paragraph. It was also found by TEM that up to 30% of the nanowires are tapered. Only untapered nanowires were used in all further investigations.

The composition of the nanowires was checked by STEM combined with EDXS as it was described in section 4.2.5. The EDX line profile was recorded along the red line in figure 5.2 *a*. The X-Ray counts are plotted against the position of the electron beam in figure 5.2 *b*. The measurement shows that all gold is concentrated on top of the nanowire (point (1) in figure 5.2 a) and mixed with 25% of In and a small amount of As (<5%). We have not detected any gold signal from the body of the nanowire (point (2) in figure 5.2 *a*). In and As in the nanowire body are distributed equally, 50% to 50% (within 1% error bar). The EDX mapping across an area of 140 × 140 nm confirms that both In and As are homogeneously distributed inside the nanowire. During the growth the gold particle forms a liquid droplet which is supersaturated with In and As

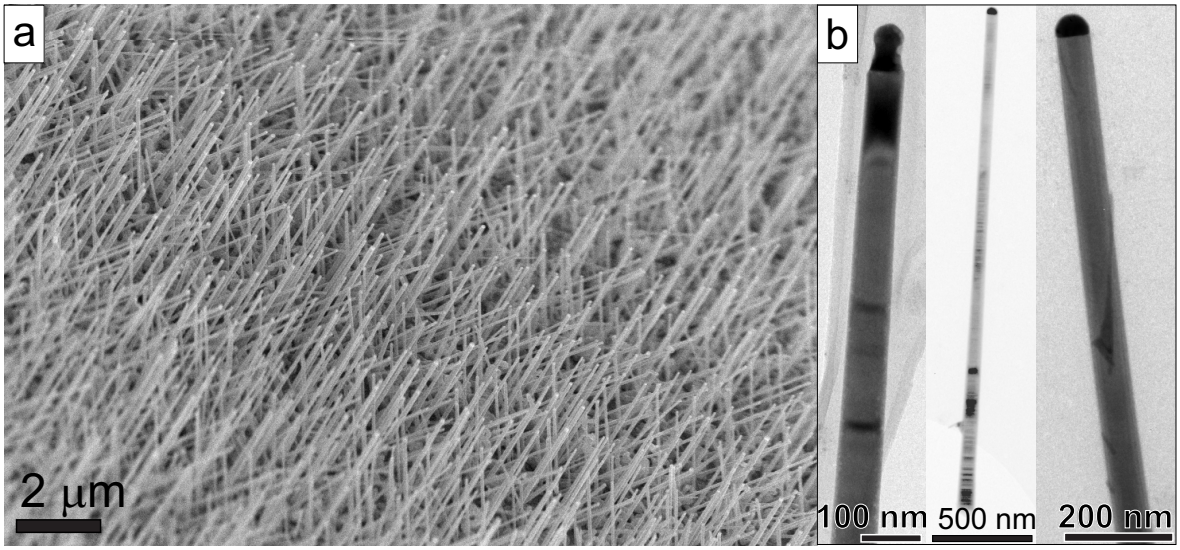

Figure 5.1.: (a) SEM micrograph of as-grown InAs nanowires on InAs substrate. (b) Low magnification TEM bright field micrographs of the InAs nanowires deposited on a copper TEM grid covered with holey carbon film.

[101]. Since after the growth the precursor flow is stoped simultaneusly with the ramping down the reactor temperature, both In and As have time to desolve from the particle befor it solidifies. However, the equilibrium preasure of As is higher than In and, thus, it escapes from the particle faster than In [80]. The fact that the nanoparticle surface is covered with indium (figure 5.3) or indium oxide can be also atributed to the end of the growth of the nanowires. Due to decrease of the temperature during the desolution In precipitate at the nanoparticle surface forming a thin amorphous shell. The simmilar result was obtained by F. Glas and coworkers [80]. The following paragraph is dedicated to a detailed study of the crystal structure of the nanowires.

5.1.2. Crystal structure of InAs nanowires

The crystal structure of InAs nanowires was studied using an FEI Tecnai F20 TEM. To determine the atomic structure the HR-TEM images were recorded and fast Fourier transformations (FFT) of the HR-TEM images were analyzed as discussed in section 4.2.2. We found three different types of nanowires which are characterized by different atomic structures and growth direction [86]. About 70% of the nanowires have cubic Zinc-Blende atomic structure with ⟨100⟩ growth direction (it correlates with the amount of the nanowires that grow perpendicular to the substrate, see previous section). Those nanowires will be called ”type 1”.

A second type of nanowires (”type 2”) has an alternating Zinc Blende and Wurtzite structure separated by stacking faults. The defect planes are perpendicular to the ⟨111⟩ growth direction, and will be discussed more intensively in section 5.1.4. The stacking faults are easy to recognize because of their stripe-like contrast in the TEM micrographs and double reflexes in the electron diffraction pattern (figure 5.4 *a*). The superposition of [-110] diffraction patterns

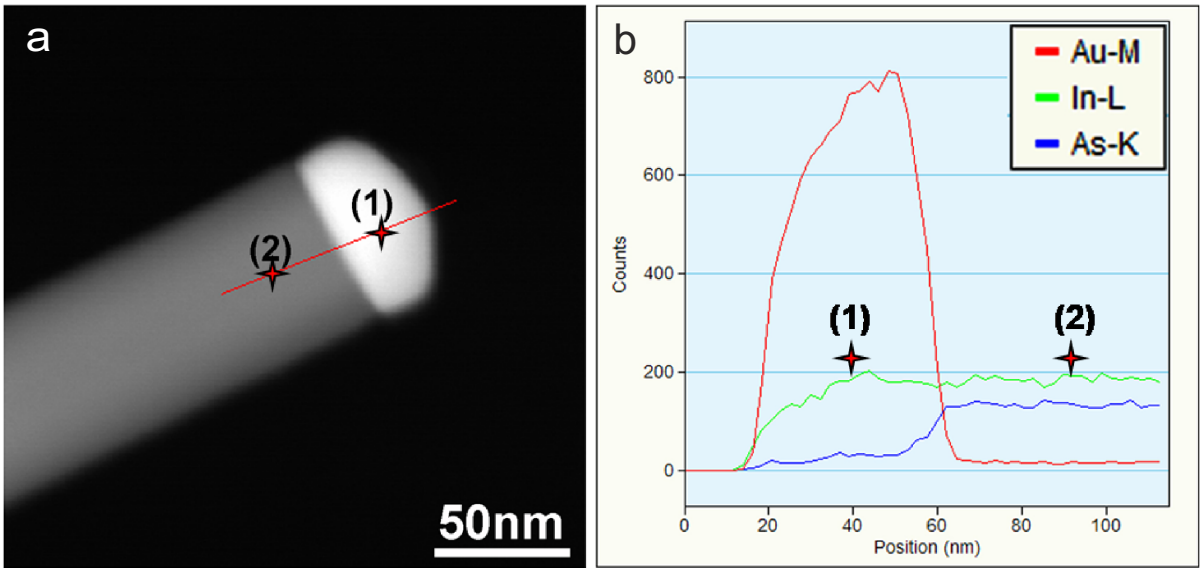

Figure 5.2.: High angular annual dark field (HAADF) image of the tip of an InAs nanowire (a). The gray contrast is proportional to the atomic number Z (bright spots correspond to high Z). Au, In and As EDX line scans taken along the red line in (a) are plotted in (b). Points (1) and (2) mark the same positions as in (a) and (b). In point (1) the quantitative analysis yields the ratio (As:In:Au) of (4.2 : 24.9 : 70.9) at.% and in point (2) the ratio of (50.5 : 49.5 : 0.0) at.%. The error is 1.0 at.%, the detection limit of EDX is around 0.3 - 1.0 at.%, depending on material.

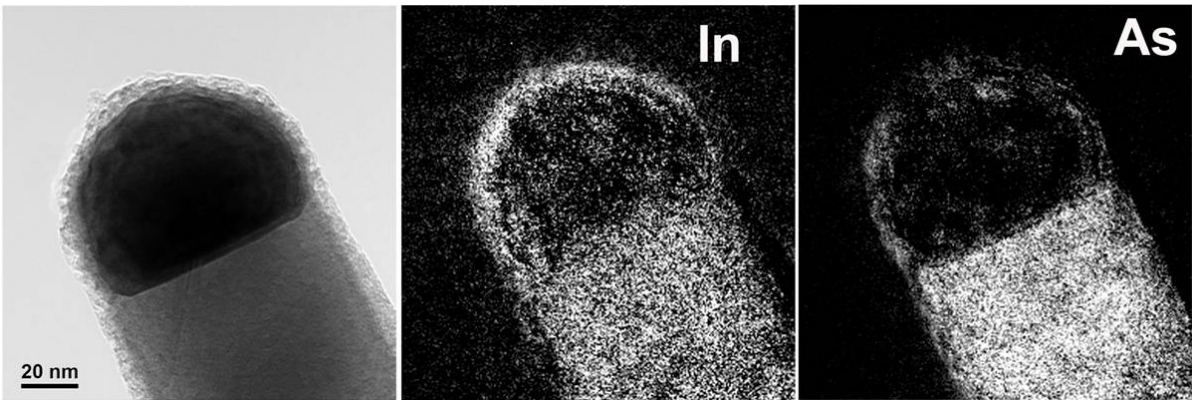

Figure 5.3.: EDX maps of In and As in an InAs nanowire. TEM bright field image (left), corresponding In map (center) and As map (right). On both maps the brightness is proportional to the EDX counts of the corresponding element. The shell around the Au nanoparticle consists of indium or indium oxide and its thickness does not exceed 0.5 nm.

of alternating twinned segments and its scheme are shown in figure 5.4 *a*. The stacking faults are not homogeneously distributed along the nanowire. In the top part the spacing between the stacking faults is about 3 atomic layers (about 0.9 per nanometer), whereas in the middle of the wires the stacking fault density varies between 0.15 and 0.35 per nm. It is important to mention that the stacking faults are visible only if the electron beam is parallel to the ⟨110⟩ zone axes (figure 5.4 *f*). If the nanowire is viewed along the ⟨112⟩ direction (figure 5.4 *e*), the electron diffraction pattern can be mistakenly indexed as an fcc symmetry (Zinc Blende structure) [86]. The angle between [110] and [112] directions is 30°. The presence of stacking faults in ⟨111⟩-oriented InAs nanowires was often reported in the literature (see ref. [80, 102] for example). Their formation is attributed to their low free energy (30±3 meV per atom [103]), compared to the thermal energy at the growth temperature (34.5 meV at 400 K). Since the nanowires grow layer by layer, one can assume that the nanowire exhibit twinning during its nucleation. During the subsequent growth the twins are extended on the whole length of the nanowire [104]. Since there is no lattice mismatch the formation of twins at the interface nanowire-substrate is not expected. This idea is supported by experimental study of crystal structure of GaAs which are similar to InAs ones, no twins were observed at the interface [105].

The ”type 3” nanowire is characterized by a mixed type of structure and stacking faults parallel to the nanowire axes. The wires have ⟨112⟩ growth direction. As it is shown on the TEM micrograph in figure 5.5 *b,d,f* a half of a nanowire normally has pure Zinc Blende structure. Another half has mixed Wurtzite and Zinc Blende structure which alternates through the stacking defects. Again, the stacking faults result in the specific stripe-like contrast on TEM images (figure 5.5 *b,f*) and the same superposition of twinned electron diffraction patterns (figure 5.5 *a*). It is important to mention that the stacking faults can be seen only when the electron beam is incident along ⟨110⟩ zone axes (figure 5.5 *f*), whereas if the electron beam is incident along ⟨111⟩ zone axes (figure 5.5 *e*) the FFT or electron diffraction can be misinterpreted as an hcp symmetry (Wurtzite structure) [86]. The angle between those two crystallographic directions is 90°. This type of twinning was previously observed in Si nanowires [104, 106].

5.1.3. Three dimensional morphology

The quantitative analysis of electron transport data as well as electromechanical resonance data requires a precise knowledge of the shape and area of the cross section of the nanowires. Moreover, information on the orientation of facets is important to understand the contribution of surface effects to the elastic and electrical properties of the nanowires. After 3D reconstruction the three dimensional data were saved as movies which are attached to the dissertation (files ”tomo-t*.avi” listed in appendix B). Figure 5.6 shows microfacets and cross sections of the three types of InAs nanowires, which were extracted by slicing the 3D reconstructions of the nanowires perpendicular to their growth directions [86]. Combining the 3D tomography data

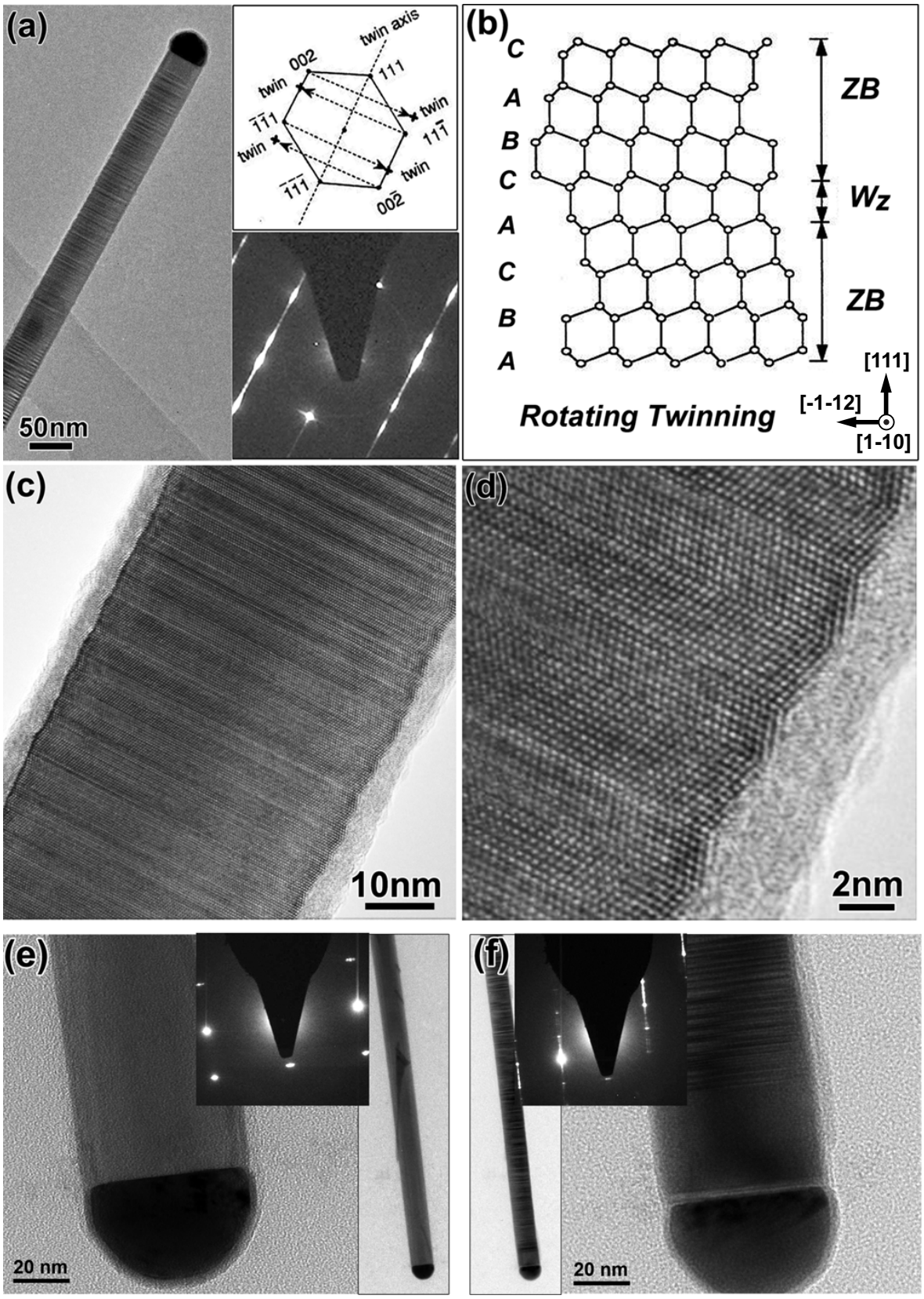

Figure 5.4.: (a) Bright field TEM micrograph of a "type 2" InAs nanowire. The insets in (a) show scheme of formation of diffraction pattern of a twin segment and corresponding diffraction pattern. (b) Schematic drawing of a twin defect. (c,d) HR-TEM micrograph of the nanowire. An amorphous oxide layer can be seen at the nanowire surface. (e,f) Bright field micrographs and corresponding diffraction patterns recorded along the [112] and [110] directions, respectively. Adopted from [86].

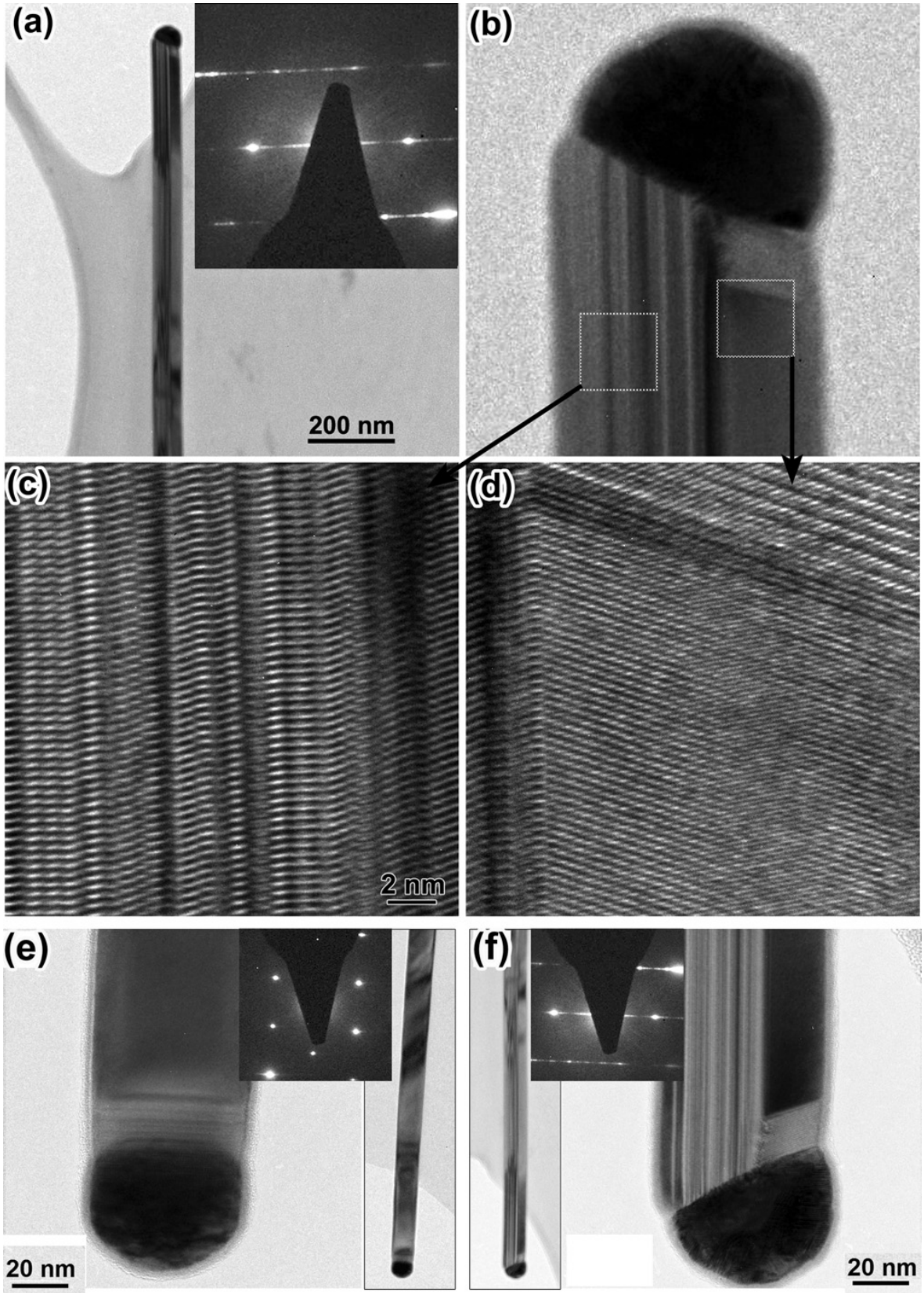

Figure 5.5.: (a) Overview bright field TEM micrograph of a ”type 3” InAs nanowire and SAED pattern in the inset. (b) Magnified top part of a nanowire, the marked regions are shown in HR-TEM micrographs (c, d). TEM images and corresponding SAED patterns recorded along the [111] zone axis (e) and the [110] zone axis (f). The figure is adopted from Li et al. [86]

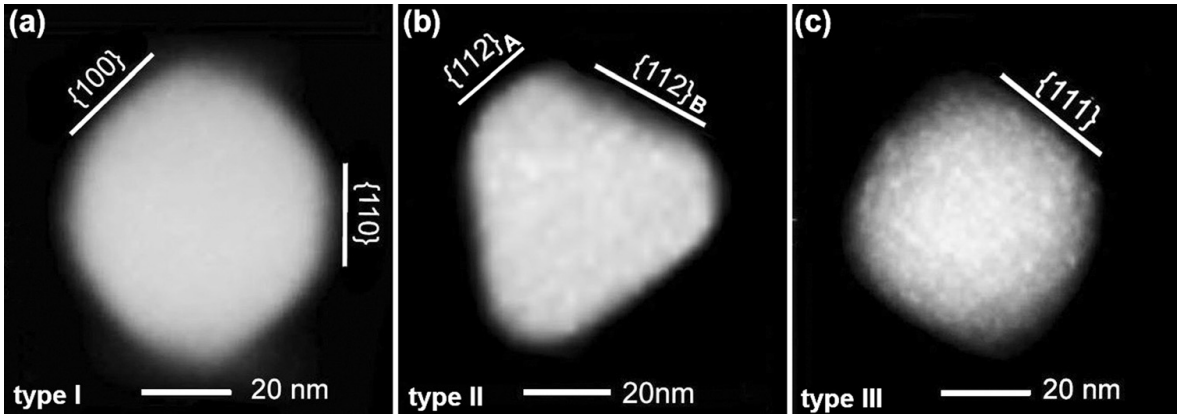

Figure 5.6.: Side walls and microfacets of three types of InAs nanowires obtained by electron tomography. (a) Type 1 with $\{100\}$ and $\{110\}$ facets. (b) Type 2 has a cross section of a truncated triangle formed by six $\{112\}$-type facets. (c) Type 3 without distinct facets. Source: [86].

with corresponding SAED data, it was found that (refer to figure 5.6): (a) "type 1" nanowires are faceted with $\{100\}$ and $\{110\}$ planes; (b) "type 2" nanowires show a cross section of a truncated triangle formed with six $\{112\}$-type facets; (c) the cross section of "type 3" nanowires is almost round and does not show clear facets [86].

5.1.4. Atomic structure of stacking faults

The presence of stacking faults in type 2 and type 3 InAs nanowires was confirmed by HR-TEM imaging and electron diffraction (see figures 5.4, 5.5). Both SAED patterns (insets in figures 5.4 *a*, *f* and 5.5 *a*, *f*) show characteristic extra spots and streaks. The first is a result of superpositions of two [110] diffraction patterns (inset in figure 5.4 *a* and 5.5 *a*) which are rotated by 70.52° against each other [84]. The streaks arise due to modification of the reflex shape by the stacking fault defects. The streaks produced by the planar defects are perpendicular to defect plains, more details can be found in [84]. The diffraction patterns like in figure 5.4 are obtained with a 10 μm selected area aperture inserted in the TEM column, which probes an area with a diameter of 200 nm. The area selected for electron diffraction contains several twins which makes quantitative analysis of the extra spots and the streaks very complicated.

According to Holt [107] twins in InAs can be of two types: "para-" or "ortho-" twins (figure 5.7 *a* and *b* respectively). The first one can be characterized by a 180° rotation of the lattice around the normal of the twin plane. Para-twins possess In-In or As-As bond formation across a twin plane and consequently have a change of crystal polarity [107]: in the lower part of the crystal (figure 5.7 *a*) the covalent bonds running from In to As pointing upwards, whereas the bonds in the upper part of the crystal pointing downwards. The second type of twin is formed by 60° rotation of the lattice against the normal of the twin plane. Ortho-twins have In-As-In bonds across the twin plane, and crystal polarity does not change.

The formation of ortho- and para-twins was not studied for InAs. Because of the requirement to form As-As or In-In bonds, para-twin formation energy is higher than the ortho-twin one. However, para-twins have been observed in BeO [108] or GaP [109], for example. The formation of para-twins in III-V semiconductor nanowires, in particular in InAs nanowires, depends on the competition of the total surface energy and para- or ortho-twin formation energies. Depending on the twin type different crystallographic facets will form which in turn have different surface energies (see for an example ref. [110]). However, to consider only the minimum of the free energy is not sufficient since during the growth of the nanowires kinetics plays important role. Among the studies of twin defects in similar systems the work of Tillmann coworkers [111] should be outlined. They studied twin defects in $In_{0.3}Ga_{0.7}As$/GaAs heterojunctions and in Cr implanted GaN thin films [111]. No para-twins were found in both samples. They observe that the ortho-twins in GaAs are distorted, i.e. the length of the Ga-As dumbbell changes by up to 10% and they are misoriented by up to 5° [111].

To identify the type of twin defects in the InAs nanowires scanning transmission electron microscopy (STEM) was performed utilizing high-angle annular dark-field detection (HAADF) (see section 4.2.4). This method delivers Z-contrast images in which heavier elements appear brighter. Figures 5.8 *a* and *b* show low and high magnification HAADF images of an InAs nanowire. The part of figure 5.8 *b*, which is marked by the red square, was filtered using a Wiener filter [112] which parameters are listed in the figure caption. Figure 5.8 *c* shows the filtered image. Comparing figures 5.8 *b* and *c* one can conclude that the filtering does not produce any artifacts in the central region of the nanowire. The area marked with the red square in figure 5.8 *c* is plotted as surface 3D plot in figure 5.8 *d*. The plane view of the surface plot is shown in the inset *(e)* in figure 5.8 *a*. The spots, correspond to the atomic columns, have double peak structure (see figures 5.8 *b-e*), which can be attributed to the In-As dumbbell. The highest peaks correspond to In atoms and satellite (smaller) peaks indicate the columns of As atoms. Comparing figures 5.7 and 5.8 *b-e*) one can conclude that the twin defects are ortho-type. No para-twins were found in the InAs nanowires. These findings are consistent with other preliminary investigations of twin defects in III-V semiconductor nanowires [110, 113]. Since the difference between ortho- and para-twin formation energies is low, the absence of para-twins indicates that the top facet of the nanowire always remains {111}B-type during the growth. The same top facet type was identified in MOCVD-grown GaP nanowires [114].

5.2. Hardening of InAs nanowires with high stacking fault densities

In this section the study of elastic properties of the nanowires is presented. First, common features in elastic response to electromechanical excitation of both ”type 2” and ”type 3”

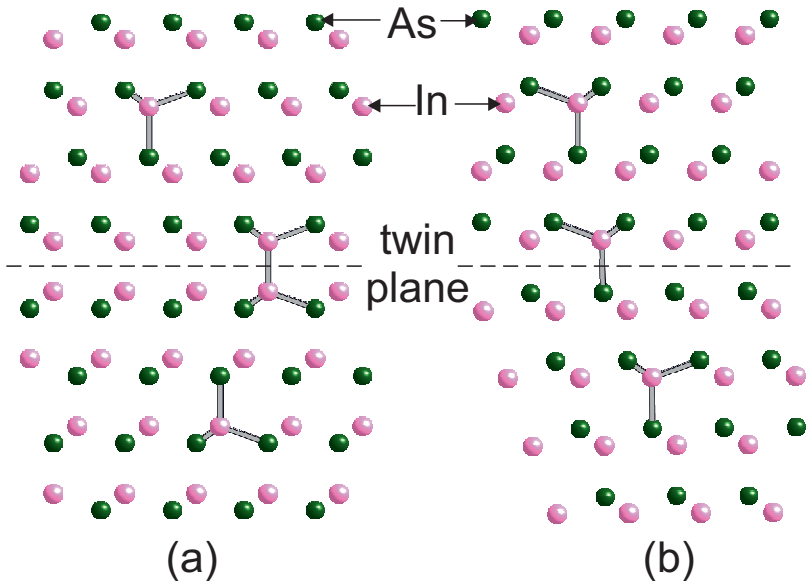

Figure 5.7.: Ball-stick model of para- (a) and ortho- (b) twins in InAs. The sticks show examples of atomic bonds. Formation of In-In bonds (a) as well as change of crystal polarization is a characteristic property of para-twins.

nanowires will be discussed. The results of the study of elastic properties of the "type 2" and the "type 3" nanowires will be discussed separately. In the end the conclusions about phenomenas affecting the elastic properties of the nanowires of both types will be drawn.

Elastic properties of InAs nanowires were determined using electromechanical resonance (see section 4.3.1) and the analysis of the bending behavior (see section 4.3.2). In the measurements of the electromechanical resonance two vibrational modes of the nanowires were observed at the frequencies f_0 and $2f_0$. The amplitude of the higher frequency mode ($2f_0$) linearly depends on the amplitude of the exciting voltage. The resonance mode with the higher excitation frequency is the fundamental mode in this case (see section 2.2). Typical TEM images of a type 2 InAs nanowire (nanowires with stacking faults perpendicular to the growth direction; see section 5.1.2) at different vibration frequencies and the corresponding amplitude-frequency dependence (resonance curve) are shown in figures 5.9 and 5.10 *b*. The resonance curve was fitted with a Lorentz function (red line in figure 5.10 *b*) to determine the quality factor Q of the resonance. Q = 1870±150 is typical for the InAs nanowires of both types with diameters between 30 and 120 nm and length of 3 - 10 μm. A relatively high (among nanowires, see appendix A) quality factor confirms a very low damping in the system. Such quality factors, however, are not exceptionally high among nano electromechanical resonators in which it can be up to $Q \sim 3.9 \times 10^5$ for strained SiN double-end clamped bar with dimensions of 75 μm x 500 nm x 105 nm [115]. The inset in figure 5.10 *a* shows an intensity profile along the black arrow in the bright field TEM image (figure 5.10 *a*) of the nanowire in resonance. The distance between the minima of intensity represents the amplitude of the vibration. Comparing the shape of the intensity profile with the simulated one for harmonic oscillations (figure 5.11) and taking

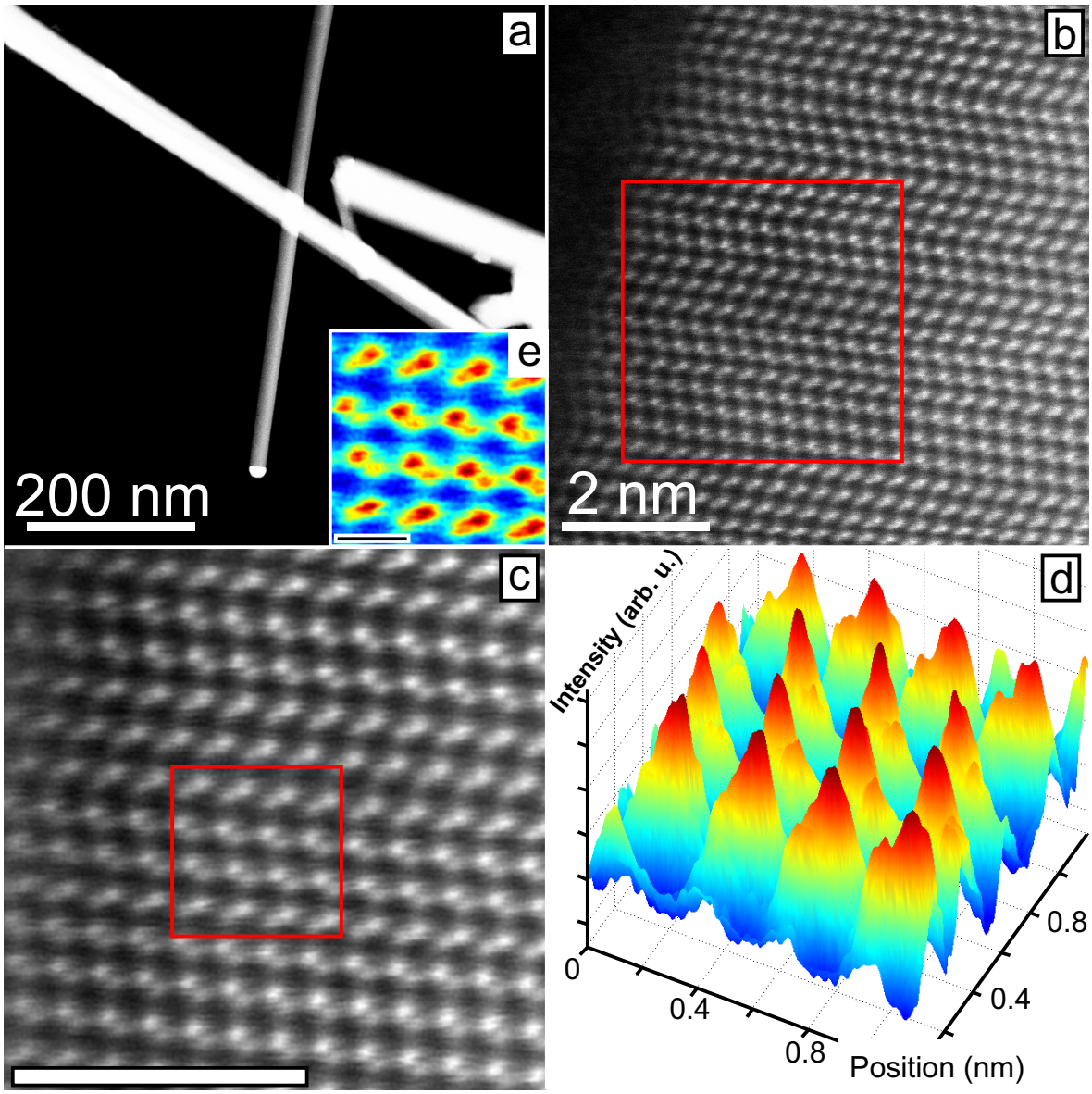

Figure 5.8.: (a) STEM-HAADF low magnification micrograph of an InAs nanowire. (b) High resolution STEM-HAADF micrograph. (c) Magnified part, as indicated by the red box in micrograph (b), filtered using Wiener filter [112], setting the upper limit of the pixels to be changed to 0.5 %, amount of filtering cycles to 10 and order of Butterworth filter to 5. (d) Linear 3D color plot of the area within red square in (c). (e) Colored inset of (a) is a 2D view of the plot (d). Scale bars in (c) and (e) are 2 nm and 0.4 nm respectively.

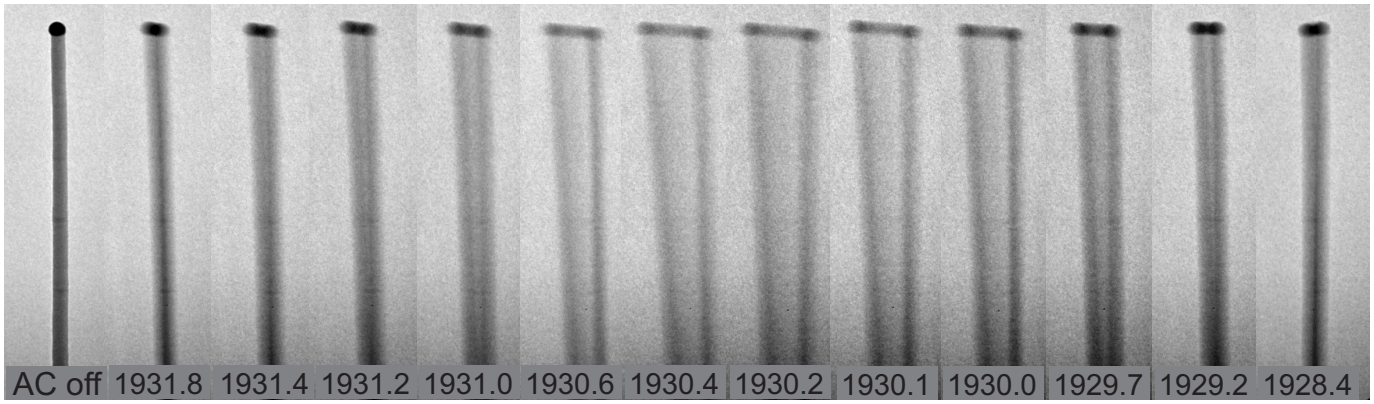

Figure 5.9.: TEM image series of electromechanical vibrations of an InAs nanowire excited by different frequencies as indicated at the bottom (in KHz).

into account that the resonance curve can be fitted with a Lorentz function, we can conclude:

- InAs nanowires (with diameters $D = 30 \div 120$ nm, length $L = 3 \div 10$ μm) respond harmonically to harmonic excitations;
- damping of the nanowire vibrations is very small ($Q > 1000$);
- the measured resonance frequency is the fundamental frequency.

These findings allow us to implement the theory for mechanical vibration as described in section 2.2.

The fundamental resonance frequencies f_1 were measured for the nanowires of type 2 and type 3 with diameters between 30 and 120 nm. Young's moduli along $\langle 111 \rangle$ directions for type 2 nanowires and along $\langle 112 \rangle$ directions for type 3 were calculated according to equation 2.30. In addition to the determination of Young's modulus by electromechanical resonance, the Young's modulus of two nanowires of type 3 was also extracted by analysis of bending of the nanowires with an AFM tip (section 4.3.2 and appendix E).

5.2.1. Young's modulus of "type 2" InAs nanowires

Young's modulus (around room temperature under low electron irradiation with low flux[1]) of "type 2" InAs nanowires which have $\langle 111 \rangle$ growth direction and stacking faults perpendicular to the growth direction is plotted in figure 5.12 *a* against the diameter D. Around $D = 65$ nm a maximum is found, where Young's modulus $E \approx 220$ GPa exceeds bulk value (solid red line in figure 5.12 *a*) more than by the factor of 2. For the thick nanowires (around $D = 120$ nm) Young's modulus approaches bulk value $E_{bulk} = 97$ GPa. The data points strongly scatter around

[1] less than 500 $\bar{e}$/nm^2

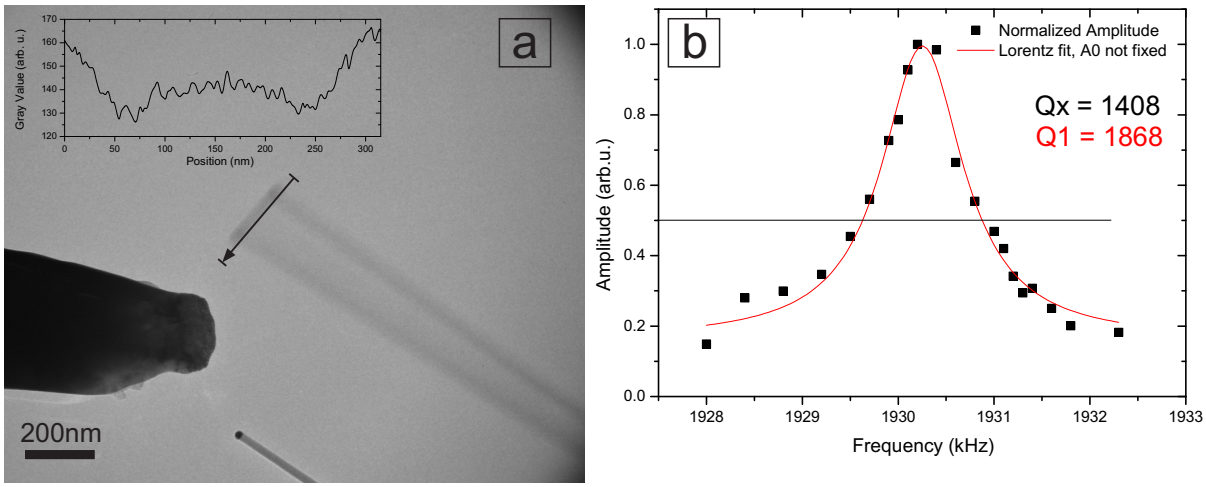

Figure 5.10.: (a) TEM image of a vibrating InAs nanowire. Between the STM tip on the left and the nanowire an alternating voltage (U_{AC} = 350mV) is applied. The inset shows the intensity profile along the black arrow. (b) Normalized amplitude versus frequency. Experimental data (black squares) are fitted with a Lorentz function (red line). $Q1$ is the quality factor calculated from the Lorentz fit is $Q1$ and $Qx = \Delta f / f_{res}$ is the quality factor estimated from direct measurements of line width Δf and resonance frequency f_{res}.

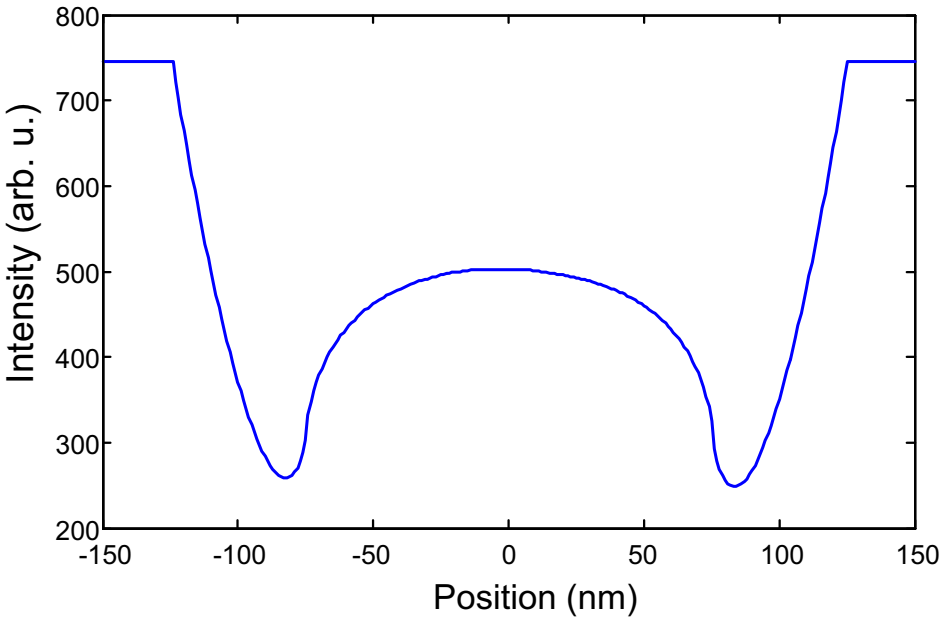

Figure 5.11.: Simulated bright field intensity profile across vibrating nanowire. The vibration frequency was set to 1.5 MHz, A = 160 nm, length L = 5 μm, diameter D = 30 nm, Young's modulus E = 100 GPa, acquisition time t_0 = 0.01 s.

D = 50 nm, although their crystal structure is identical. This indicates that the morphology and stacking fault density of the nanowires are different. The stacking fault density for some[2] of the nanowires could be estimated from TEM images. The stacking fault density is shown with blue circles in figure 5.12 (use right y-axes to interpret the data). It decreases from a maximum value around D = 65 nm by more than a factor of two at $D \approx 120$ nm. This can be correlated with Young's modulus: the higher is the stacking fault density the stiffer is the nanowire.

The drastic enhancement of Young's modulus of the nanowires of up to 200 % around D = 65 nm compared to bulk can be due to:

- **Surface** effects: in particular surface relaxation or surface stress;
- Distortion of the crystal lattice in the **stacking fault** region;
- Redistribution of electron densities either at the surface or inside the nanowire.

The question if the **surface** is softer or stiffer than the bulk was discussed in section 2.3. While there is no general answer to this question, there are some factors which may result either in a softening or stiffening of the surface. According to the bond-orientation-bond-length-bond-strength (bond-OLS) model [29] surface relaxation is an important factor affecting elasticity. Negative normal relaxation (contraction of bonds perpendicular to the $\langle 111 \rangle$ direction) should result in stronger bonds at the surface and consequently stiffening. In the case of InAs nanowires with the $\langle 111 \rangle$ growth direction the surface of the nanowire is decorated with the $\{112\}$ type macrofacets, which, however, can be formed by the continuous $\{112\}$ surface or by the $\{111\}_A$ and $\{111\}_B$ surfaces alternating with twin defects (see appendix F). The last one should be allowed only in multitwin nanowires with the stacking fault (SF) density about 0.1 - 1 SF per nm. A free energy of the $\{111\}$ surface is lower than that of the $\{112\}$ surface, which was found to be unstable [116]. Schemes and arguments presented in the appendix F, bring us to a conclusion that the nanowires most probably decorated with the $\{111\}$ surfaces, whose relaxation in a normal direction does not lead to a significant change of the elastic properties. In the case of the $\{112\}$ surfaces, we believe that the relaxation is small and can take place mostly in the normal direction due to low symmetry and short interplane distances of the $\{112\}$ planes. In both cases softening or stiffening of the surface due to surface relaxation can be neglected.

The other important aspect affecting the stiffness of the InAs nanowires is the **presence of stacking faults**. The stacking faults are ortho-type, thus, there are no In-In or As-As bonds across the defect plane (see section 5.1.4). There is no change of the orientation of the nearest neighbors in the nanowire segment containing a stacking fault compared to the original Zinc

[2] A possibility to see stacking faults in a bright field TEM image depends on the nanowire crystallographic orientation (see section 5.1.4). Since the orientation of the nanowires was not controlled during sample preparation for the in-situ measurements (section 4.3.1), only for about 20 % of the nanowires the stacking fault density could be estimated.

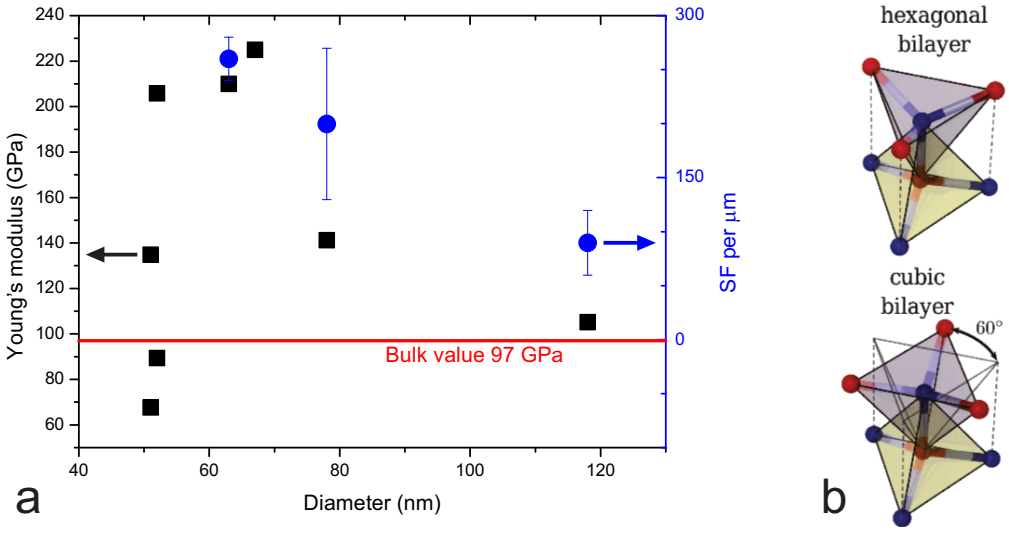

Figure 5.12.: (a) Dependence of Young's modulus of "type 2" InAs nanowires on diameter (black squares). The value for bulk InAs in ⟨111⟩ direction is marked with the red line. Blue circles show the density of stacking faults (right y-axis). (b) Schematic atomic model of hexagonal (Wurtzite) and cubic (Zinc Blende) bilayers: In atoms (red balls) of the top layer are located above As atoms (blue balls) for the hexagonal structure. The top In layer is rotated by 60° in the cubic structure (adopted from [102]).

Blende. The layer of second nearest neighbors, however, is rotated by 60 ° with respect to the original structure. For instance, figure 5.12 *b* shows an AB^3 bilayer of original cubic structure and an AB bilayer of a region with stacking fault (hexagonal structure). Obviously the distance between the second nearest neighbors is increased in the cubic structure, if one assumes the same interplane distance for both structures. According to density functional theory calculations performed by Kriegner and coworkers [102], the rotation of the layer of the second nearest neighbors increases the lattice parameter of the hexagonal structure with respect to the cubic segment by approximately 0.2 %. The increase in lattice parameter leads to weaker bonds within the region containing a stacking fault, that is a smaller Young's modulus in this region. This effect can be estimated applying the "bond-OLS" model proposed by C. Q. Sun and coworkers [29]. The bond energy change can be expressed as following [29]:

$$\frac{\Delta E_B(d)}{E_B(d_0)} = \frac{E_B(d)}{E_B(d_0)} - 1 = c^{-m} - 1, \tag{5.1}$$

where $d = d_0 + \Delta d$, $c = \Delta d/d_0 + 1$, d_0 is an original lattice parameter and Δd is an absolute change of the parameter, m is a parameter which defines bond-length dependence of the change of binding energy [29]. The study shows that $m \approx 4$ is a good approximation for compounds (including InAs) [29]. The consequent relative change of Young's modulus can be calculated

[3]Please refer to figure 5.7. Blue letters represent hexagonal bilayer, red letters represent cubic bilayer. For the closed packed structure layers sequence (AB) and (ABC) represent hcp and fcc structures respectively.

using the following equation [29]:

$$\frac{\Delta E}{E} = c^{-m} - 3c + 2 \tag{5.2}$$

According to the DFT simulations and experimental results obtained by Kriegner and coworkers the total bond expansion in the region containing a stacking fault in InAs along the ⟨111⟩ direction is around 0.2 % [102]. Inserting c = 1.002 and m = 4 in equation 5.2, I calculated a decrease of Young's modulus by 1.4 %. This result indicates that the distortion of the crystal lattice can not explain the trends observed experimentally (figure 5.12 *a*).

According to Zhou and coworkers [30], also the distribution of electron charge in the sample affects Young's modulus. The InAs surface possesses an electron accumulation layer (see section 3.1), resulting in a stronger bonding and a stiffer elastic response at the surface. Since the redistribution of electron density happens only in the first few atomic layers, thinner wires, due to their higher surface-to-volume ratio, are expected to be stiffer than thicker ones. The charge density redistribution may also occur due to stacking faults. A scanning probe microscopy experiment [18] shows Coulomb blockades in the nanowires at low temperature. The authors attribute the observed effect to the stacking fault defects. It provides an evidence that stacking faults result in the charge density redistribution along the nanowire. While the other previously discussed phenomena which affect elastic properties of the nanowires are not related with stacking faults or have a very small impact (like lattice relaxation in the stacked region), we conclude that the charge redistribution results in the experimentally observed hardening of the nanowires with high densities of stacking faults. The electronic properties of the nanowires will be discussed in the next chapter.

5.2.2. Young's modulus of "type 3" InAs nanowires

Figure 5.13 shows the dependence of Young's modulus of the type 3 nanowires (with ⟨112⟩ growth direction) on their diameter. The black squares and blue circles show the data obtained by using the electromechanical resonance technique and by the analysis of bending of the nanowires, respectively (see section 4.3.2 and appendix E). The Young's modulus of thin nanowires ($D \approx$ 35nm) is slightly increased (by less than 50 %) compared to the bulk value for ⟨112⟩ direction. Around D = 52 nm a maxima is found where the Young's modulus increased by about 300 % compared to bulk value. For the thicker nanowires with D ~ 90 nm Young's modulus aproaches bulk value. The graph shows that Young's modulus increases with the increase of diameter for the nanowires with diameters up to 52 nm and decreases again for the thicker nanowires. Comparing the experimental data with the data for the ⟨111⟩-oriented nanowires, the same enhancement of Young's modulus is found. However, Young's modulus for the thinner nanowires (< 52 nm) does not show a sign of surface effects. This trend can be

compared with the elastic properties of the tungsten oxide nanowires investigated by Liu and coworkers [36]. In that case the Young's modulus increases up to bulk value with the decrease of the nanowire diameter (shown with magenta dashed line in the figure 5.13). This behavior should be related to the stacking faults. It is difficult to determine the stacking fault density for the ⟨112⟩-oriented nanowires, since they can be imaged only in specific directions (refer to section 5.1.2).

The main reasons for the significant enhancement of the Young's modulus in the ⟨112⟩-oriented nanowires can be:

1. **lattice relaxation** due to the stacking faults;

2. **redistribution of electron densities** at the surface of the nanowires.

(2) Was already discussed above. The surface effects could explain the trend seen in figure 5.13 for the nanowires thicker than 52 nm (blue circles). Young's modulus is higher for thinner nanowires due to stronger bonding within surface atomic layers induced by the electron density redistribution at the surface. The main reason for the drastic enhancement of the Young's modulus around 52 nm is a lattice distortion due to stacking faults. The lattice constant of a Zinc Blende segment does not match the lattice constant of the stacked segment. The area of the interface between Zinc Blende and Wurtzite region in this nanowires is much bigger than in case of the ⟨111⟩-grown wires. This will result in higher internal stress at the interface regions which may result in anisotropic relaxation of the lattice, which signs can be seen in the diffraction pattern (figure 5.14 *a*) taken for ⟨111⟩ zone axes for a "type 3" InAs nanowire.[4] At the diffraction pattern (figure 5.14 *a*) distance between the reflexes of $\frac{1}{3}$(2-42) type ($1/d_1$ = (2.669±0.016) 1/nm) is smaller than the distance between the reflexes of $\frac{1}{3}$(-2-24) and $\frac{1}{3}$(-422) types ($1/d_2$ = (2.950±0.010) 1/nm). This findings give a hint that the original lattice (ideal interplane distance $d_{1/3(422)} \approx 3.708$ Å) is compressed in the [-1-12] and [-211] directions by approximately 9% and expanded in the [1-21] direction by approximately 1%. Moreover, the anisotropic relaxation can result in a complicated deformation behavior (combination of stretching/compression, shear and twisting) of the nanowires in both experiments.

To analyze the deformation behavior during the experiments the selected area electron diffraction was performed during the bending of a nanowire (the procedure is described in section 4.3.2). Figure 5.14 shows diffraction patterns for an InAs nanowire under different mechanical loads. It is interesting that after the loading force overcomes a value of about 170 nN, a well pronounced concentric stretching of the diffraction reflexes takes place (figure 5.14 c). This stretching (broadening) of the reflexes is due to bending of the nanowire: lattice planes with the same indices change their relative orientation depending on the position in the wire.

[4] Type 3 InAs nanowires have ⟨112⟩ growth direction and stacking faults parallel to the growth direction. In this case viewing along [111] zone axes means viewing normal to the stacking faults plains.

The position of the diffraction reflexes from each plane will be different and the superposition of the reflexes gives characteristic arcs in the diffraction pattern. HR-TEM images and related diffraction patterns were simulated assuming a nanowire segment with size of approximately 90x30x60 nm^3, which bending curvature has radius R equal to 500 nm (see appendix D for more details). Figure D.5 (in appendix D) shows a simulated HR-TEM micrograph and the corresponding diffractograms for a non-deformed wire (*a-c*) and for a bended wire (*d-f*). One sees that, the homogeneous bending results in a homogeneous concentric broadening of diffraction reflexes (figure D.5 *b-c*).[5] The experimental diffraction pattern of the bended nanowire (figure 5.14 *c*), however, is not identical with the simulated one (figure D.5 *e*). To be able to compare experimental and simulated diffraction patterns the reflexes of the experimental patterns (from figure 5.14) were magnified and plotted in color in figures 5.15 and 5.16. The following features do not appear in the simulated diffractograms (figures D.5-D.8):

- the variation of the intensity of the symmetric reflexes. For example, for the non-deformed nanowire (figure 5.15) maximum of intensity of the $\frac{1}{3}$(-2-24) reflex is equal to 180 arb. u., whereas the intensity maximum of the $\frac{1}{3}$(22-4) reflex is 18 arb. u.;
- the broadening of $\frac{1}{3}$(2-42) and $\frac{1}{3}$(-24-2) reflexes (see figures 5.14 *c* and 5.16) is smaller than broadening of $\frac{1}{3}$(-422), $\frac{1}{3}$(-2-24) and $\frac{1}{3}$(22-4)[6] We will call this feature "anisotropic broadening" of diffraction reflexes;
- the reflexes of $\frac{1}{3}$(-422), $\frac{1}{3}$(-2-24) and $\frac{1}{3}$(22-4) planes are split (see figures 5.16);
- the change of the radial position of the intensity maxima of $\frac{1}{3}$(-422), $\frac{1}{3}$(-2-24) and $\frac{1}{3}$(22-4) reflexes under the load (decrease of the corresponding lattice spacings).

The first feature is only due to not perfect imaging conditions - the electron beam was not exactly parallel to the zone axes. The imaging conditions, however, can not affect position and shape of the reflexes. The anisotropic reflex broadening shows anisotropy in the elastic properties (i.e. the elastic constants for crystallographically equal directions [11-2] and [1-21] will not be equal). The reason for the anisotropy of the elastic properties is the anisotropic lattice relaxation which is caused by the stacking fault defects which are parallel to the growth direction.

The split of the reflexes shows that the wire deformation is inhomogeneous: during the deformation one group of lattice planes is inclined with an angle of about 2° to another group of the lattice planes, which is, however, has the same Miller indices as the first one. Since the two parts of the reflex are clearly separated, the transition from one group to the other must be rapid, resulting in a high local strain. Or the reflex splitting can be the result of a complex

[5] One should note that the described mechanism is valid only for the deformation of an isotropic body, however it can also be partly applied to the InAs nanowires with ⟨112⟩ growth direction.

[6] note that the corresponding interplane distances were found to be decreased comparing to ideal InAs as described previously.

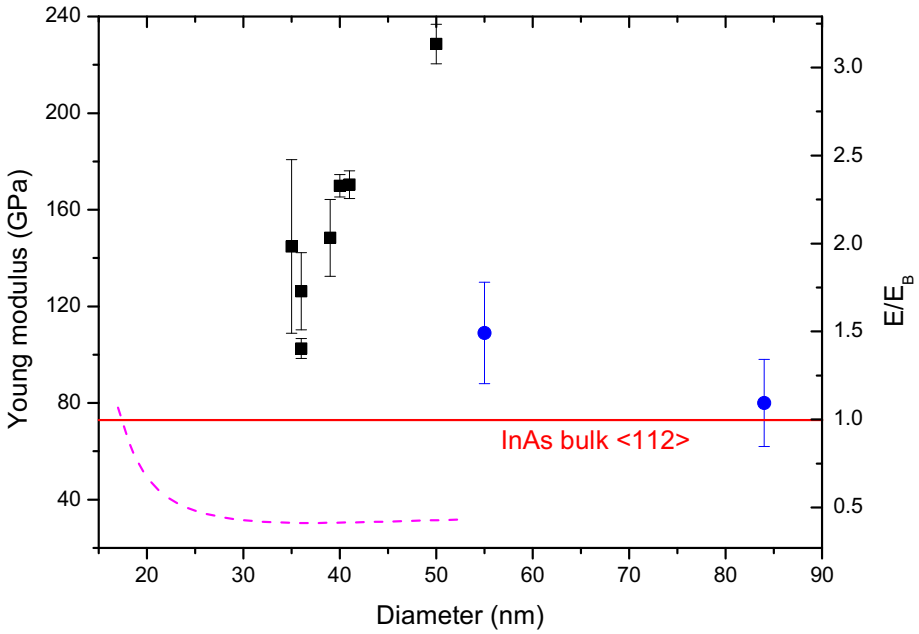

Figure 5.13.: Dependence of Young's modulus of the type 3 InAs nanowires (with $\langle 112 \rangle$ growth direction) on their diameter. Black squares show data points measured with electromechanical resonance and blue circles show data measured analyzing bending data. A bulk value of Young's modulus calculated for the $\langle 112 \rangle$ direction is shown with the red line. The dashed magenta line shows the dependence of Young's modulus of tungsten oxide nanowires [36] with the same type of stacking fault defects on their diameter. Experimental data can be interpreted using both left and right axes. The reference data for tungsten oxide should be interpreted using the right axis which shows Young's modulus normalized to bulk value E/E_b.

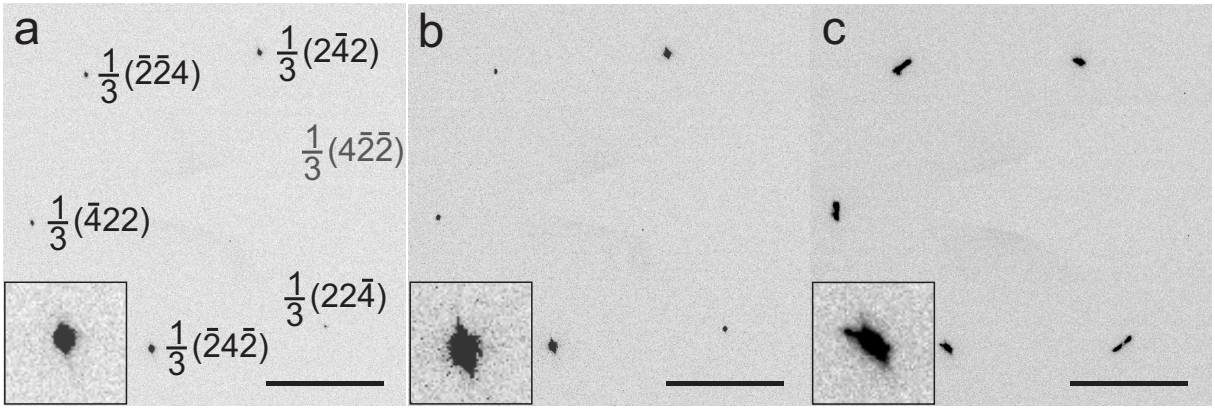

Figure 5.14.: (a) Electron diffraction pattern of an InAs nanowire without any mechanical load, (b) loaded with an AFM tip with a force F = 79nN and (c) F = 225nN. The length of the scale bars in all images is 2 1/nm. The insets in each image show a magnified lower left diffraction reflex from the corresponding pattern.

deformation (twist and shear) and the existence of two distinct areas in the sample that are differently deformed.

In contrast to ideal bending the deformed nanowire shows a contraction of the interplane distances as indicated by the larger reflex separation. The decrease of the interplane distance d for distorted (11-2) and (-211) planes reaches 3%, whereas for the non-distorted (1-21) planes the interplane distance remains the same within the error bar of ±0.5 %. This again confirms that the nanowire is deformed in a complex way. Since the diffraction pattern delivers only two dimensional information, the deformation of the nanowire can not be fully analyzed. To obtain a better understanding the finite element analysis (FEA) was used to model the deformations of a nanowire under a bending force. The calculation allows to estimate the stress and strain in the nanowire as a function of the bending. Based on these structural calculations a diffraction pattern can be simulated and compared with the experimental one. Both simulations can be repeated iterativelly to acheive the best fit to experimental data.

The FEA simulations were performed using "Comsol Multiphysics®" software [117]. The nanowire was approximated as a solid cylinder with a diameter of 80 nm and a length of approximately 1.5 μm (both parameters are the same as the experimental parameters of the nanowire). The bottom end of the cylinder was fixed. A force of 285 nN was applied to the upper (-1-12) surface of the nanowire at an angle of 15° with respect to the cylinder axis. The elastic constants of bulk InAs at room temperature (c_{11} = 83.4 GPa, c_{12} = 45.4 GPa, c_{44} = 39.5 GPa) [118] were used for the simulations. An average size of the mesh element is 12 nm^3. Figure 5.17 shows the simulated shape of the deformed nanowire and distribution of the strain energy in color code. One sees that the bottom part of the wire is strongly deformed and highest strain energies are present at the surface. The strain energy decreases towards central axis of the nanowire and its top. The strain energy is homogeneous in the whole volume and no twisting deformation can

be seen. Since the stacking faults were not included in the model, we conclude that the defects result in the inhomogeneous deformation, which was seen in the experimental data. The improvement of the model required more detailed knowledge of the lattice distortions induced by the stacking faults in the ”type 3” nanowires and more experimental data on the bending of the nanowires.

The observed inhomogeneous deformations do not allow to implement the simple model discussed in section 2.1 an in appendix E to extract the elastic moduli by analyzing bending of the nanowires. Consequently, the blue points in figure 5.13 may only represent efficient Young's modulus which is an analogue to spring constant of the system with a given geometry. The better understanding of mechanical properties of the ⟨112⟩-oriented nanowires and extraction of quantitative information require more experimental data and improvement of the model for FEA simulations.

In summary, elastic properties of InAs nanowires strongly depend on their growth direction and consequently on the orientation of the stacking fault defects. It was shown that the higher is the stacking fault density in the ”type 2” nanowires, the higher is Young's modulus (figure 5.12). This phenomenon was attributed to redistribution of electron densities in the nanowires, which is induced by the stacking faults. This redistribution leads to stronger bonding in the regions containing the defects. In the ”type 3” nanowires the stacking fault lead to strong distortions of the crystal lattice (which is not a case in the ”type 2” nanowires). These distortions result in inhomogeneous strains during bending deformations and significant change of elastic properties of the nanowires (figure 5.13).

5.3. Electron transport in InAs nanowires

5.3.1. Correlation of electron transport with atomic structure in InAs nanowires

The electron transport in InAs nanowires was studied by a two point contact I-V measurement in-situ in TEM as described in section 4.3.3. Figure 5.18 a shows a typical I-V curve for the InAs nanowires. The measurement starts at -500 mV (blue curve). The red curve shows the reversed direction (from +500 mV to -500 mV). There is no hysteresis in the curve, thus, there is no charging of the system (nanowire and two contacts) during the measurement. The I-V curve is not linear. For about 50% of the nanowires the non-linearity is more pronounced. The I-V curves, however, are symmetric, and the contacts at the top and at the bottom of a nanowire are different. Thus, there is no Schottky barier and the reason for the non-linearity is different. There are two possible effects which can lead to the non-lineariry of the I-V curves:

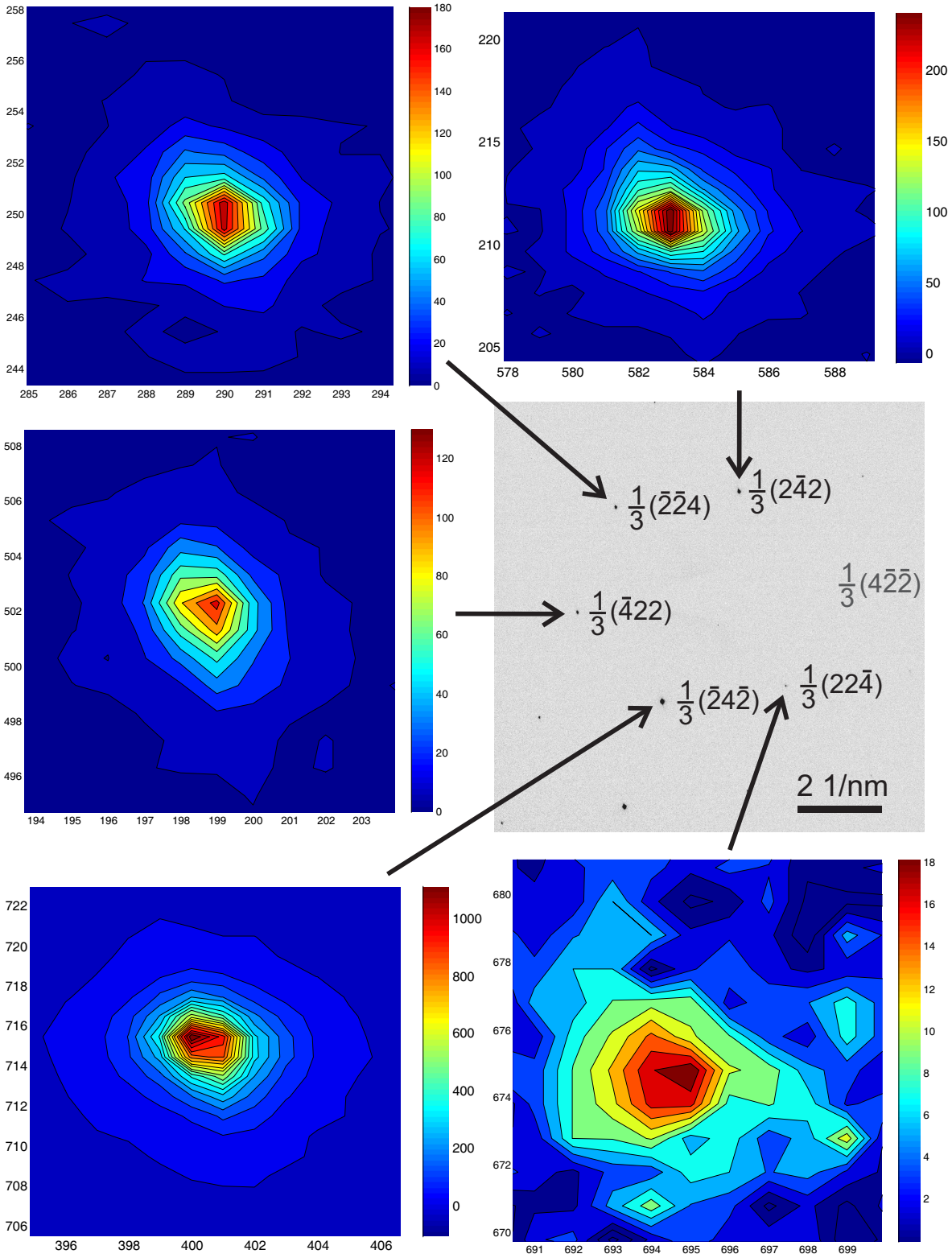

Figure 5.15.: Electron diffraction of a non-deformed InAs nanowire (gray scale image in the center). The magnified reflexes are shown as colored contour plots as indicated by the arrows. The scales of x- and y-axis are have units of pixels (the origin of the axis is at the top left corner). The color code shows the absolute intensity of the original diffractogram in arbitrary units.

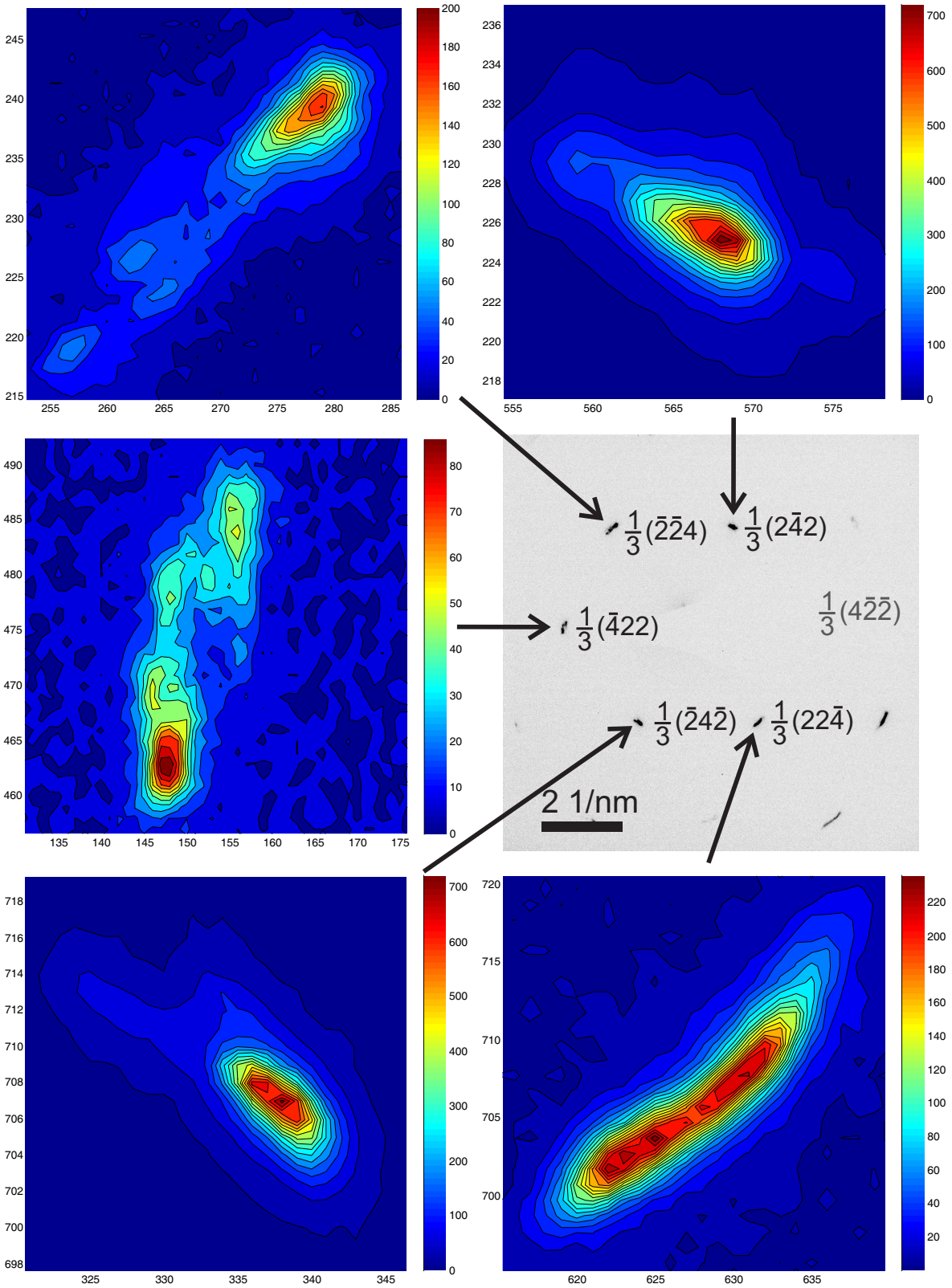

Figure 5.16.: Electron diffraction of a InAs nanowire to which a force of 225 nN is applied (gray scale image in the center). The magnified reflexes are shown as colored contour plots as indicated by the arrows. The scales of x- and y-axis have units of pixels (the origin of the axis is at the top left corner). The color code shows the absolute intensity of the original diffractogram in arbitrary units.

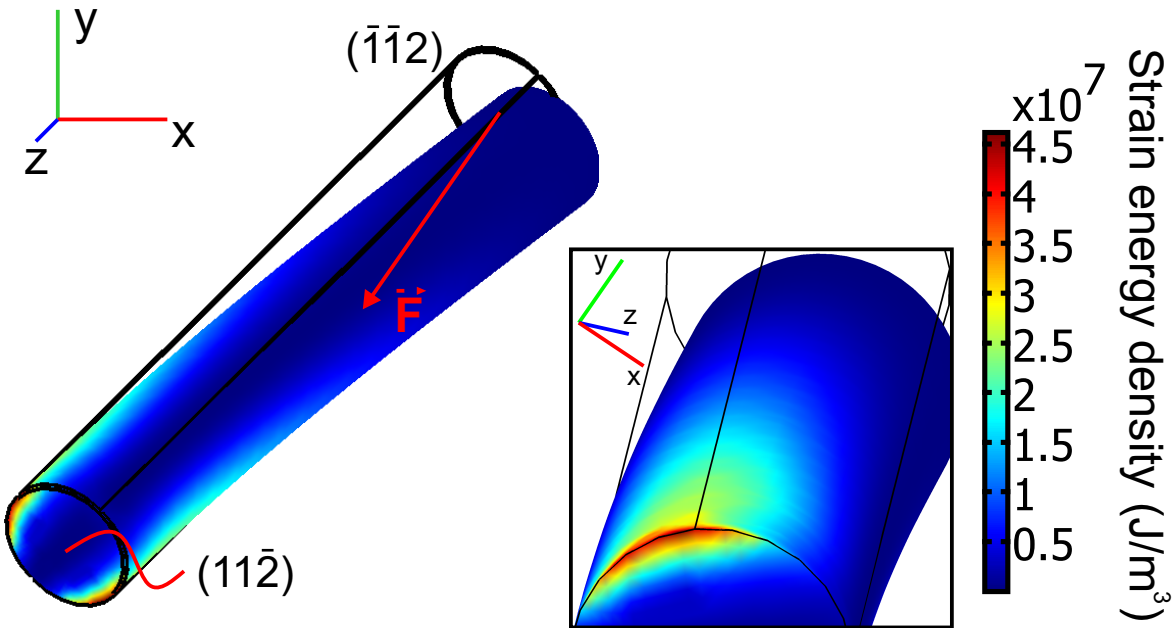

Figure 5.17.: The simulated shape and strain energy density of a deformed InAs nanowire. The axes X, Y and Z are set along ⟨001⟩ directions. The nanowire axis is parallel to ⟨112⟩ direction. The nanowire is bended by a force $\vec{F}$ applied to the top (-1-12) surface. The force vector lies in (111) plane and has an angel of 15° with the nanowire axis. The bottom (11-2) surface of the nanowire is fixed. The initial shape of the wire is shown with black contour line. Inset shows magnified part of the nanowire, in which the highest strain energy is concentrated.

space charge limited current (SCLC) and Joule heating of the nanowire. The first effect ocures when the electrons are injected from the STM tip into the nanowire due to the electron concentration in the tip is much higher. The current injection will result in space charges near interface which contribution to total current will be higher with an increase of the voltage. Using the electrodynamic solution proposed by Talin et al. [119], the current density j is given by:

$$j = \zeta_0 \frac{\epsilon \mu}{RL} V^2, \text{ for } \frac{R}{L} << 1, \tag{5.3}$$

where ζ_0 is a numeric constant, ϵ is a dielectric constant of InAs, μ is an electron mobility, R, and L are radius and diameter of the nanowire. The crossover voltage V_c at which SCLC equals to Ohmic current can be written as [119]:

$$V_c = \frac{eR^2}{\epsilon} n_{eff}, \tag{5.4}$$

where e is charge of an electron, and n_{eff} is an effective electron concentration in the nanowire. At the crossover voltage transition from Ohmic to SCL current occurs. To apply this theory, the I-V curves were first plotted as a log-log plot, where the crossover voltage V_c can be easily found as a paint in which the slope of the curve changes. The region above V_c of the original I-V curve can be than fitted with a parabolic function according to equation 5.3 (see figure 5.19 *a*). One sees that the red curve in figure 5.19 fits good to the experimental data, but the low voltage part of the I-V curve (bellow V_c) is, however, not linear, which will be discussed later. The fitting procedure allows to extract μ and n_{eff}, that are in the range of (1.2÷6.5)x10^3 cm^2/(Vs) and (1.6÷4.3)x10^{17} cm^{-3}, respectively, for the nanowires with diameters between 40 and 72 nm. These values are in a good agreement with the once reported previously for InAs nanowires with the similar dimensions [12, 23] (see also section 3.3). The reliability of the application of the SCLC model is, however, not sufficient due to the following reasons:

- The determination of V_c associated with a significant statistic error of 30-45%;
- Electron concentration and carrier mobility are included as the values averaged through the nanowire volume. This does not take into account domination of the surface in the electron transport;
- The low voltage part of the I-V curve should be linear, which is not the case.

The Joule heating of the nanowire can be estimated by solving the thermal conductance equation, assuming that the nanowire is connected at both ends to thermal sinks. Not going into the details, the temperature change in the center of the nanowire can be written as:

$$\Delta T_c = \frac{L}{8\kappa A} P, \tag{5.5}$$

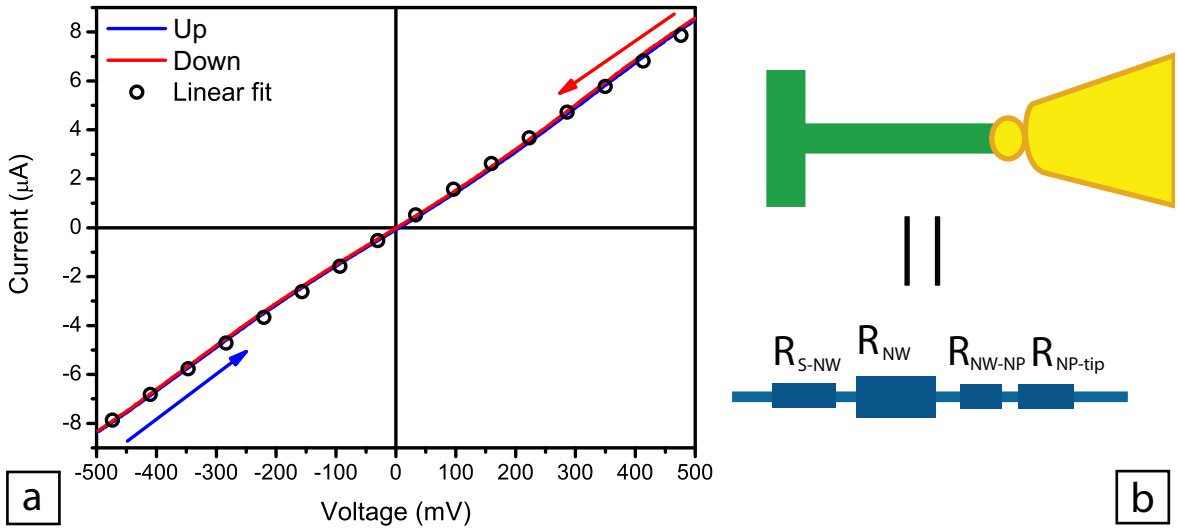

Figure 5.18.: Typical I-V curve (a) for the InAs nanowires. The measurement starts at -500 mV, when the voltage reaches +500 mV the direction was reversed (red line). The open circles show a linear fit which gives the conductance G =1.65 x 10^{-5} S. Scheme (b) shows the equivalent electrical scheme of the experiment, an InAs substrate with an InAs nanowire (green), gold nanoparticle on top of the nanowire, gold STM tip. At the bottom, blue squares represent the electrical resistances which are described in the text.

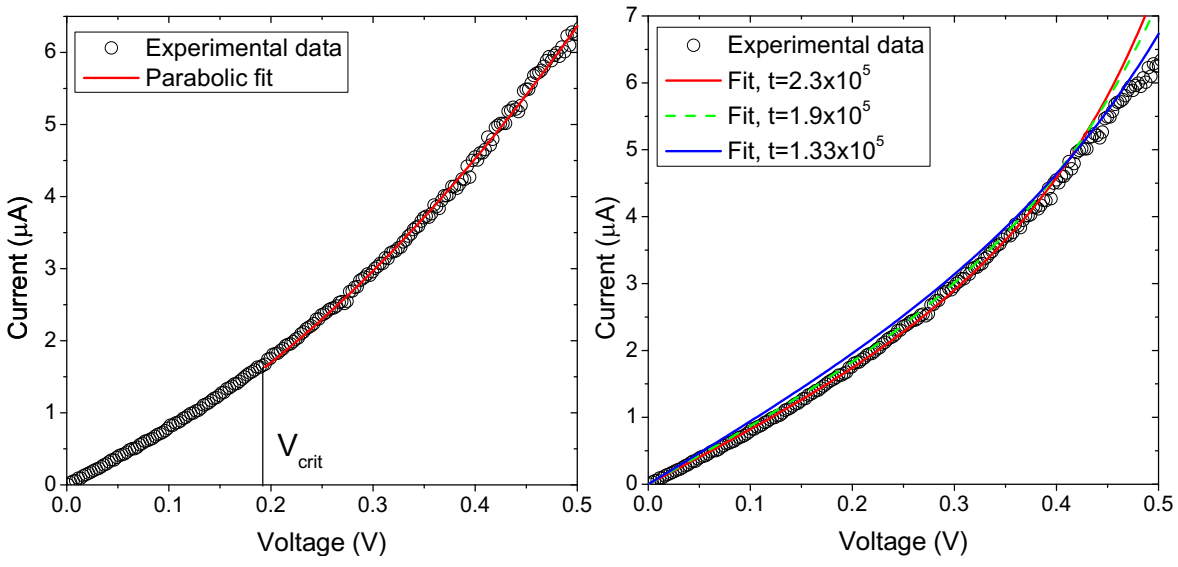

Figure 5.19.: An I-V curve recorded for an InAs nanowire with diameter of 52 nm and length of 8.7 μm (black circles in both graphs) fitted with parabolic function (red curve in (a)), which represents space charge limited current. Red, green and blue curves in (b) show fit according to equation 5.7 with problem parameter t. Parameter G_0 equal to 8.1x10^{-6}, 8.6x10^{-6} and 9.3x10^{-6} and coefficient of determination R^2 equal to 0.9783, 0.9858 and 0.9910 for red, green and blue curves respectively.

where L is length of the nanowire, κ is thermal conductivity, A is cross sectional area and P is electrical power transfered into the heat. The average temperature change ΔT in the whole nanowire will be approximately 2 times less than in the center. Since the change of the nanowire conductivity above room temperature can be approximated linearly (see figure 3.6 or reference [65]), the average conductance can be written as:

$$G = G_0(1 + \beta\Delta T), \tag{5.6}$$

where G_0 is conductance at room temperature, β is (linear) temperature coefficient of conductance. Using Ohm's law, equations 5.5 and 5.6, the relation between current I and voltage V can be written as:

$$I = \frac{G_0 V}{1 - G_0 t V^2}, \text{ where } t = \frac{\beta L}{16\kappa A}. \tag{5.7}$$

The experimental I-V curve was fitted using equation 5.7 using G_0 as fitting parameter and t as problem parameter (see figure 5.19 *a*). The graph shows that from red to green and to blue curve the fit quality increases (R^2 increases), however, the low voltage part fitted worser. Significant deviations of the fit curves from experimental data is due to the temperature dependence of κ which was not included in the model. Thus, red curve, which fits the low voltage part the best, is the most reliable fit. Its parameter $G_0 = (8.1\pm0.1)\text{x}10^{-6}$ S is equal to the conductance estimated from a linear fit of the low voltage part of the I-V curve $G = 8.2\text{x}10^{-6}$ S. The problem parameter $t = 2.3\text{x}10^5$ W^{-1} and $\kappa \approx 3.6$ W/(K m) from literature [65] deliver $\beta \approx 106$ K^{-1}, which is factor of 5 larger than the one obtained by Mavrokefalos and coworkers [65] for InAs nanowires above room temperature. The reliability of the application of the Joule heating model is not sufficient due to the following reasons:

- The fit does not converge if both t and G_0 used as the fitting parameters. Using t as a problem parameter results in a statistic error of about 20%.
- The temperature dependence of thermal conductivity is not included in the model;
- Thermal conductivity for the nanowires studied in this work can differ from the one used for the data analysis due to the presence of stacking fault defects;
- The fit does not deliver reasonable values for β. This, however, can be a consequence of the previous statement.

Concluding the stated above, both SCLC and Joule heating should occur in the nanowire and result in the non-nonlinearity of the I-V curves. To separate the contributions of these effects, however, is not possible. Thus, none of the fitting procedures can be applied.

The conductance of the nanowires was extracted by fitting of low voltage part of the curves ($V \leq$ 100-200 V) with a linear function. The linear relation can be used, since in this regime

the voltage is bellow crossover voltage of SCLC and the increase of the temperature can be neglected. The typical resistance calculated from the inverse slope of the fits is 50-150 kΩ. Figure 5.18 *b* shows the equivalent electrical scheme of the connected nanowire. The total resistance of the system can be written as:

$$R_{total} = R_{S-NW} + R_{NW} + R_{NW-NP} + R_{NP-tip}, \tag{5.8}$$

where R_{S-NW} is the resistance of the substrate-nanowire interface,
R_{NW} is the resistance of the nanowire itself,
R_{NW-NP} is the resistance of the interface nanowire-gold nanoparticle,
R_{NP-tip} is the resistance of the nanoparticle-gold STM tip contact.
The nanowire is epitaxially grown on the InAs substrate, and according to Glas et al. [80] the interface should be defect free since there is no lattice mismatch between the substrate and the nanowire. Therefore, the resistance of the interface (R_{S-NW}) is expected to be negligible small. According to the reports in the literature (reviewed in section 3.3) the resistance of an InAs nanowire (R_{NW}) with the diameter of 50 nm and length of 5 μm is expected to be on the order of several kΩ. The nanowire-gold nanoparticle interface is expected to be ohmic, and its resistance (R_{NW-NP}) was estimated in section 3.4 to a few Ω which is much smaller than the total resistance and can be neglected. The nanoparticle-gold STM tip contact resistance does not exceed 300 Ω according to the estimations done in section 3.4 and, therefore, can be neglected as well. Both statements are confirmed by electron holography which is described in section 4.3.4 and in the next paragraph. We conclude that in the framework of contact theory (section 3.4) the total resistance is approximately equal to the resistance of the nanowires. Since the dimensions of the nanowires were measured directly in TEM, and the cross section is known (see section 5.1.3), the resistivity of the nanowires can be calculated. Figure 5.20 shows the dependence of the resistivity of the nanowires of type 2 (with stacking faults perpendicular to the growth direction; see section 5.1.2) on their diameter. The resistivity values are consistent with previous studies [120, 121], the variations should be attributed to differences in preparation conditions, morphology and crystal structure. No dependence on diameter is seen and the data scatter by a factor of 5 in the investigated regime between 40 and 72 nm diameter. This can be interpreted as either contact resistances R_{NW-tip} and R_{S-NW} are significant and change from wire to wire, or the wire resistivities are different due to defects. Unintentional carbon doping[7], which was reported recently [121], can not cause the observed scattering of the data, due to following reasons:

- All the samples were grown at the same conditions, therefore, there is no reason for changes in the amount of doping, if there is;

[7] Carbon, which is coming from products of decomposition of the precursors, incorporate during the CVD growth of the nanowires.

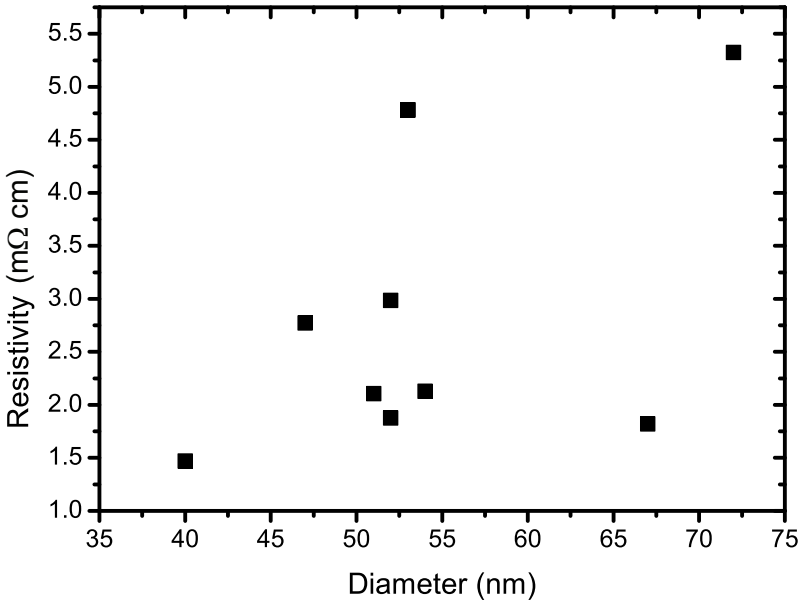

Figure 5.20.: Dependence of the resistivity of the "type 2" InAs nanowires on their diameter.

- The carbon doping does not seem to have a significant impact on the transport in the nanowires. The conclusions drawn in [121]: "...changes in the resistivity of InAs nanowires as the growth temperature and V/III ratio are changed, indicative of changing levels of carbon incorporation" and "...differences in crystal quality, here quantified as the stacking fault density, are not the primary cause for variations in resistivity of the material studied", can be faulty[8].

To check the contact issue the transfer length measurement (TLM) technique (see section 4.3.3) was applied to the wires with a diameter of about 50 nm. The dependence of the nanowire resistance on the length is shown in figure 5.21. The data points cannot be fitted with a linear function, thus, the resistivity of the wires differs from wire to wire.

The nanowires contain stacking faults (see section 5.1.2) which can influence the electron transport significantly [18]. Since there is no clear answer how the stacking faults change the electrical properties of the wires, we measured the electrical potential by electron holography, while sending simultaneously electrical current through the wires. It should be underlined here that for the holography experiment the nanowires were shaved from the substrate and deposited onto a piece of a copper TEM grid using dielectrophoretic deposition (see sections 4.3.2 and 4.3.4 for more details on the sample preparation and the reasons why those methods were chosen). Figure 5.22 *b* shows the I-V curve of the nanowire sample, which is clearly different from the usual observation (figure 5.18 *a*). The wire acts now like a tunnel diode [122], because the contact between the copper grid and the wire might be contaminated during the sample prepa-

[8]Indeed, table 1 in the reference [121] shows that the resistivity of the nanowires with different V/III ratios are equal within the error bars. The structural and electrical investigations have not been done on the same nanowire, whereas large error bars confirm that the nanowires may be different even within the same sample.

ration. However, the possibility to measure the electrical potential of the wire directly with nm spatial resolution using electron holography avoids the contact problem. The contrast of the reconstructed phase images from the holograms shows the relative phase shift of the electron waves after they passed through the sample, which according to equation 4.4 is proportional to the electric potential in the material in the absence of magnetic field. Figure 5.23 shows the phase images of the nanowire at different bias voltages U_B. Since the gold nanoparticle at the top of the wire was not transparent to the electron beam, the patterns inside it are artifacts. The graph in the middle of the image shows intensity profiles of the phase images at the top, taken along the lines. The movement of the lines towards the rim of the nanowire changes only offset of the profiles but not the behavior. The slope of the red curve (U_B = +2 V) is higher than the slopes of the black curve (U_B = 0 V) and the blue curve (U_B = -2 V). All three slopes are positive, even though at 0 V the wire along its whole length should have the same potential. This fact means that the contribution of the inner potential is not constant along the wire because of the diameter change. Thus, by subtracting the 0V profile from the intensity profiles recorded at U_B = +2 V and U_B = -2 V we can determine the phase change only due to the change of electrical potential along the nanowire (figure 5.23 bottom). The graph shows that the phase, which is proportional to the electrical potential multiplied by thickness, increases along the nanowire for U_B = +2 V and decreases for U_B = -2 V. This trend was expected and shows that the part of the nanowire which is closer to the substrate has higher (lower, for U_B = -2 V) electrical potential than the part near the contact with the STM tip.[9] Both profiles do not show any features (e.g. local minima or maxima) which could be attributed to the stacking faults. To increase the signal to noise ratio the -2 V profile was subtracted from the +2 V profile resulting in the intensity profile which shows the relative phase change (see black line in the graph in figure 5.24). The profile can be correlated with the bright field TEM image of the same nanowire where the stacking faults are visible as dark stripes. No change of the electrical potential can be detected at stacking faults. The phase resolution of our particular electron tomography experiment is $\phi_{lim} \approx 0.1$ rad, and the corresponding voltage detection limit can be calculated by:

$$\phi_{lim} = C_E V_{lim} t_{NW}, \tag{5.9}$$

where C_E = 0.00856 rad / (V nm) at 120 keV is an interaction constant, which was calculated using equation 4.3; t_{NW} = 69 nm is the nanowire diameter. It can be concluded here that either stacking faults do not create any potential change, or the potential change is smaller than 0.15 V per 4 V applied to the nanowire.

The holography data can also be used to calculate the resistivity of the nanowires. The slope b_ϕ of the line profiles of the phase images (figure 5.23 bottom) is related to the resistivity ρ in

[9] U_B = +2 V (-2 V) is applied to the source of the nanowire and the top of the wire is grounded by the STM tip

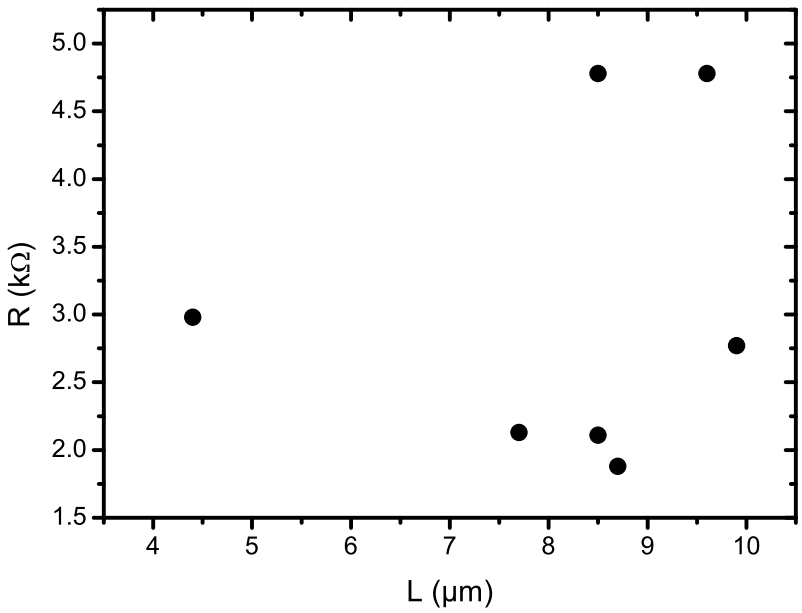

Figure 5.21.: Dependence of the resistance of InAs nanowires (two point contact measurement) with a diameter of about 50 nm on their length.

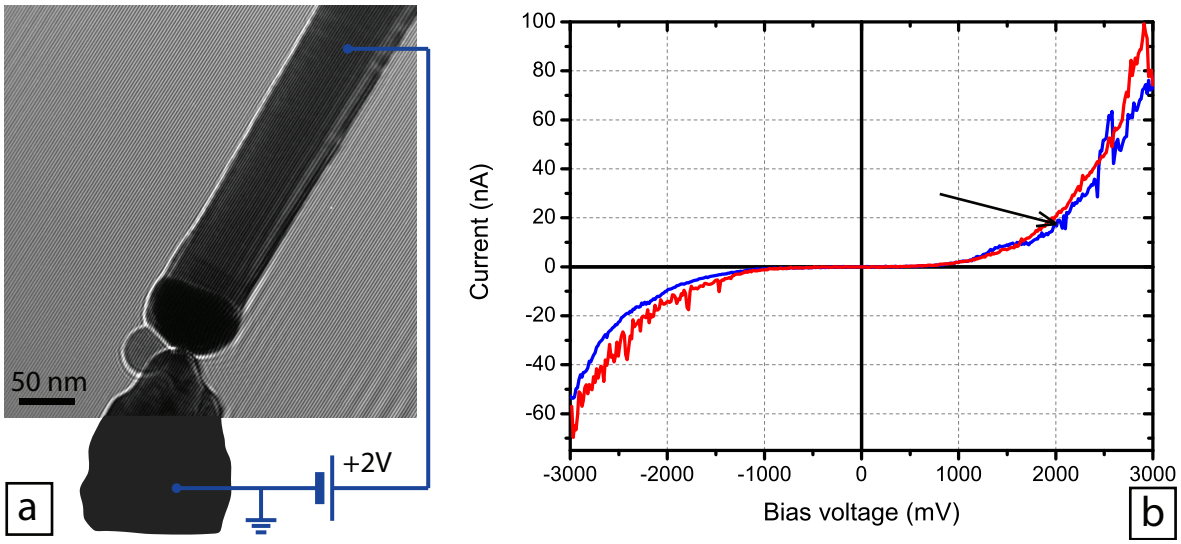

Figure 5.22.: (a) Experimental hologram of a nanowire at bias voltage +2V applied to the wire with schematically shown electrical connections (blue lines). At the bottom of the scheme is the STM tip. The I-V curve (b) of the system was recorded prior to the hologram without changing the setup. Blue curve is in ”up” direction, red is in ”down” direction (see section 4.3.3). The black arrow indicates the voltage at which the hologram (a) was recorded.

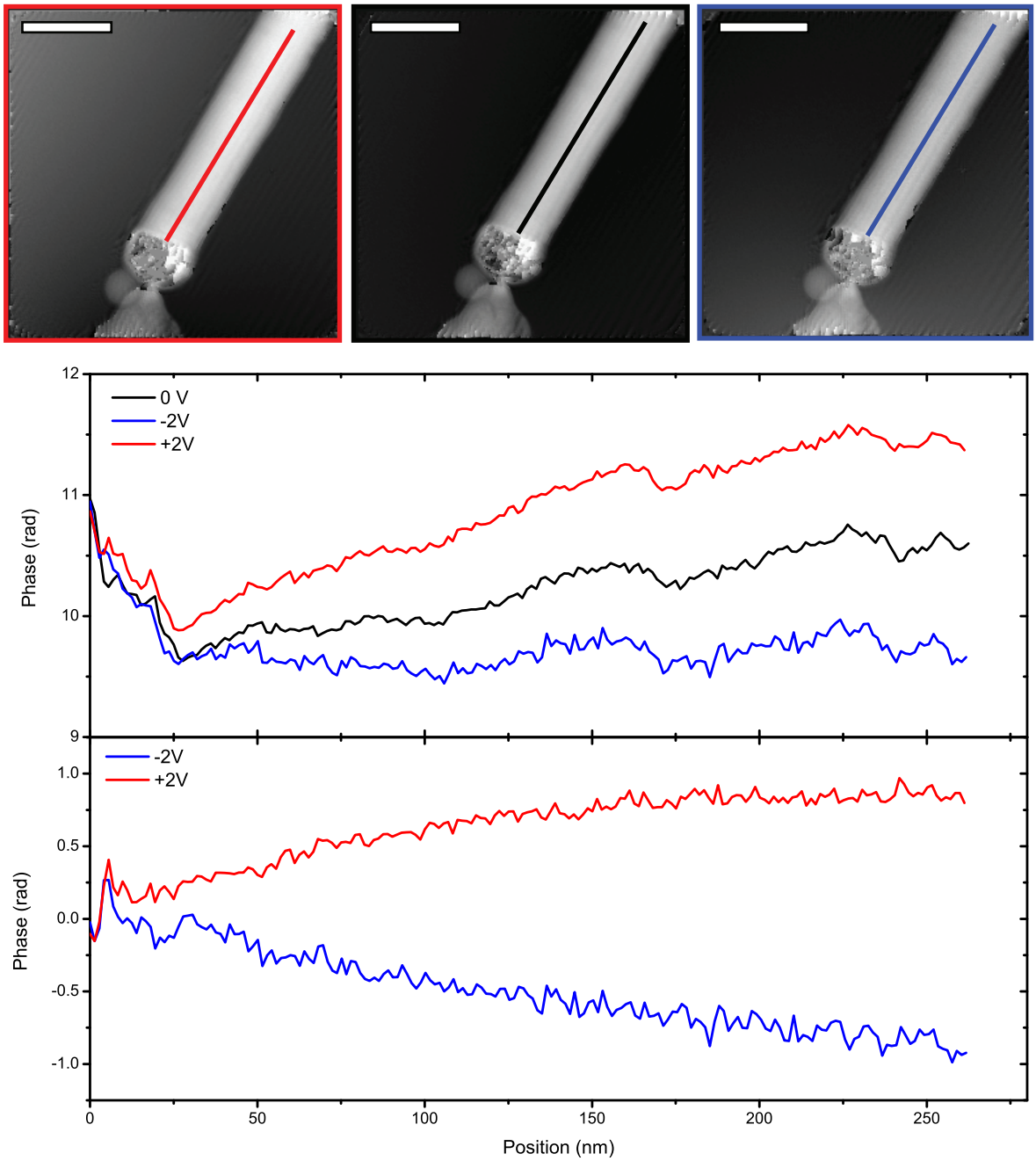

Figure 5.23.: Electron holography phase images of an InAs nanowire (top). Taken at a bias voltage U_B of (from left to right) +2 V (red), 0 V (black), -2 V (blue). The scale bar is 100 nm. The graph in the middle shows intensity profiles taken along the lines (with a thickness of 3 px, which was used to integrate the signal) shown in each phase image. The graph at the bottom shows the +2 V and -2 V profiles after subtraction of the 0 V profile.

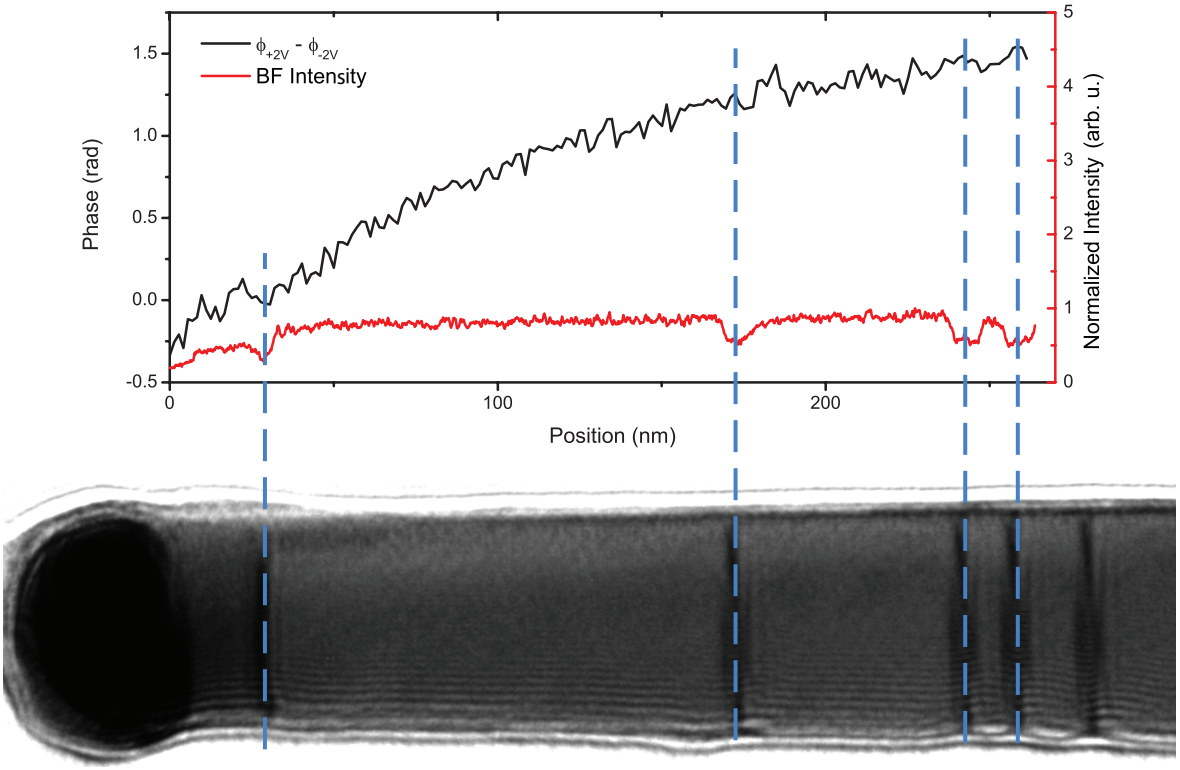

Figure 5.24.: Difference of electron phase recorded at U_B = +2 V and U_B = -2 V (black line, left y-axis). The intensity profile of the bright field (BF) TEM image (bottom) is shown with the red line (right y-axis). The local minima identify positions of the stacking faults (blue dashed lines and black stripes at the TEM micrograph).

the following way:

$$\rho = \frac{b_\phi A}{I C_E t}, \tag{5.10}$$

where A is the cross sectional area of the nanowire, I is the electrical current flowing through the nanowire, C_E is the interaction constant (see above), t is the nanowire diameter[10]. Before the analysis the phase images were checked for artifacts and the signatures of external electric fields which might contribute to the slope in the phase profiles. Figure 5.25 shows the contour plots of the phase which correspond to the phase images in figure 5.23. The phase shift between two nearest equiphase lines is equal to $\pi/2$. The change of the phase in vacuum confirms the presence of external electric fields. Ideally the fields should be subtracted by simulating the charge configuration which causes the fields. Since it is very difficult to identify the sources of the fields, the phase shift produced by the external electric fields was interpolated from the vacuum region for the whole image. Figure 5.26 shows the interpolated images (*a*-*c*) and the result of their subtraction from the original images[11] (*d*-*f*). The last will be called "approximated images" in further text. The interpolated image does not posses any phase wrap and looks smooth. The approximated image does not contain background (phase change due to external electric fields). However, the noise in the nanowire region increases due to interpolation uncertainties. After the background subtraction the line profiles (figure 5.27) of the phase images should represent a change of the electric potential inside the nanowire. Unfortunately, the line profiles are flat and do not show any change of the phase along the nanowire at any bias voltage. Thus, the potential change inside the nanowire cannot be detected within the noise level. The main reason is the high mobility of the charge carriers in the InAs nanowires ($\sim 10^3$ cm^2/(V s)) and the decrease of the sensitivity of the measurement due to subtraction of the interpolated background. Those two factors make it impossible to calculate the resistivities of the wires from the holography experiment.

The most significant result of the holography is the electric field distribution at the STM tip interface. No electric stray fields around the interface are detected. Figure 5.28 shows a typical contour phase image of a nanowire in contact with a very thin carbon layer attached to the STM tip. There are no stray fields around the contact area as well as no abrupt change of the phase within the contact region. This finding confirms the estimations of the negligible contact resistance in section 3.4.

To analyze the data obtained by 2 point contact measurement, I propose the following model:

1. Only the resistances of the nanowire-gold nanoparticle interface R_{NW-NP} and the nanowire itself contribute to the total resistance;

[10] Here the changes the cross section along the nanowire axis are neglected. Otherwise, the equation 5.10 should be rewritten.

[11] The original images are shown at the top of figure 5.23.

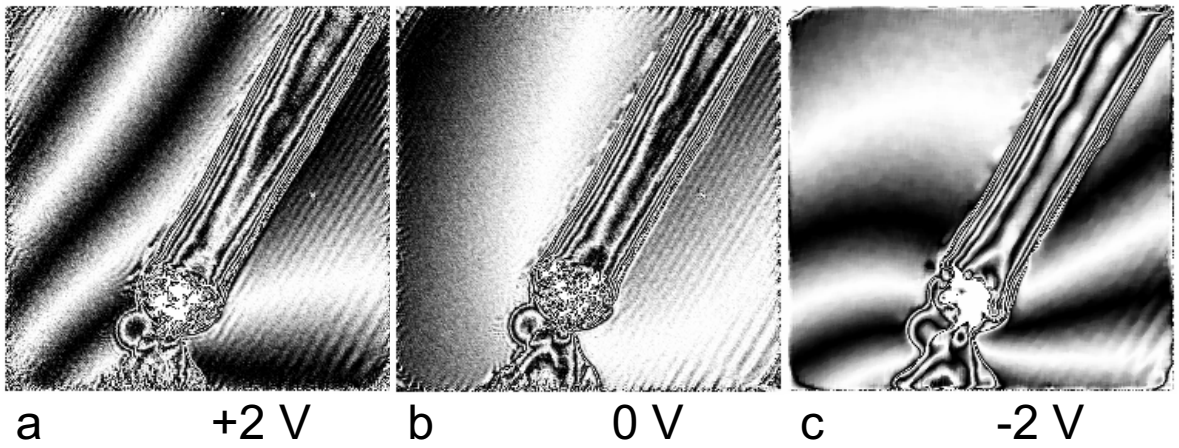

Figure 5.25.: Contour maps of the holographic phase images which are shown in figure 5.23. Black and white stripes show equiphase lines, the phase shift between two next black (or white) lines is $\pi/2$.

2. The resistance of the interface R_{NW-NP} is proportional to the cross sectional area (or simply the square of the diameter of a nanowire).

Going back to the graph in figure 5.20 (obtained by in-situ two point measurements of resistivity of the nanowires versus their diameter) we will try to find the difference between the nanowires with resistivity[12] around 1.5, 3.0 and 4.5 mΩ cm comparing their micrographs. It is expected that the difference in the stacking fault density causes this variation of the resistivity.

The nanowires with low stacking fault density and diameter around 50 nm were used to determine the resistance of the nanowire-gold nanoparticle interface using the transfer length measurement method. The estimated resistance $R_{cont,50}$ is equal to 32±12 kΩ. According to the model which was formulated above the resistivity of the nanowire ρ_{NW} can be calculated as following:

$$\rho_{NW} = (R_{total} - \frac{50^2}{D^2} R_{cont,50}) \cdot \frac{A}{L}, \tag{5.11}$$

where R_{total} is the series resistance of the nanowire and the interface with nanoparticle, D is the nanowire diameter, A and L are its cross section area and length respectively. Figure 5.29 shows the dependence of resistivity of the InAs nanowires (calculated according to equation 5.11) on their diameter. The stacking fault (SF) density is shown with the colored data points and listed in the legend[13]. One sees that all blue points shows the lowest resistivity which slightly increases with diameter. Red points show higher resistivities than the blue onces, and it increase with the diameter is more pronounced. Green points show almost the highest resistivities, and it slight increase with the diameter. Two trends can be mentioned:

[12] Here, the resistivities were calculated neglecting the resistance of the interface between a nanowire and gold nanoparticle.

[13] Black squares ("Unspecified" stacking fault density) represent the nanowires which could not be oriented in the microscope in the way that the stacking faults are visible.

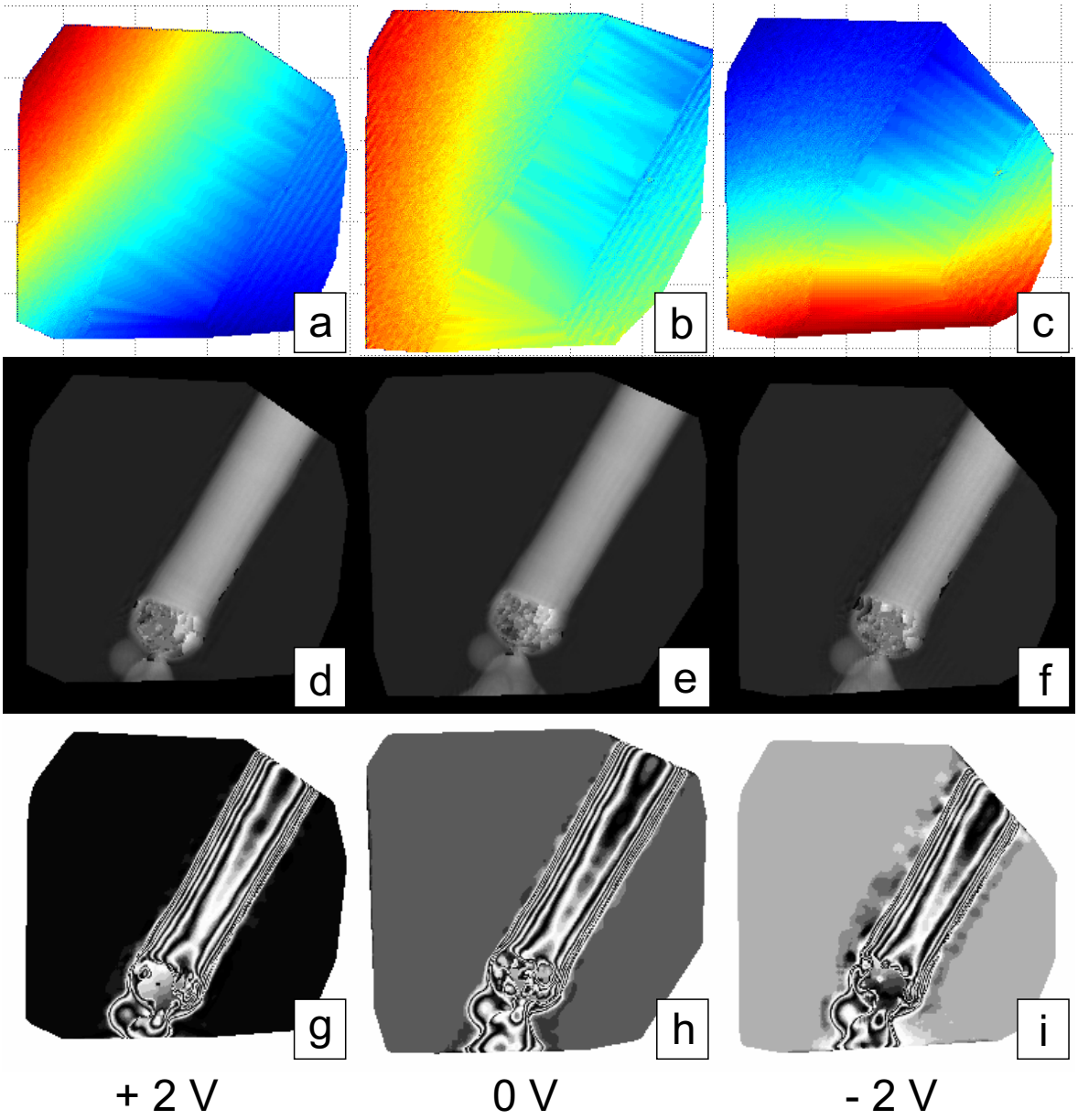

Figure 5.26.: Interpolated phase (a-c) of the images in figure 5.23 are shown as normalized color maps (red is 1, blue is 0). Phase images with subtracted background (d-f) and their contour maps (g-i), in which the difference in phase between two next equiphase lines is equal to $\pi/2$. Images *a, d, g* correspond to a bias voltage of +2 V, *b, e, h* correspond to 0 V and *c, f, i* correspond to -2 V.

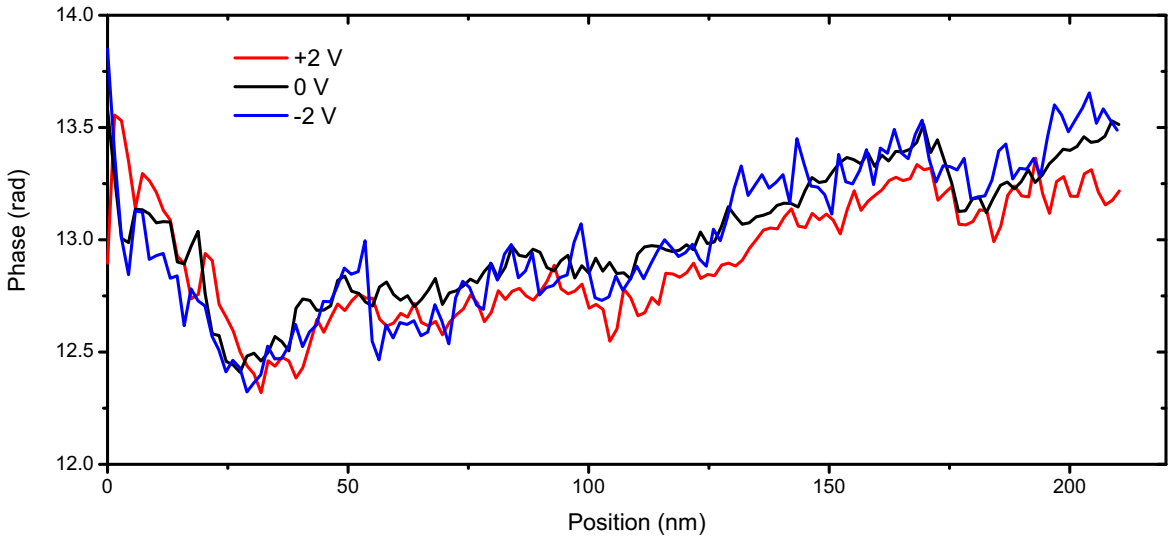

Figure 5.27.: Line profiles of the corrected phase images (figure 5.26 *d-f*) recorded along the nanowire axis. Red line shows the phase at U_B = +2 V bias voltage (figure 5.26 *d*), black line shows the phase without any bias voltage (figure 5.26 *e*) and blue line shows the phase at U_B = -2V (figure 5.26 *f*).

- **the higher the stacking fault density is, the higher is the resistivity of the nanowires**;
- **the resistivity increases with the nanowire diameter** (for the nanowires with diameters between 40 and 75 nm).

The tendency of the thicker wires to show higher resistivity contradict to the findings of Scheffler et al. [120] and Thelander et al. [121], in which no dependence on diameter was observed in this regime[14]. This phenomenon can be explained using a core-shell model for the nanowires, consisting of a poorly conductive cylindrical core surrounded by a thin shell with conductivity higher by several orders of magnitude (see figure 5.30 *a*). This assumption makes sense, since the surface of the InAs nanowires possesses charge accumulation (see section 3.1). The core and the shell are connected in parallel which results in a total resistance of the nanowire $R_{total} = (R_c^{-1} + R_s^{-1})^{-1}$, where R_c and R_s are the resistances of the core and the shell, respectively. The following formula for the effective resistivity of the nanowire ρ_{eff} can be easily observed:

$$\rho_{eff} = \frac{\rho_c \rho_s D_0^2}{t_s(2D_0 - t_s)\rho_c + (D_0 - t_s)^2 \rho_s}, \tag{5.12}$$

where ρ_c and ρ_s are the resistivities of the core and the shell, D_0 is the outer diameter of the nanowire, t_s is the radial thickness of the shell (figure 5.30 *a*). Since the parameters ρ_c, ρ_s and t_s in equation 5.12 are undefined and the graph in figure 5.29 contains only few data points for each stacking fault density, no reasonable fitting of the data points can be performed. On the other hand, graphs *b*, *c* and *d* in figure 5.30 show the calculated dependencies according to

[14] It should be underlined, that the measurements of resistivity in the references were done without direct correlation with atomic structure for each nanowire

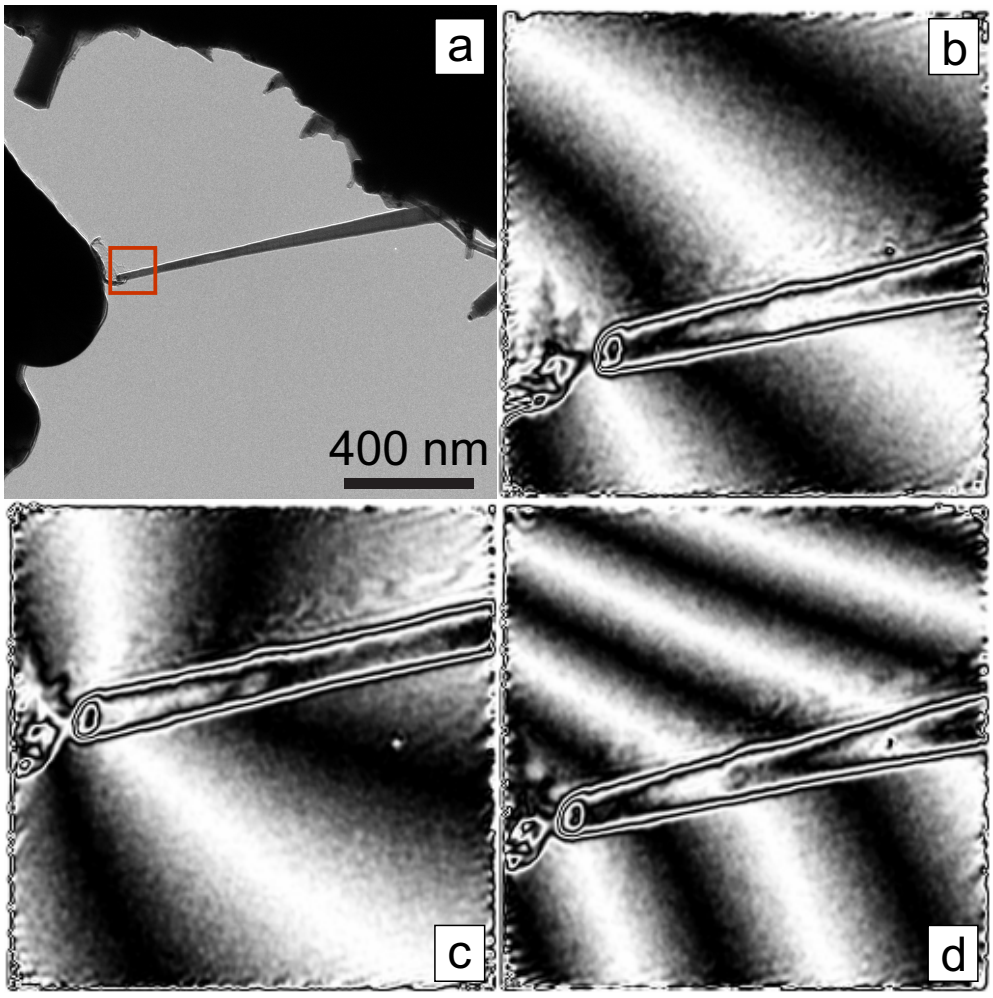

Figure 5.28.: (a) Bright field TEM micrograph of an InAs nanowire in contact with an STM tip. The area which is shown on the phase contour images (b-d) is shown within the red box. The contour phase images shows a phase amplified by a factor of 4 (a phase change between two next black lines is equal to $\pi/2$) at different bias voltages applied between the nanowire and STM tip: b) +1 V, c) -1 V, d) +2 V.

equation 5.12. The effective resistivity of the nanowires increases with the diameter until the resistivity of the core is higher than the resistivity of the shell. The slope of the curves depends on all three parameters. Since we observe an increase of the effective resistivity of the nanowires with the increase of the defect density (figure 5.29), both (core and shell) resistivities can decrease with the increase of stacking fault density. As shown in section 5.1.4 the stacking fault changes the orientation of the next nearest neighbor along with the tetragonal bonds direction. This change of the lattice periodicity may result in an abrupt change of the electrostatic potential resulting in a potential barrier for the conduction electrons. The nanowire shell conductance caused by the free electrons that situated between conduction band minima and Fermi level. But the core of the nanowire most probably has properties of intrinsic semiconductor (Fermi level remain bellow conduction band minima). Therefore, I suggest that stacking faults increase the scattering of the charge carriers in the shell, thus, increase the resistivity of the shell. In the core, due to the change of the potential field and intrinsic semiconductor nature of the core, the stacking faults will produce additional energy levels within the band gap. This will result in a decrease of the core resistivity. Since figure 5.30 *d* shows that the change of the core resistivity slightly influences the total resistivity, the total resistivity increases with the increase of the stacking fault density. To extract more quantitative data one needs to obtain more statistical data on the dependence of electrical transport in the nanowires on diameter and defect density.

5.3.2. Dependence of electron transport on electron irradiation and magnetic field

The magnetic field dependent experiments were made utilizing the magnetic field of the objective lens of the Phillips CM12 TEM. Its magnitude at the sample position can be set either to 1 T or to 70 mT. The magnetic field of the TEM lens is perpendicular to the imaging plane, therefore the angle between a nanowire and the field is typically in a range of 60°-90°. All the experiments were done at room temperature, without the electron beam irradiation. Electronic noise was approximately 10 nA (for the measurement range of 5 μA). Figure 5.31 shows the I-V curves of an InAs nanowire at different magnetic fields. The nanowire axis was inclined with an angle of less than 5° to the image plane, meaning that the experiment was performed in transversal geometry (magnetic field is perpendicular to the current). Both I-V curves are linear with R $\approx$ 170 kΩ. No difference between the curves can be detected. The noise increases significantly for the voltages higher than 100 mV and reaches 100 nA. This noise can probably be associated with space charge effects, which were described in section 5.3.1. Instabilities of the space charge can lead to the charging/discharging events, that increase noise in the current. In our measurement the noise level of 10 nA results in an error of 1.6% for the resistivity, which, however, can be higher due to the current fluctuations in the nanowire itself. In these experimental conditions magnetoresistance bellow 2.5 % can not be detected.

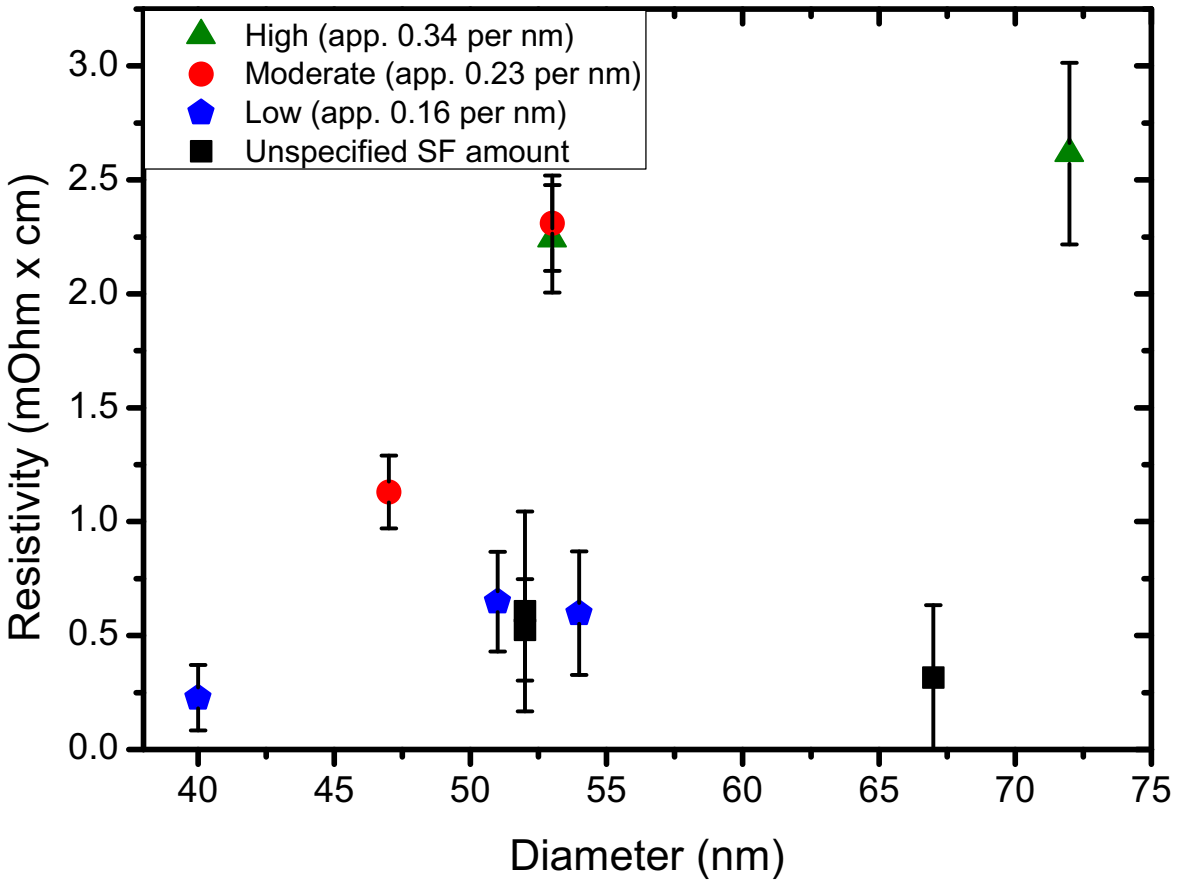

Figure 5.29.: Dependence of resistivity of the nanowires on their diameter. The density of the stacking faults (SF) is shown with different colors and shapes as listed in the legend.

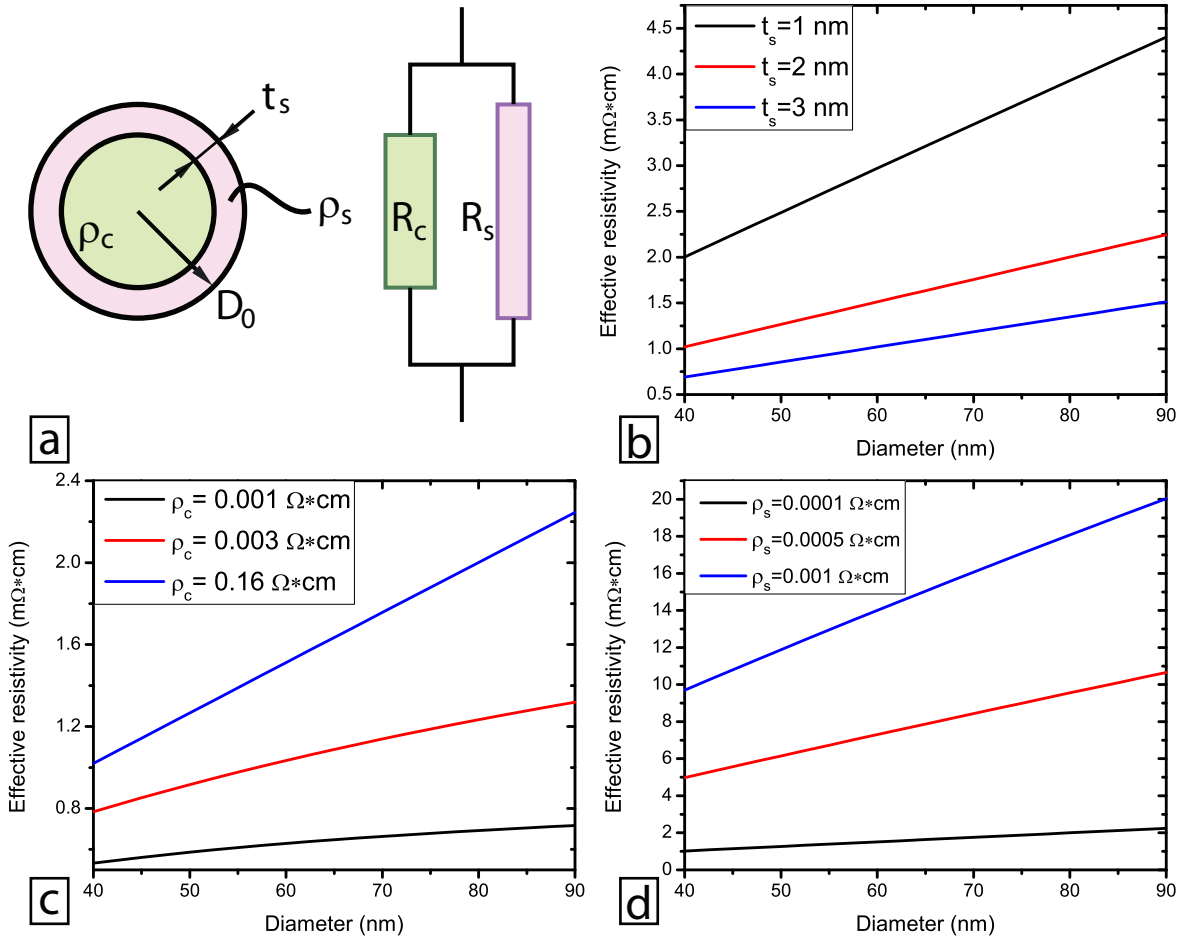

Figure 5.30.: (a) Schematic representation of the core-shell model. Cross section of the core-shell nanowire is shown on the left, the resistances discussed in the text are shown on the right. (b-d) Dependences of the effective nanowire resistivity calculated according to equation 5.12. For all simulations the parameter D_0 is set to 50 nm. In (b) ρ_c = 0.16 Ωcm (intrinsic InAs) and ρ_s = 0.0001 Ωcm. In (c) parameters t_s = 2 nm and ρ_c = 0.0001 Ωcm. And in (d) parameters t_s = 2 nm and ρ_s = 0.16 Ωcm.

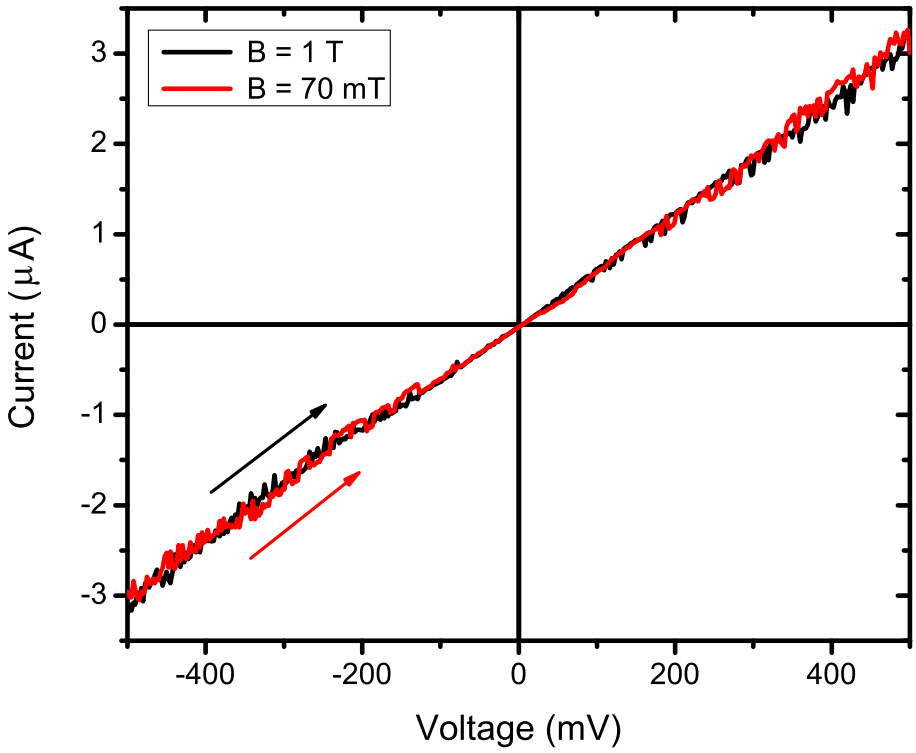

Figure 5.31.: I-V curves of a nanowire recorded in a magnetic field of 1 T (black) and 70 mT (red). Both curves were recorded sweeping voltage from -500 mV to 500 mV.

The measurements of the transversal magnetoresistance (MR) were reported for InAs single crystalline bulk samples [123, 124]. The MR $\Delta\rho/\rho$ at room temperature reaches 2.4% at 1 T and 0.03% at 70 mT. To my knowledge magnetoresistance in InAs nanowires was investigated only at low temperatures with applied gate voltage V_G. No magnetoresistance was detected at V_G = 0. Small oscillations of electron mobility (at V_G = 0) with magnetic field and significant device-to-device variations were found [125]. These variations were associated with high sensitivity to geometry of the nanowire and external field. In summary, the MR in the nanowires should be a subject of more systematic study with the increased sensitivity.

The effect of electron irradiation on the electron transport in InAs nanowires has not been reported in the literature yet. I performed the electrical characterization at room temperature, in vacuum, with magnetic field of 70 mT applied with an angle of 60°-90° with respect to the nanowire axis. Figure 5.32 shows I-V curves of the InAs nanowire under different illumination conditions. The electron beam irradiation with electron flux Φ = 8000 $\bar{e}$/(nm^{2}s) results in an increase of the nanowire resistivity, it increases the noise in the I-V curves and disturbs the linearity of the curves. To explain this experimental finding the following interactions of the electron beam with the material should be considered:

- Inelastic electron scattering with subsequent X-Ray photon generation (higher scattering cross section);

- Inelastic electron scattering with subsequent secondary electron generation (lower scattering cross section);
- Thermal heating of the sample as a result of the energy transfer from an excited electron subsystem to phonons;
- Momentum (both angular and linear [126]) transfer from electron beam the atoms. It can result in the electron beam induced sputtering of the material or sample recrystallization. These effects lead to the change of morphology which was not observed in the experiments.

The increase of the temperature of the sample usually does not exceed 10-20 °C. Since the conductivity of InAs nanowires is expected to increase with temperature [65], the heating of the nanowires by the electron beam will result in a decrease of the resistance by 5-10%. Since we observed an increase of the resistance by more than 200 %, the impact ionisation of the nanowires should play a dominant role. First, the secondary electron generation causes a decrease of the electron concentration in the nanowires and, thus, reduction of the nanowire conductance. Second, the sample will be positively charged due to the loss of electrons resulting in an additional discharge current which is opposite to the electron current, and effectively increase the measured resistance. The instability of the discharge current is probably the main reason for the increase of the noise in the corresponding I-V curves (figure 5.32). The non-linearity of the I-V curves under the electron beam irradiation is more difficult to explain. Since the nanowire is effectively composed of two different types of material: semiconducting InAs in the core and InAs with depleted bands at the surface (as proposed in the core-shell model described above), the electrom beam can differently affect different parts of the wires. One possible reason is a change of conductance regime from drift conductance to the space charge limited conductance. In the last case the electric current is limited due to low electron concentration. The free electrons, injected from the metal electrodes, will form a space charge near the metal-nanowire interface. The charges will produce an electric field in opposite direction to the current flow. This effect can be affected by the formation of additional space charges due to the electron beam. Since the charges produced by the electron beam irradiation are randomly distributed, the space charges will fluctuate increasing the noise in the current-voltage characteristic (figure 5.32 blue and red lines).

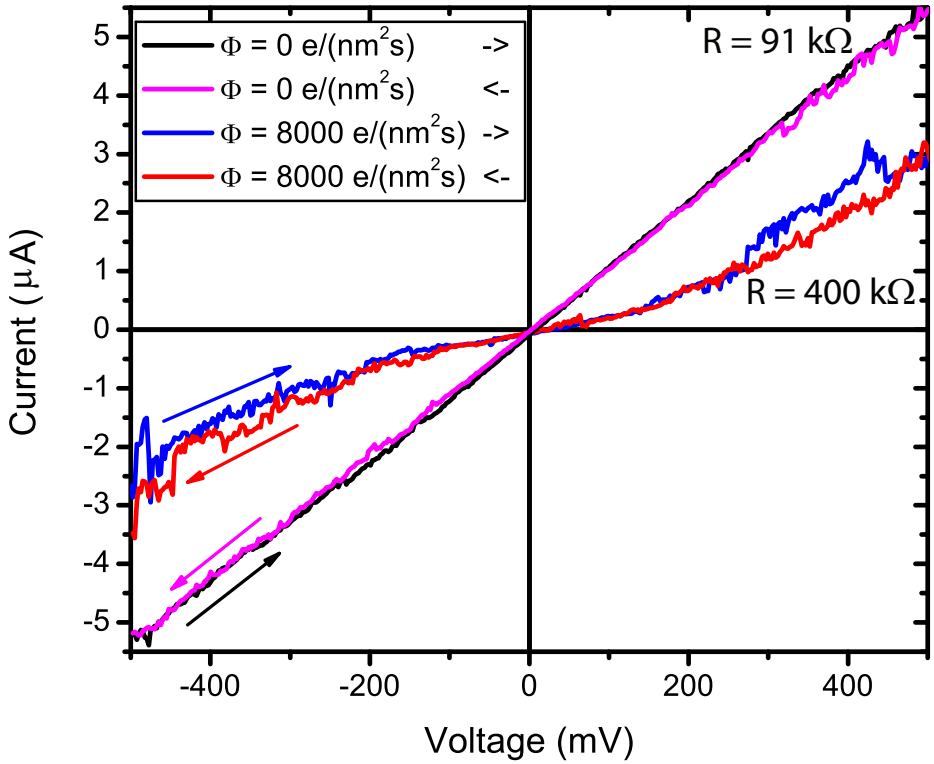

Figure 5.32.: I-V curves of a nanowire recorded at different average fluxes Φ of the electron beam and different directions of the voltage sweep (see the legend).

6. Summary and conclusions

In this work electron transport and the elastic properties of InAs nanowires were studied in the correlation with the atomic structure. The morphology, chemical composition and atomic structure were fully characterized using different electron microscopy techniques. The results of the first two are in a good agreement with the literature. The key issue of the structural study was the identification of the atomic structure of twin defects in ⟨111⟩-oriented InAs nanowires, for the first time. The scanning transmission electron microscopy experiment reveals that all defects in the nanowires are ortho-type, meaning 60 degree rotational twins. These findings are important for the interpretation of the mechanical and electrical experiments done in this work, as well as for the future characterizations of the nanowires.

Novel in-situ characterization methods were used to investigate the elastic properties and electron transport of InAs nanowires: i) analysis of bending behavior of the nanowires combined with its direct observation in TEM and with electron diffraction; ii) in-situ TEM electron holography combined with the electrical biasing of the nanowire. The first method allows to correlate the macroscopic strain in the nanowire with the crystal structure and to correlate the atomic distortions with the force applied to the nanowire. The second method (electron holography on the electrically biased nanowire) allows to access the distribution of the electrical potential in a nanowire when an electrical current is flowing and to directly image the potential for different currents passing through the wire. The electrical potential can be correlated with the structural peculiarities of the nanowires (i.e. stacking defects).

The elastic properties were studied for nanowires with two different growth directions: ⟨112⟩ and ⟨111⟩. Both types of the nanowires have stacking fault defects. In the ⟨112⟩-oriented ones the defects are parallel to the nanowire axis, whereas in the ⟨111⟩-oriented wires the stacking faults are perpendicular to the axis. All nanowires show harmonic response to the sinusoidal excitations and Q-factors above 1000, that makes them quite attractive for the applications in nano electromechanical systems.

For the ⟨112⟩-oriented nanowires the diameter dependence of Young's modulus possesses a local maximum at 50 nm. The increase of Young's modulus at this point approaches 300 % of the bulk value. For the thinner nanowires as for the thicker ones the Young's modulus decreases down to the bulk InAs value. Obviously this trend is determined by the stacking faults, whose density may vary with the diameter of the nanowires. The reasons for such a dependence

of Young's modulus lies most probably in lattice distortions which arise in the nanowire due to stacking faults. The distortions were confirmed by selective area electron diffraction. The anisotropic lattice expansion of 9.4 ± 0.5 % in one of the ⟨112⟩ directions results in internal strains which significantly change the deformation behavior of the nanowires. Indeed, the electron diffraction of the deformed nanowire confirmed that its deformation is not homogeneous and combines bending with other deformation types (twisting, compression). The further analysis would require simulations of the deformations taking into account the lattice distortions, that should be studied precisely and systematically.

Regarding the elastic properties of the ⟨111⟩-oriented nanowires, it was shown that Young's modulus increases for the nanowires with diameter D = 65 nm by a factor of 2. For the thicker nanowires with D = 120 nm it reaches the bulk value of InAs. The simultaneous measurement of the crystal structure shows that the higher the stacking fault density is, the higher is Young's modulus of the nanowires. Previously it was believed, that the stacking faults have no effect on Young's modulus of the nanowires [33]. The described experimental result can be a consequence of several effects: i) distortion of the lattice in the stacked region; ii) redistribution of electron density in the stacked region. The distortion of the lattice for the ⟨111⟩-oriented nanowires is much smaller than the one in the ⟨112⟩-oriented wires (about 0.2 % [102] agains 9 %) since the area of the defect planes is much smaller for the first ones. The effect of these distortions on the elastic properties is negligeable. It was deduced that the electron redistribution is the most significant mechanism, which is responsible for the observed correlation of the Young's modulus with the defect density. I expect the electron accumulation at the defects due to the scattering, which is not uniform along the nanowire axis. The accumulation will result in stronger bonding and thus increase of the Young's modulus.

The electrical resistance of the ⟨111⟩-oriented nanowires was measured by the two-point contact method. The contact resistances were found to be negligible small compared to the nanowire resistances. The linearity of the I-V curves in the low voltage regime (below 100 mV) confirms the formation of donor-type surface states in the nanowires as it is suggested in the literature. The slight non-linearity above 100 mV was due to space charge limited current and Joule heating phenomena. The separation of those effects, however, was not possible. It was shown by calculations and the electron holography that the scattering of the data is not due to the contribution of the contact resistances. The main reason for the scattering of the data is, therefore, the variation of the stacking fault density. However, electron holography could not resolve a change of the electric potential at the stacking faults. The nanowires could be categorized in three groups according to the defect density. It was found that the higher is the defect density, the higher is the resistivity of the nanowires. To explain the experimental data I proposed the following model: the nanowire consists of a poorly conductive cylindrical core surrounded by a highly conductive shell (electron accumulation layer). Since no variation

of electrical potential at the stacking faults was detected, the increase of the resistivity was attributed to the enhancement of the electron scattering at the defects within the shell. The enhanced scattering should result in a significant decrease of the electron mobility within the shell but not within the core. A slight decrease of the effective electron mobility due to stacking faults was reported before.

In addition it was found that: i) electron beam irradiation with flux Φ = 8000 $\bar{e}$/(nm^{2}s) and energy E = 120 kV drastically (up to factor of 3) increases the resistance of the nanowires; ii) the change of magnetic field between 70 mT and 1 T does not impact electron transport in the nanowires. The first finding can be attributed to the extraction of secondary electrons due to interaction of In and As atoms with the electron beam, and consequent reduction of the electron concentration in the nanowire. The secondary electron emission results also in random charging and discharging events, that increase the noise in the electrical current. The absence of the nanowire response to magnetic field at room temperature is due to the detection limits of the experimental setup. The resistance changes below 2.5 % could not be detected, meaning that the magnetoresistance in the nanowires does not exceed bulk value which is about that value for magnetic field of 1 T.

Appendices

Appendix A.

Parameters of InAs, InAs nanowires and related materials and devices

A.1. Parameters of bulk InAs and InAs nanowires

Table A.1.: Basic parameters of InAs. "ZB" states for Zinc Blende structure. The data for bulk InAs is taken from [127–129].

	Bulk	Nanowires		
Parameters	Value	Value	Diameter (nm)	Reference
Crystal structure	ZB	ZB / Wurtzite	10 ÷ 120	[70, 71]
Lattice constant (Å)	6.0583	6.058 ± 0.024	20 ÷ 70	[102]
Band gap (eV)	0.354	0.7 ÷ 1.8	10 ÷ 2	[61], fig. 3.4
Effective electron mass (m_0)	0.023	0.04 ÷ 0.18	10 ÷ 2	[61], fig. 3.4
Carrier concentration (cm^{-3})	10^{15}	10^{17}-10^{18}	20 ÷ 110	[12, 23, 65]
Electron mobility ($cm^2/(V\ s)$)	≤4 x 10^4	0.5-3 x 10^3	20 ÷ 110	[12, 23]
Intrinsic resistivity (Ω cm)	0.16	10^{-3} - 1	20 ÷ 100	[120, 121]
Dielectric constant (static)	15.15		NA	
Elastic constants (GPa)				
c_{11}	83.4		NA	
c_{12}	45.4		NA	
c_{44}	39.5		NA	
Young's modulus [111](GPa)	97	38 - 95	40 ÷ 100	[33]

A.2. Parameters of InAs and other III-V semiconductors

Table A.2.: Comparison of basic parameters of InAs and other III-V semiconductors. The data is taken from [127–129].

Parameters	Material			
	InAs	GaAs	GaP	GaN
Crystal structure	Zinc Blende	Zinc Blende	Zinc Blende	Wurtzite
Lattice constant (Å)	6.0583	5.65325	5.4505	3.189, 5.186
Mass density (g/cm^3)	5.68	5.32	4.14	6.15
Band gap type	direct	direct	indirect - X	direct
Band gap (eV)	0.354	1.42	2.26	3.2
Effective electron mass (m_0)	0.023	0.063	0.22	0.20
Electron affinity (eV)	4.9	4.07	3.8	4.1
Intrinsic carrier concentration (cm^{-3})	10^{15}	2.1 x 10^6	2	10^{-4}
Electron mobility (cm^2/(V s))	≤4 x 10^4	≤8500	≤250	≤1000
Holes mobility (cm^2/(V s))	≤5 x 10^2	≤400	≤150	≤350
Intrinsic resistivity (Ω cm)	0.16	3.3 x 10^8	NA	NA
Young's modulus [100](GPa)	51.4	85.9	103	181

A.3. Q-factors of different electromechanical resonators

Table A.3.: Q-factors of different electromechanical resonators. "CNT" states for carbon nanotube.

Resonator	Dimensions	Material	Geometry	**Q-factor**	Frequency (MHz)	Young's modulus (GPa)	Ref.
Nanowire, triangular cross section	D=36-84 nm, L=3.2-11.2 μm	GaN	one-end clamped	500-2800	~2	≈ 250	[32]
Nanowire, triangular cross section	D=16-53 nm, L=1.4-3.1 μm	W_xO_y	one-end clamped	≈ 600	2-8	100-300	[36]
Electrically gated CNT at room temperature	D=10nm, L=500nm	C	one-end clamped	≤500	0.01-0.4	NA	[130]
Electrically gated CNT at mK temperatures	D ≈1.6 nm, L ≈800 nm	C	double-end clamped	≤10^5	0.3	~1000	[131]
Strained nanobeam	75 μm x 500 nm x 105 nm	SiN	double-end clamped	≤3.9 10^5	≈4	≈200	[115]

Appendix B.

List and description of attached multimedia files

The printed version of the thesis has a compact disc (CD) with supporting multimedia materials attached to the back cover. The CD has the following content:

- `Migunov-V_phd_thesis.pdf` (full path: "`../00_Thesis_e-version/Migunov-V_phd_thesis.pdf`") - electronic version of the thesis in PDF format with links and high resolution figures.

- `tomo_t1.mpg` (full path: "`../01_Electron_tomography/tomo_t1.mpg`") - electron tomography video for a "type 1" InAs nanowire. It shows the reconstructed 3D shape of a nanowire and its cross sectional slices. The file can be opened with any video player software ("Windows media player" or "VLC" for example). If you face problems to play back the video, the most common issue is the absence of the required video codec. If you operate a MS Windows system, please install the attached "K-Lite Codec Pack" (refer to `http://www.free-codecs.com/download/K_Lite_Codec_Pack.htm`) from the folder "`../05_Codecs`". Otherwise, being an advanced user of an UNIX/ UNIX-like system, you might be able to solve the problem yourself. The video file is courtesy of Christina Möller and Dr. Zi-An Li.

- `tomo_t2.mpg` (full path: "`../01_Electron_tomography/tomo_t2.mpg`") - electron tomography video for a "type 2" InAs nanowire. The video file is courtesy of Christina Möller and Dr. Zi-An Li.

- `tomo_t3.mpg` (full path: "`../01_Electron_tomography/tomo_t3.mpg`") - electron tomography video for a "type 3" InAs nanowire. The video file is courtesy of Christina Möller and Dr. Zi-An Li.

- `2010_12_02_19_17_07.avi` (full path: "`../02_AFM-TEM/2010_12_02_19_17_07.avi`") - video file demonstrating a typical AFM-TEM ex-

periment on in-situ bending of an InAs nanowire. The black and white video in the upper part was captured by the TEM CCD camera. A tip of an AFM cantilever is at the very top, the nanowire attached to a substrate is moving from the bottom to top. The graph at the lower part shows the force, measured with a sensor on the AFM cantilever plotted against the substrate displacement.

- `InAs_02_para.cfg` (full path: "`../03_Atomic_models/InAs_02_para.cfg`") - configuration file containing coordinates of an InAs segment with a para-twin defect. It can be opened using "Notepad" or any similar text editor. The format of the file is described in appendix D. The model can be used for the simulations of HRTEM/STEM micrographs using QSTEM software (see appendix D).

- `InAs_02_para.cmtx` (full path: "`../03_Atomic_models/InAs_02_para.cmtx`") - model visualization file for an InAs segment with a para-twin defect. It can be opened using "Crystal Maker" software. The demo version (for MS Windows and Mac systems) can be found on the same CD.

- `InAs_01_orth.cfg` (full path: "`../03_Atomic_models/orth.cfg`") - configuration file containing coordinates of an InAs segment with a ortho-twin defect.

- `InAs_01_orth.cmtx` (full path: "`../03_Atomic_models/orth.cmtx`") - model visualization file for an InAs segment with a para-twin defect.

- Crystal Maker Demo (full path: "`../04_Crystal_maker`") - contains two folders with distributions of demo versions "Crystal Maker" for Mac OS (in the sub folder "Mac") and for MS Windows (sub folder "Win"). Please refer to `http://www.crystalmaker.com/` for details concerning installation and usage of the software.

- K-Lite Codec pack (full path: "`../05_Codecs/K-Lite_Codec_Pack-880_Standard.exe`") - a codec pack for MS Windows operation systems, which can be installed if you experience problems with play back the video files by running the ".exe" file. For more details please refer to `http://www.free-codecs.com/download/K_Lite_Codec_Pack.htm`.

Appendix C.

Samples and STM tip preparation

C.1. Substrate sample preparation

The InAs nanowire sample for electromechanical characterization (see section 4.3.1) was prepared by cutting an InAs substrate and gluing it onto a copper wire. First, the substrate with as grown InAs nanowires was fixed [1] at a double-sided scotch-tape (with a size of 5 cm x 5 cm) to avoid the pieces of the substrate flying apart during the cutting. A diamond cutter was used to cut a piece of the substrate with a size of approximately 3 mm x 3 mm by scratching and simultaneous pressing the cutter against the substrate. Since the copper wire should be glued to the bottom surface of the substrate, it was mounted with its top surface onto an edge of an adjustable table with double-sided scotch-tape as shown in figure C.1. The procedure should be followed by adjusting the angle of the table and gluing an end of a copper wire (with a diameter of 0.25 mm) to the bottom surface of the substrate with conductive silver epoxy "Chemtronics CW2400" (see figure C.1). After that, the epoxy was dried in air at room temperature for 16 - 24 hours. After the epoxy was dried, the copper wire was cut to a length of 5-6 mm, and the sample was dismounted from the table and stored with the copper wire forced vertically into a foamy material. This geometry allows to avoid contact of the nanowires with any other objects, which is crucial to prevent damage to the nanowires.

C.2. Dielectrophoretic deposition of the nanowires

The deposition of the InAs nanowires on copper electrodes was done by dielectrophoretic deposition and described bellow in a form of a guide. The whole procedure can be divided in three main parts: i)preparation of InAs nanowire solution ; ii) preparation of the copper electrodes; iii) alignment of the electrodes and deposition of the solution.

1. Preparation of InAs nanowire solution.

[1] Since the nanowires grow on the top surface of the substrate, it should be fixed with its bottom surface. The terms "top" and "bottom" surface will be used further in the same meaning.

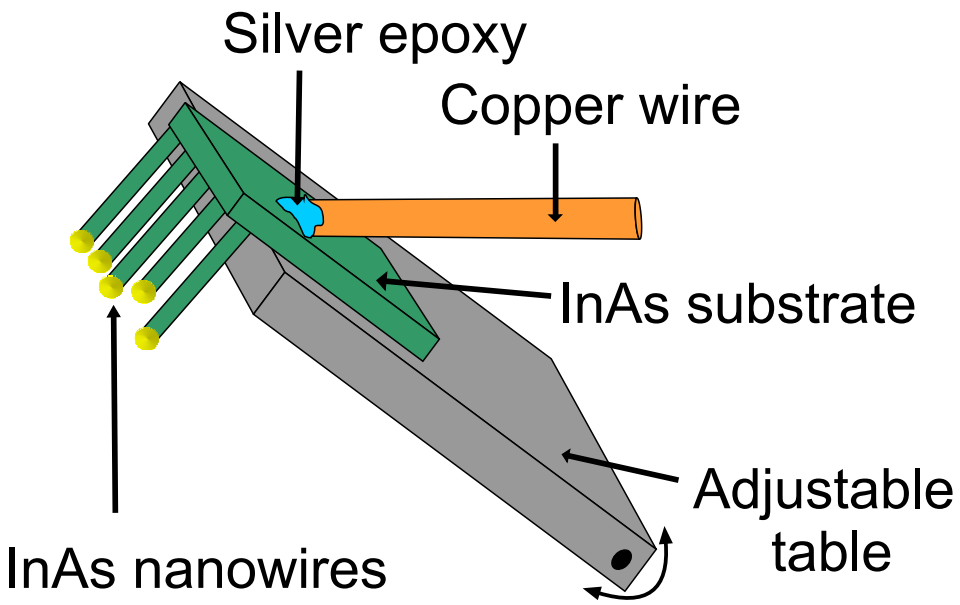

Figure C.1.: Scheme of the preparation of InAs sample on a substrate.

a) Cut a piece of InAs substrate with the nanowires (3 mm x 3 mm) as described in the previous section;

b) Clean the bottom and the side surfaces of the substrate (except the top one with nanowires) using acetone and isopropanol (IPA) or ethanol;

c) Fill a plastic or glass container of total volume of about 5 - 10 ml with 2 ml of a polar solvent (either deionized H_2O or IPA were used);

d) Immerse the container half into an ultrasonic bath;

e) Immerse the top surface of the substrate only into the solvent and switch on the ultrasonication for 3 - 6 seconds;

f) Remove the substrate from the solution, which is now containing the nanowires.

2. Preparation of the copper electrodes for the deposition.

a) Align a copper TEM grid (300 meshes) between two microscope specimen glass plates (with a thickness of 1 - 2 mm) the way that the TEM grid lies in the middle of the bottom plate, and an edge of the top plate is coincident with the cutting directions;

b) Cut the TEM grid with a razor blade bringing it into contact with the side edge of the top glass plate;

c) Repeat cutting in all directions which are shown in the figure C.2 *b*;

d) Chemical polishing of the TEM grid piece can be performed in a solution of H_2O, H_3PO_4 and H_2SO_4 using DC voltage of 1.5 V applied across the TEM grid piece

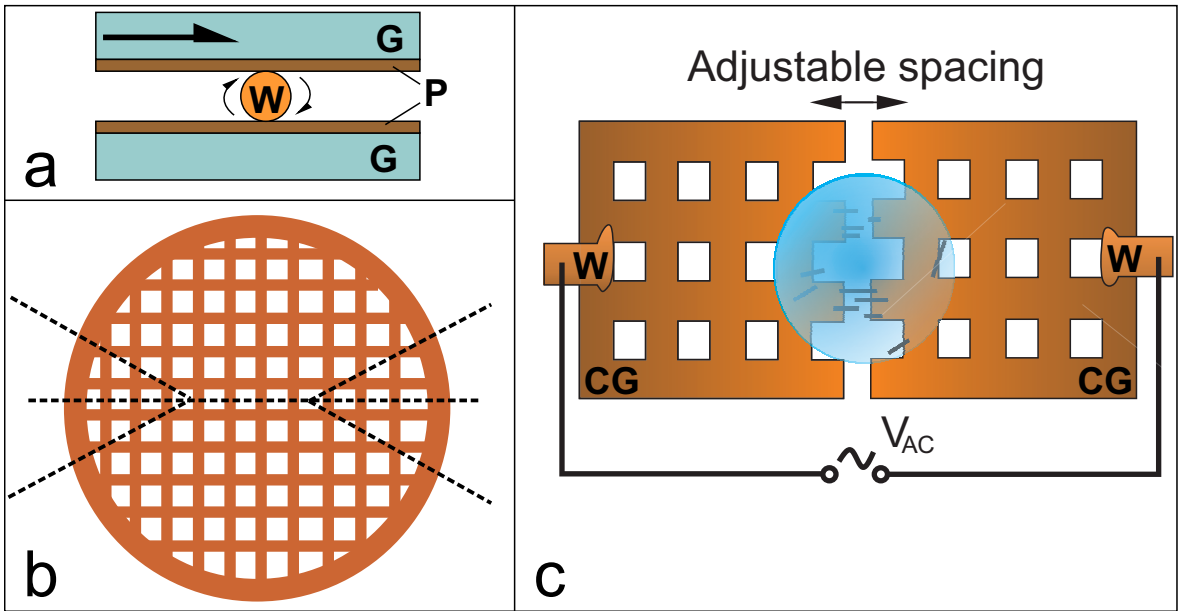

Figure C.2.: (a) Scheme of the wire straightening procedure: *P* - paper, *G* - glass plate, *W* - copper wire. (b) Scheme of cutting of TEM grid. The cutting directions are shown with dashed lines. (c) Scheme of DEP experiment. The figure shows alignment of copper TEM grid electrodes ("grid electrodes"). A drop of solution with the nanowires should be deposited on the middle of the electrodes.

(positive potential) and counter electrode which was settled at the bottom of the glass with the solution. Optimal time for polishing is 10 seconds;

e) The polished TEM grid piece is to be washed in distilled water and dried carefully with a laboratory tissue;

f) Before being glued to the TEM grid pieces the copper wire (0.25 mm in diameter and 8-16 mm length) is to be straightened by rolling it between two microscope specimen glass plates with attached paper to them (see scheme in figure C.2 *a*);

g) Flatten 1 mm of the copper wire using flat pliers;

h) Glue the flat end of the copper wire to the TEM grid piece the way that the wire is parallel to the vertical bars of the TEM grid (see figure C.2 *c*) using conductive silver epoxy and let it drying for 16 - 24 hours. The resulting assembly will be called "grid electrode" in the following text.

3. Alignment of the electrodes and deposition of the nanowires.

a) Two grid electrodes are to be aligned parallel to each other using home built micro-manipulator stages [91] (see figure C.2 *c*), and the distance between the electrodes is to be adjusted to approximately 5 μm;

b) Switch on AC voltage across the grid electrodes with the following parameters: frequency of 1 MHz, peak-to-peak voltage amplitude of 6 V;

c) Deposit a 4 μl drop of the InAs nanowire solution on the middle of the electrodes;

d) Dry the solution with a heat gun at a temperature set to 50 - 70 °C;

e) Switch off the voltage and examine the sample using an optical microscope.

C.3. Preparation of sharp STM tips by electrochemical etching

STM tips were prepared by different methods. Tungsten tip preparation methods which were used in the work are discussed here [79, 132]. The gold tip were prepared by electrochemical etching which procedure discussed bellow in a form of guide.

1. Prepare saturated solution of KCl;
2. Fill a petri cup with the solution;
3. Dip a platinum ring (about 1 cm in diameter) electrode (*E*) into the solution and pull it out to form a thin film of the solution on it (figure C.3 *b*);
4. Attach the electrode to the etching machine[2] (*EM*; figure C.3 *a*);
5. Clamp a gold wire (*GW*) with the diameter of 0.25 mm in the etching machine using screw *S*. The wire should pass through the circular electrode with the solution like it is shown in figure C.3 *b*;
6. Use a cylinder (*C*) with a hole of 0.3 - 0.4 mm in diameter and an adjustable table (*AT*) to insert the bottom end of the gold wire into the hole (figure C.3);
7. The setup is to be adjusted so that: i) the wire end does not reach the bottom of the hole in the cylinder; ii) the length of the wire after it passes through the solution exceeds the depth of the hole; iii) the arm of the etching machine can be moved 3 - 5 mm upwards or downwards without letting the gold wire reach the surface of the cylinder or bottom of the hole with its end;
8. The meniscus, which is formed by the KCl solution on the sides of the gold wire, is to be observed in a medium magnification optical microscope;
9. The etching machine is to be connected to a positive terminal and the platinum electrode is to be connected with the negative terminal;

[2] A setup which allows to clamp vertically a wire (0.25 mm in diameter) on a lever arm with an adjustable height.

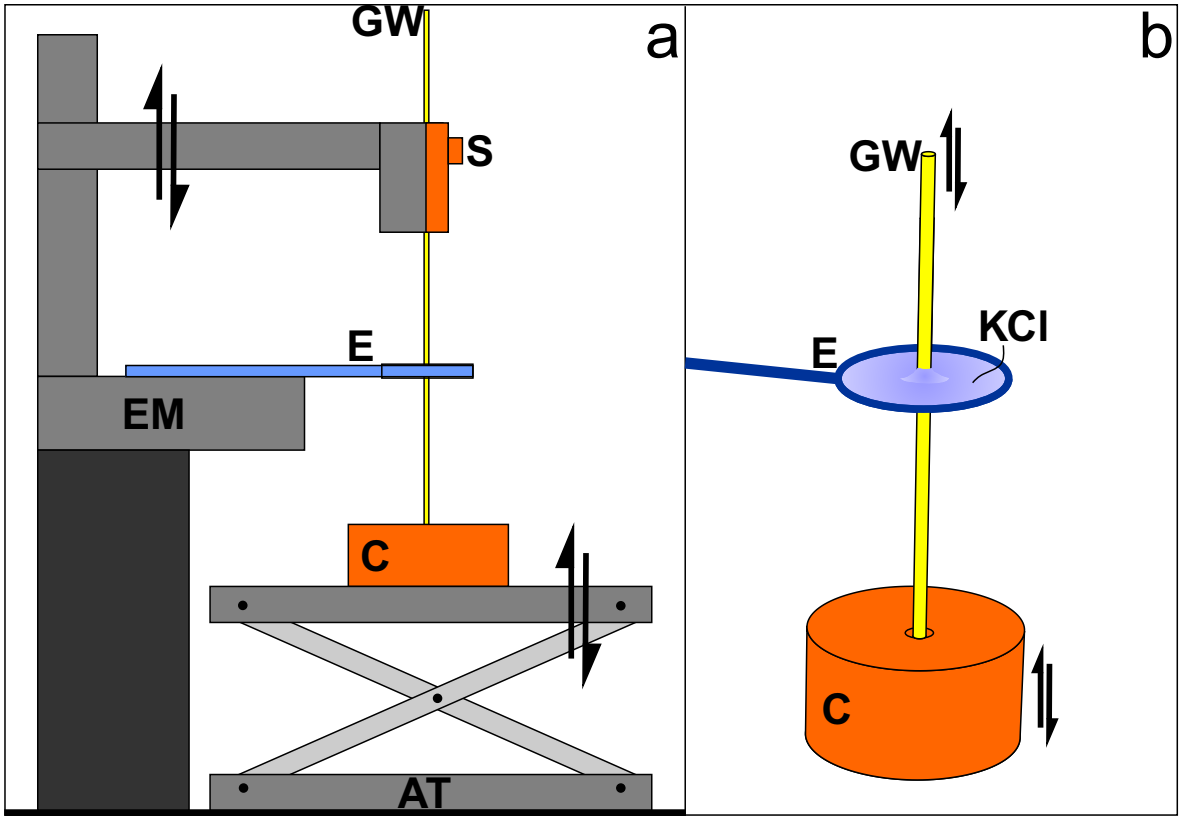

Figure C.3.: (a) Schematic overview of the tip etching procedure. (b) Scheme of electrode/gold wire/-cylinder alignment.

10. To start etching, an AC voltage of 6 V at 6 kHz with a DC offset of 2 V is to be applied between the terminals;

11. The gold wire is to be moved upwards and downwards to optimize the meniscus (to increase its curvature and size);

12. The etching process (i.e thinning of the gold wire in the meniscus region) is to be controlled in the optical microscope;

13. The voltage is to be switched off immediately after the gold wire is cut into two parts, the lower part should fall inside the hole in the cylinder (*C*) depicted in figure C.3 *b*;

14. The upper part of the wire is to be cut under the spot where it is clamped in the etching machine;

15. Both, cut piece and lower part (which fell into the hole) of the gold wire are to be cleaned with distilled water and can be used as tips for the STM setup.

Appendix D.

High resolution transmission electron microscopy image simulations

D.1. Simulations of twin defects

The high resolution TEM images were simulated using QSTEM program. First the atomic models for para- and ortho-twin structures of InAs were built as a the alternating in c-direction layers of closed packed In and As atoms. The layer *A* of In atoms is constructed of hexagonal oriented atoms as it is shown in figure D.1, layer *a* of As atoms (not shown in figure D.1) is above the layer *A*. Layer *B* is another hexagonal layer which is which is situated above the holes between atom of layer *A*, and layer *b* is a corresponding As atomic layer situated above *B*. Layer *C* is a next hexagonal layer which is situated above the holes between atoms of layers *A* and *B*. The corresponding As layer *c* lies above layer *C*.

The para-twin model was constructed from the following layer sequence: "*AaBbCcAaBbCCbBaAcCbB*", in a cubic box with side of 128.4459 Å, containing a total 2723 atoms. The "`InAs_02_para.cfg`" file containing the model information and coordinates of all the

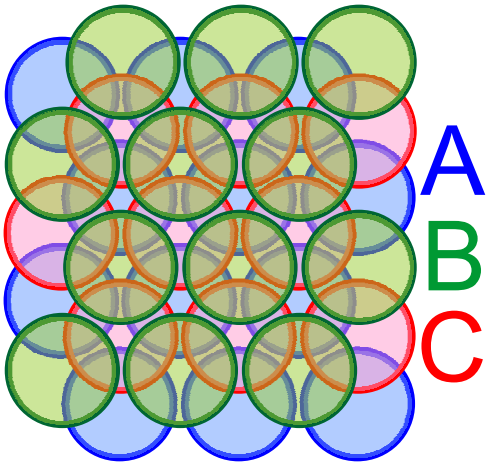

Figure D.1.: Scheme of hexagonal close packing of solid balls, that represent atoms.

atoms is on the CD attached to the thesis. The model can be viewed using ”Crystal Maker” software (demo version on the CD). One should open file ”`InAs_02_para.cmtx`”. The text below shows a part of ”`InAs_02_para.cfg`” file which contains header and relative coordinates of the first layer of In atoms (layer *A*):

```
Number of particles = 2723
A = 1.0 Angstrom (basic length-scale)
H0(1,1) = 128.4459 A
H0(1,2) = 0 A
H0(1,3) = 0 A
H0(2,1) = 0 A
H0(2,2) = 128.4459 A
H0(2,3) = 0 A
H0(3,1) = 0 A
H0(3,2) = 0 A
H0(3,3) = 128.4459 A
.NO_VELOCITY.
entry_count = 3
98
In
0.5 0.5 0.3639
0.5167 0.5289 0.3639
0.4833 0.5289 0.3639
0.4667 0.5 0.3639
0.4833 0.4711 0.3639
0.5167 0.4711 0.3639
0.5333 0.5 0.3639
0.5333 0.5577 0.3639
0.5 0.5577 0.3639
0.4667 0.5577 0.3639
0.45 0.5289 0.3639
0.4333 0.5 0.3639
0.45 0.4711 0.3639
0.4667 0.4423 0.3639
0.5 0.4423 0.3639
0.5333 0.4423 0.3639
0.55 0.4711 0.3639
0.5667 0.5 0.3639
0.55 0.5289 0.3639
0.55 0.5866 0.3639
0.5167 0.5866 0.3639
0.4833 0.5866 0.3639
0.45 0.5866 0.3639
0.4333 0.5577 0.3639
0.4167 0.5289 0.3639
0.4 0.5 0.3639
0.4167 0.4711 0.3639
0.4333 0.4423 0.3639
0.45 0.4134 0.3639
0.4833 0.4134 0.3639
0.5167 0.4134 0.3639
0.55 0.4134 0.3639
0.5667 0.4423 0.3639
0.5833 0.4711 0.3639
0.6 0.5 0.3639
0.5833 0.5289 0.3639
0.5667 0.5577 0.3639
0.4167 0.5866 0.3639
0.4 0.5577 0.3639
0.3833 0.5289 0.3639
0.3667 0.5 0.3639
0.3833 0.4711 0.3639
0.4 0.4423 0.3639
0.4167 0.4134 0.3639
0.5833 0.4134 0.3639
0.6 0.4423 0.3639
0.6167 0.4711 0.3639
0.6333 0.5 0.3639
0.6167 0.5289 0.3639
0.6 0.5577 0.3639
0.5833 0.5866 0.3639
0.3833 0.5866 0.3639
0.3667 0.5577 0.3639
0.35 0.5289 0.3639
0.3333 0.5 0.3639
0.35 0.4711 0.3639
0.3667 0.4423 0.3639
0.3833 0.4134 0.3639
0.6167 0.4134 0.3639
0.6333 0.4423 0.3639
0.65 0.4711 0.3639
0.6667 0.5 0.3639
0.65 0.5289 0.3639
0.6333 0.5577 0.3639
0.6167 0.5866 0.3639
0.35 0.5866 0.3639
0.3333 0.5577 0.3639
0.3167 0.5289 0.3639
0.3 0.5 0.3639
0.3167 0.4711 0.3639
0.3333 0.4423 0.3639
0.35 0.4134 0.3639
0.65 0.4134 0.3639
0.6667 0.4423 0.3639
0.6833 0.4711 0.3639
0.7 0.5 0.3639
0.6833 0.5289 0.3639
0.6667 0.5577 0.3639
0.65 0.5866 0.3639
0.3167 0.5866 0.3639
0.3 0.5577 0.3639
0.2833 0.5289 0.3639
0.2667 0.5 0.3639
0.2833 0.4711 0.3639
0.3 0.4423 0.3639
0.3167 0.4134 0.3639
0.6833 0.4134 0.3639
0.7 0.4423 0.3639
0.7167 0.4711 0.3639
0.7333 0.5 0.3639
0.7167 0.5289 0.3639
0.7 0.5577 0.3639
0.6833 0.5866 0.3639
0.2833 0.5866 0.3639
0.2667 0.5577 0.3639
0.25 0.5289 0.3639
0.2333 0.5 0.3639
0.25 0.4711 0.3639
0.2667 0.4423 0.3639
0.2833 0.4134 0.3639
0.7167 0.4134 0.3639
0.7333 0.4423 0.3639
0.75 0.4711 0.3639
0.7667 0.5 0.3639
0.75 0.5289 0.3639
0.7333 0.5577 0.3639
0.7167 0.5866 0.3639
0.25 0.5866 0.3639
0.2333 0.5577 0.3639
0.2167 0.5289 0.3639
0.2 0.5 0.3639
0.2167 0.4711 0.3639
0.2333 0.4423 0.3639
0.25 0.4134 0.3639
0.75 0.4134 0.3639
0.7667 0.4423 0.3639
0.7833 0.4711 0.3639
0.8 0.5 0.3639
0.7833 0.5289 0.3639
0.7667 0.5577 0.3639
0.75 0.5866 0.3639
0.2167 0.5866 0.3639
0.2 0.5577 0.3639
0.1833 0.5289 0.3639
0.1667 0.5 0.3639
0.1833 0.4711 0.3639
0.2 0.4423 0.3639
0.2167 0.4134 0.3639
0.7833 0.4134 0.3639
0.8 0.4423 0.3639
0.8167 0.4711 0.3639
0.8333 0.5 0.3639
0.8167 0.5289 0.3639
0.8 0.5577 0.3639
0.7833 0.5866 0.3639
0.1833 0.5866 0.3639
0.1667 0.5577 0.3639
0.1667 0.4423 0.3639
0.1833 0.4134 0.3639
0.8167 0.4134 0.3639
0.8333 0.4423 0.3639
0.8333 0.5577 0.3639
0.8167 0.5866 0.3639
```

The first line defines the number of atoms in a model. The second line states which units are used for the size of the simulation box. The lines 3 - 11 set the simulation box size and geometry. Line 13 states how many entries are used to define an atom: ”3” means that an atom is defined only by its coordinates. Line 14 and 15 contain Z-number and the name of the element, respectively. The following lines contain tab separated values of the relative atomic coordinates of the atoms of the type as stated in lines 14 and 15. Further details of ”.cfg” file structure for

"QSTEM" can be found elsewhere [88, 133].

The ortho-twin model was constructed from the the following layer sequence: "*AbBcCaAbBcCaAbBcCbBaAbBaAbB*", in a square box with size of 128.4459 Å. Total amount of atoms in the model is equal to 3644, the "`InAs_01_orth.cfg`" file containing the model information and coordinates of all the atoms is on a CD attached to the thesis. The model can be viewed in "Crystal Maker" software by opening a file "`InAs_01_orth.cmtx`".

Both models were used to simulate the propagating through the sample planar electron wave (and consequently HRTEM micrograph) of a TEM by QSTEM software [88]. Figure D.2 shows screen shot of the software window which shows the parameters used for the simulations. The parameters were set close to the parameters of the Tecnai F20 microscope which was used for experimental investigation of the InAs nanowires. Among them are: array size, which determines image size; high voltage is the acceleration voltage of the microscope (200 kV); spherical aberration. Another important parameter is slice thickness. The slice thickness should be set to a value which does not exceed the lattice spacing in the direction of the electron beam, since multislice algorithm, implemented in "QSTEM" software, based on calculation of the electron wave function after each slice. The "QSTEM" returns an output of 8 ".img" files that contain complex wave of the electrons. The last file, which contains the wave after the electron passed through the simulation box, was used to simulate HR-TEM images in "imageSim" software which is a part of "QSTEM".

The parameters for the TEM image simulations were chosen according to the values of the experimental parameters (see screen shot of "imageSim" window in figure D.3). By setting the defocus step and images values to 10 nm and 10 respectively one can achieve a focus series of 10 HR-TEM images with focus differences of 10 nm between them.

Figure D.4 shows a focal series of TEM images. The differences between the images (for any given defocus) are obvious. The lattice distortion in the stacked region could not included in the atomic model. This can lead to significant difference between simulated images and the experimental ones.

D.2. Simulations of bended nanowires

The simulations of HRTEM images and diffraction patterns of bended nanowire was done using the "QSTEM" software. The atomic models were build by transformation (bending) of a "parent" model. The parent model was constructed from the the following layer sequence in the z-direction: "*AaBbCcAaBbCcAaBbCcAaBbAaBbAaBbAaBbAaBb*". The growth direction of the wire is aligned along the x-direction of the box which corresponds to the $\langle 112 \rangle$ crystallographic direction. Therefore, the plains of stacking faults are parallel to the growth direction. Half of the nanowires has Zinc Blende structure and the other half has Wurtzite structure. The

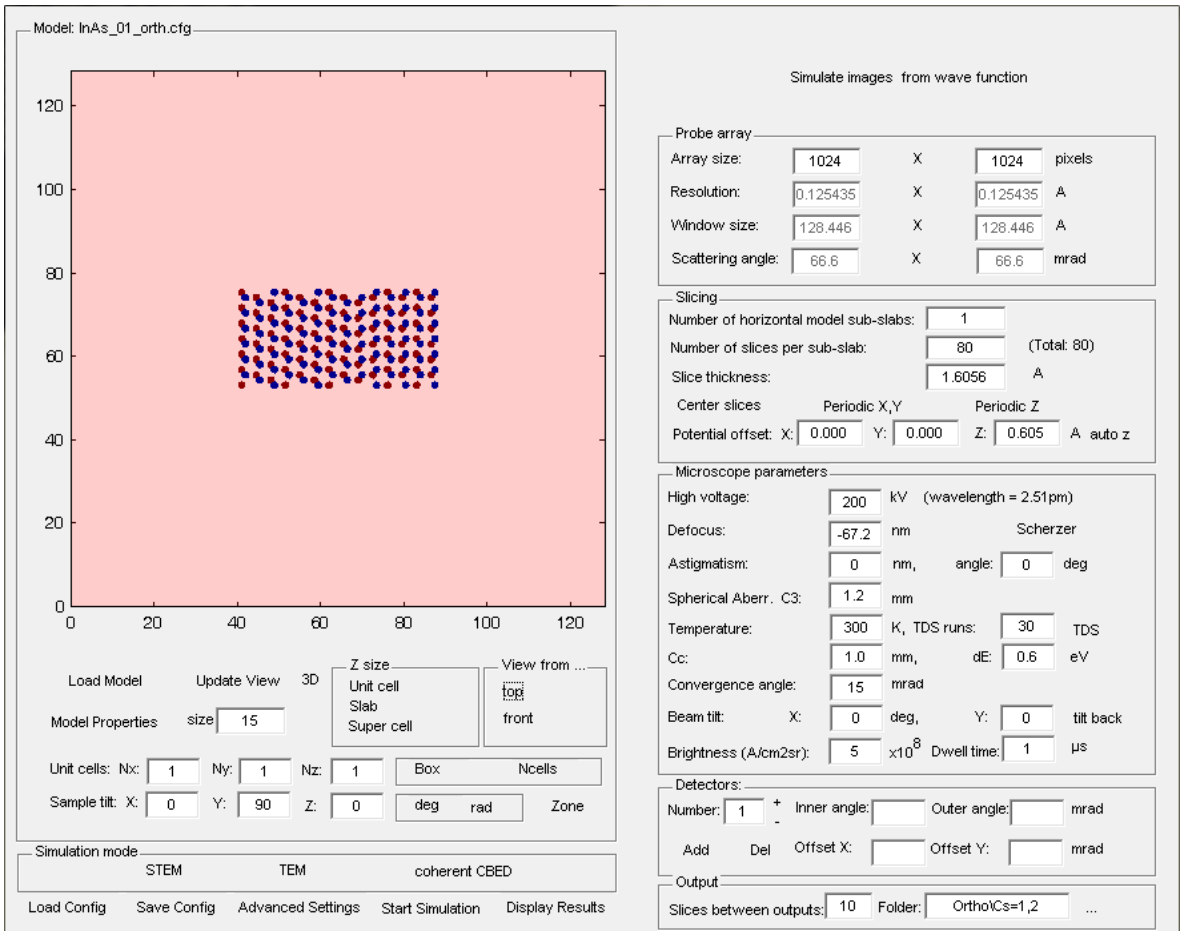

Figure D.2.: Screen shot of "QSTEM" software window. The image at the top left of the window shows a top view of an atomic model used for the simulation. The parameters used for the simulation are given in boxes at the bottom and on the right hand side.

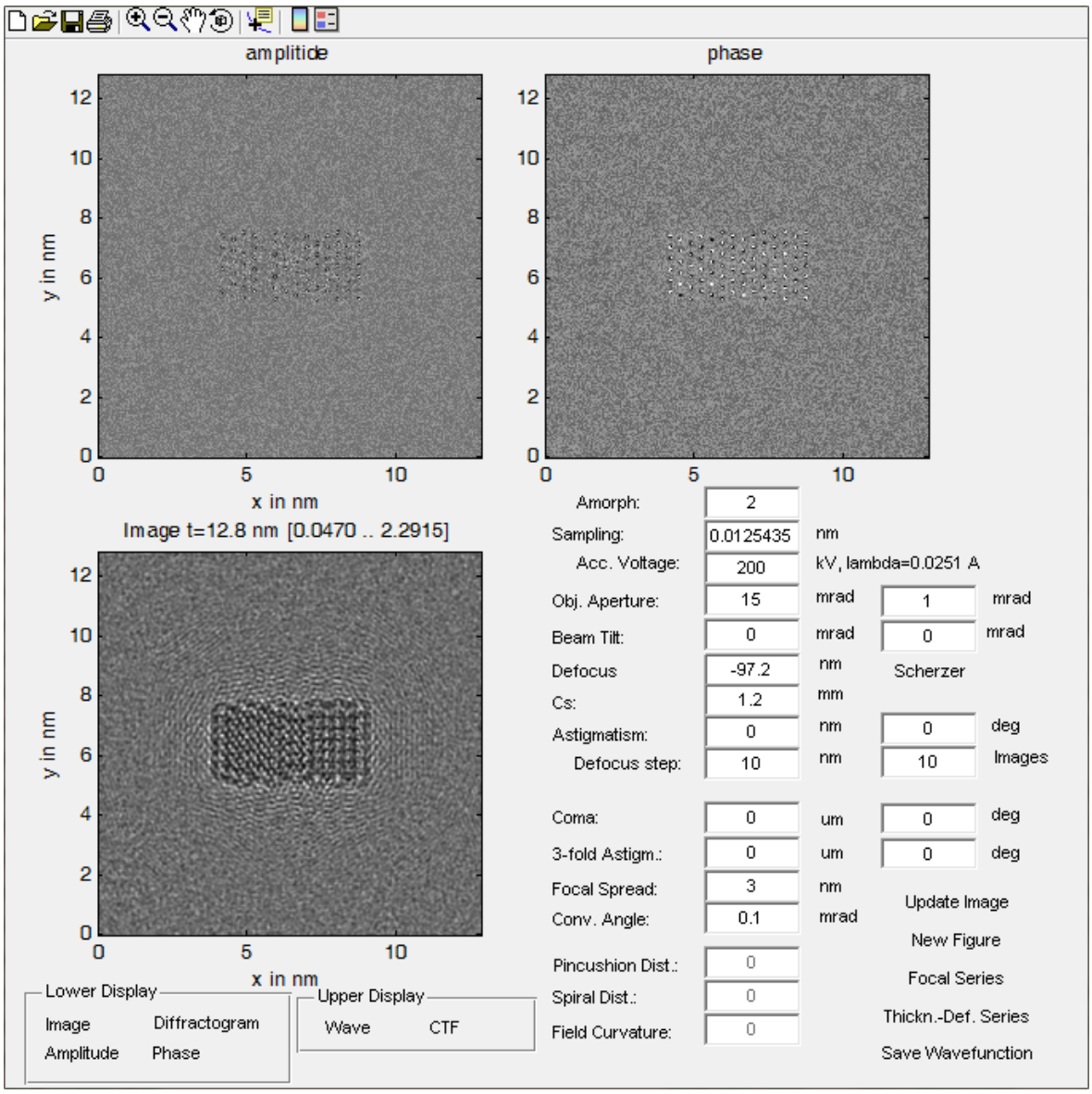

Figure D.3.: Screen shot of "imageSim" software window. The upper left image shows the amplitude of the selected complex electron wave, the upper right image shows the phase, the lower image shows the resulting TEM micrograph, which contains both the amplitude and the phase. The parameters used for the simulations are shown in the white boxes.

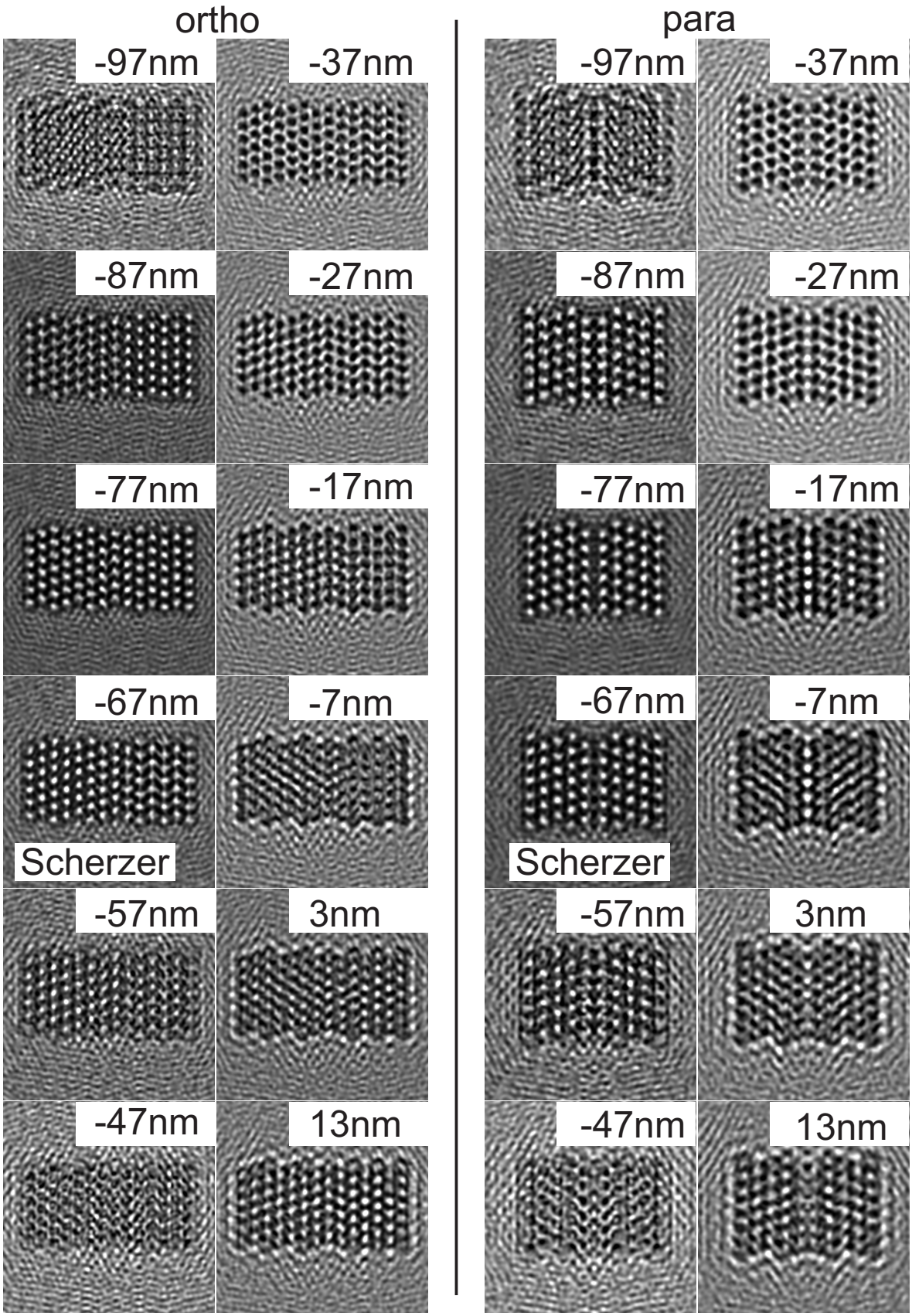

Figure D.4.: Simulated focus series of TEM micrographs of ortho- (left) and para-twin (right). The defocus values are given on each image.

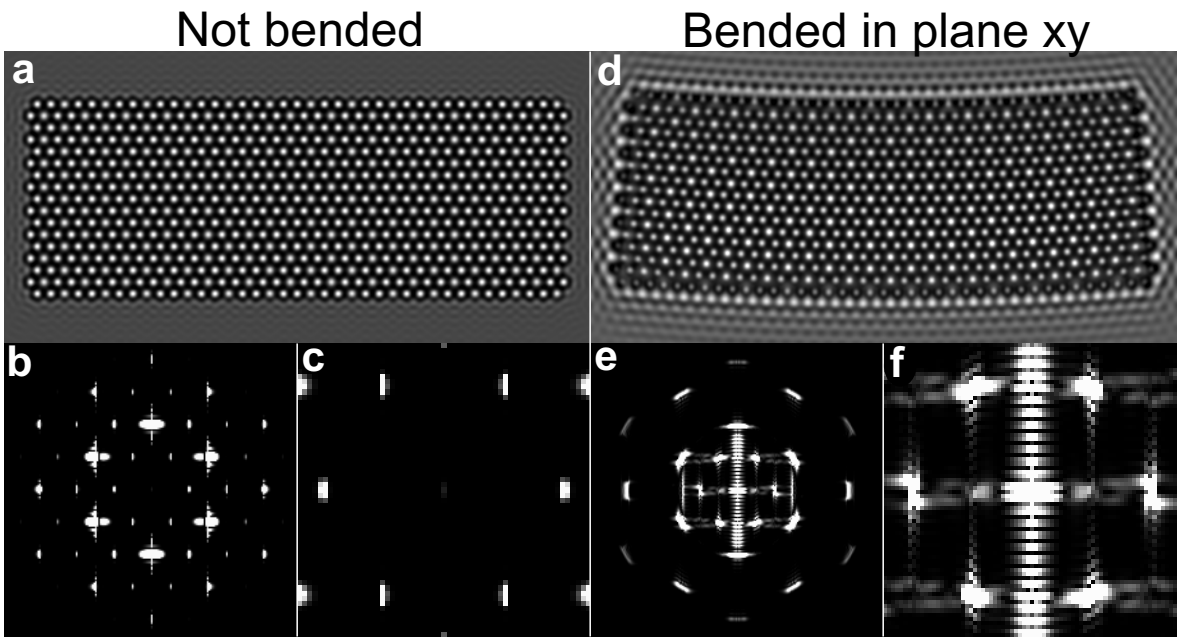

Figure D.5.: (a) Simulated TEM micrograph of a part of a non-deformed InAs nanowire viewed along the ⟨111⟩. (b) The corresponding filtered FFT pattern. (c) The magnified first order (central) reflexes of the FFT pattern (b). (d) Simulated TEM micrograph of a part of an InAs nanowire which is bended in (xy) plane. (e) The corresponding filtered FFT pattern. (f) The magnified first order reflexes of the FFT pattern (e).

parent model was bent in plane (xy) (figure D.5 *d-f*), in planes which have angle of $\pi/12$ (figure D.6 *a-c*), $\pi/6$ (figure D.6 *d-f*), $\pi/4$ (figure D.7 *a-c*) and $\pi/3$ (figure D.7 *d-f*), and in plane (xz) (figure D.8). The bending of the models was performed by assigning interpolated coordinate displacements to the atoms of the parent model. The curvature radius is equal to 500 nm as in the experiment. The model was aligned with z-axis (⟨111⟩ direction) parallel to the electron beam. The TEM images were simulated as it was discussed in section D.1. Since the HR-TEM simulations were performed only to obtain FFT images subsequently, the simulation parameters are not similar to the experimental ones. The spherical aberration was set to 0.01 mm, the defocus to -6.1 nm (Scherzer defocus), the other parameters have the same values as listed in figure D.2. The simulated electron wave which passed only few nanometers of the sample was then used to simulate HR-TEM images using the ”imageSim” software. The parameters for HR-TEM image simulations were adopted from electron wave simulation. The simulated HR-TEM micrographs were processed by FFT or FFT with Hanning filter.

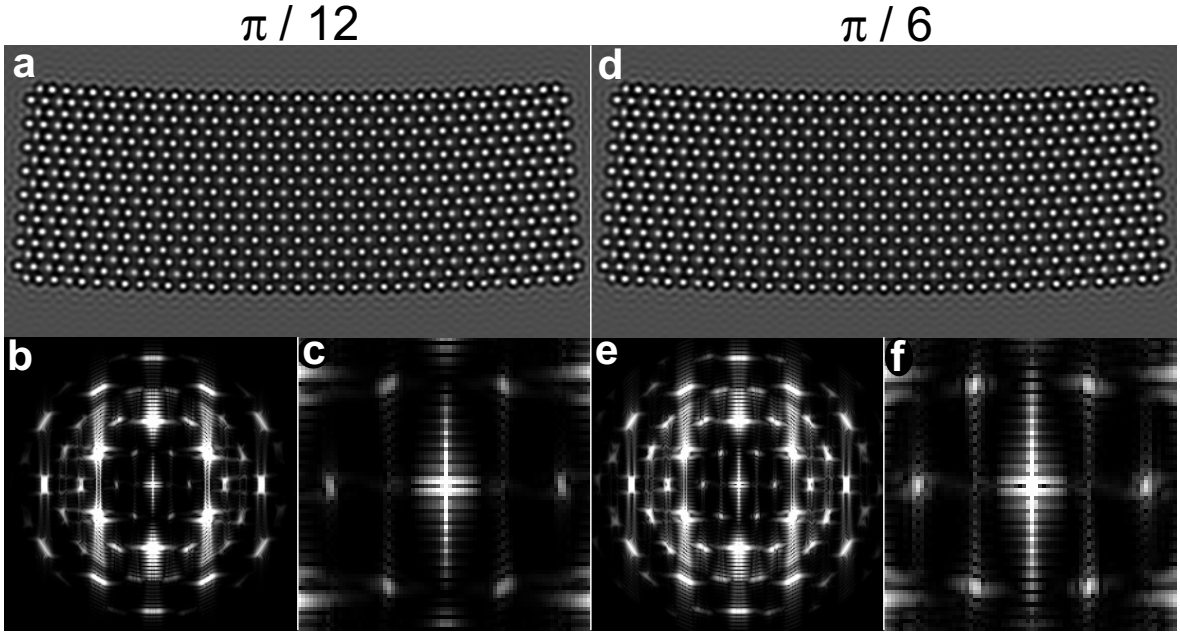

Figure D.6.: (a) Simulated TEM micrograph of a part of an InAs nanowire which is bended in plane inclined at an angle $\pi/12$ to the (xy) plane. (b) The corresponding filtered FFT pattern. (c) The magnified first order reflexes of the FFT pattern (b). (d) Simulated TEM micrograph of a part of an InAs nanowire which is bended in plane inclined at an angle $\pi/6$ to the (xy) plane. (e) The corresponding filtered FFT pattern. (f) The magnified first order reflexes of the FFT pattern (e).

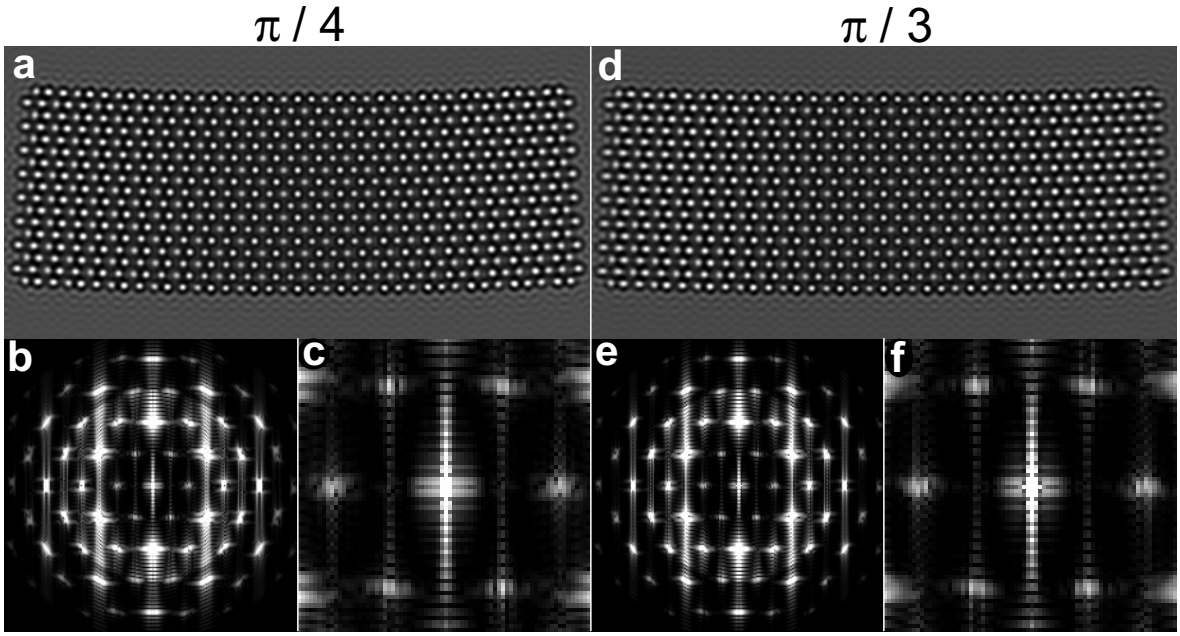

Figure D.7.: (a) Simulated TEM micrograph of a part of an InAs nanowire which is bended in plane inclined at an angle $\pi/4$ to the (xy) plane. (b) The corresponding filtered FFT pattern. (c) The magnified first order reflexes of the FFT pattern (b). (d) Simulated TEM micrograph of a part of an InAs nanowire which is bended in plane inclined at an angle $\pi/3$ to the (xy) plane. (e) The corresponding filtered FFT pattern. (f) The magnified first order reflexes of the FFT pattern (e).

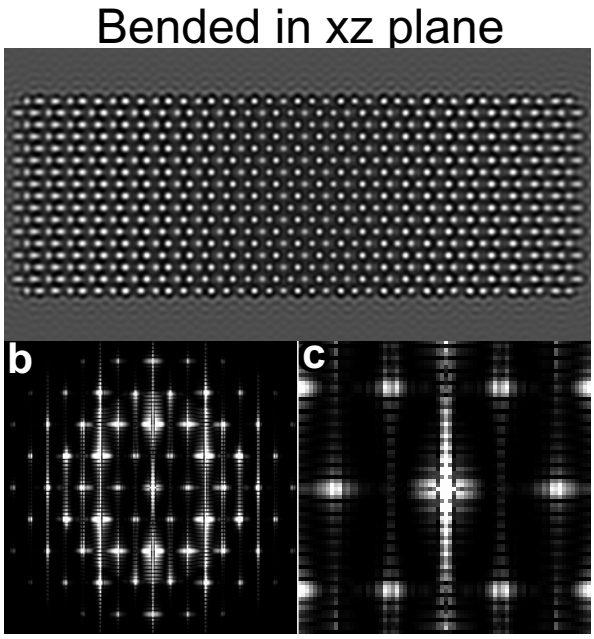

Figure D.8.: (a) Simulated TEM micrograph of a part of an InAs nanowire which is bended in (xz) plane. (b) The corresponding filtered FFT pattern. (c) The magnified first order reflexes of the FFT pattern (b).

Appendix E.

Bending technique: Implementation and data analysis

The principal scheme of the bending experiment is shown in figure E.1. The nanowires, sticking out from the bars of a TEM grid, are to be brought into contact with the cantilever tip. The whole system (AFM tip and the nanowire) is to be simultaneously observed (in focus) in TEM. The substrate with the nanowires is pushed against the cantilever in a controlled way (”Nanofactory Control” software). Force-displacement (F-d) plots are recorded automatically. The parameters used for the testing are listed in table E.1. Simultaneously a video is recorded with TEM camera (synchronized with the F-d plot). The example of such a force-displacement test is shown in video file ”`2010_12_02_19_17_07.avi`”.

After video recording the F-d plot must be corrected to eliminate the effect of a discharge current on the readout of the AFM sensor. This is necessary , since the AFM sensor is charged during the experiment [90, 91]. The discharge current gives rise to the overall signal which is converted into force. The additional signal is approximated as linear in time. Since in the beginning and in the end of the experiment the nanowire is not in contact with the AFM tip,

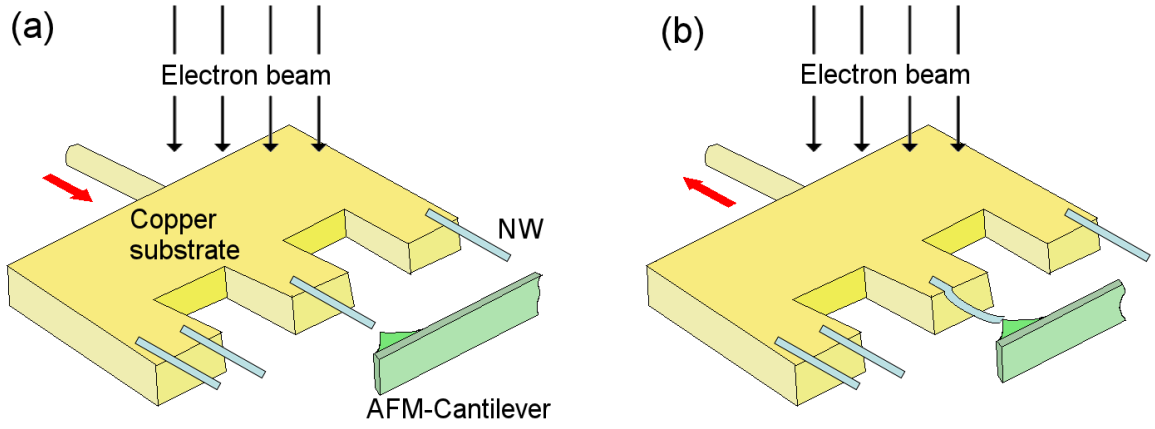

Figure E.1.: Scheme of the bending experiment. a) Approach of a nanowire to the AFM cantilever. b) Bending of the nanowire and its subsequent retraction. The image is adopted from [91].

Table E.1.: Parameters for acquisition of F-d plots.

Parameter	Value (units)	Description
Start	-50 - 0 (nm)	Relative start position of the sample. The position of the sample will be changed by this value before the experiment. If the nanowire is initially in contact with the AFM tip, the value should be set to a negative value to move the sample backwards to rip contact of the nanowire and AFM tip. If the nanowire is initially separated from the tip, this value can be set to 0.
End	50 - 500 (nm)	Relative end position of the sample. This parameter determines overall displacement of the sample towards the AFM tip.
Dual Slope	Yes	When it is set to ”Yes” the sample will be moved first to the start position, than to the end position and to the start position back. This assures that force displacement curves are recorded in forward and backward direction.
Acquisition time	3000 - 30000 (ms)	Is a total acquisition time for the F-d plot.
Samples	1600 - 3200	Is the amount of the data points of that the F-d plot consists of.
Relative	Yes	By selecting ”Yes” the initial and stop positions of the sample will be calculated relative to the current position.
Soft Reset	Yes / No	By selecting ”Yes” the sample will be set after the experiment to the same position as before the experiment. By selecting ”No” the sample will remain the end position of the experiment.

the force in these moments should be equal to zero. The difference between force reading at the moment t=0 (experiment start) and at the moment t=t_{end} (experiment end) is ΔF, which is related to the parasitic signal $F_p(t)$ in the following way:

$$F_p(t) = \frac{\Delta F t}{t_{end}} \tag{E.1}$$

The signal $F_p(t)$ is extracted from the force displacement plots.

To calculate Young's modulus from the bending experiment the distance between the nanowire end and the source should be measured before the experiment l_0 and during the experiment at maximal displacement l' of the substrate. The total deformation of the nanowire $\Delta l = l_0 - l'$ and maximal force F_{max}, which corresponds to a maximal substrate displacement, can be used to calculate Young's modulus of the nanowire [91]:

$$E = \frac{2R^3 F_{max}}{I l_0}, \tag{E.2}$$

where R is bending radius, I is second moment of inertia. Approximating the bending radius with a circle sector the following formula can be used for numerical calculations of R [91]:

$$R = \frac{l'}{2sin\frac{l_0}{2R}}. \tag{E.3}$$

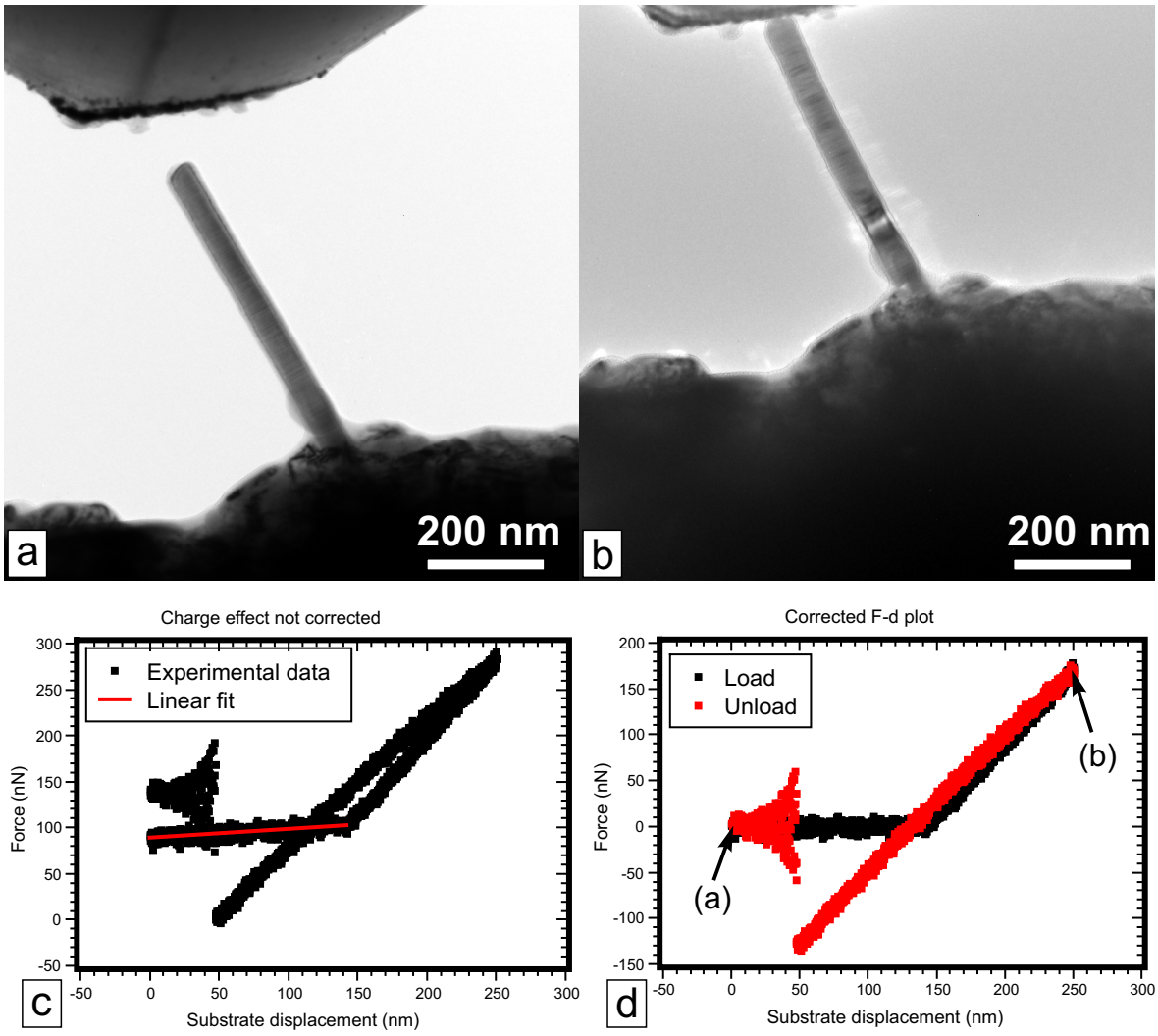

Figure E.2.: Illustration of the experiment on bending of a nanowire. a) TEM micrograph of a nanowire before bending. b) TEM micrograph of the nanowire under maximal load. c) Raw F-d plot. d) Corrected F-d plot. Points (a) and (b) on the graph correspond to the micrographs. The figures are adopted from [91].

Appendix F.

Surface of InAs nanowires

The {112} side wall facets have been found in InAs nanowires with ⟨111⟩ growth direction (see section 5.1.3). However, the precise atomic structure can not be studied using TEM. In the table below different possibilities of facet formation are considered, and the properties of the facets are described. The sketches show a bulk truncated atomic structure of the facets which is viewed from the side along ⟨110⟩ direction. Green balls correspond to In atoms (cations) and purple balls correspond to As atoms (anions). Dangling bonds (DB) of the surface atoms are shown with blue ellipses.

In general to predict theoretically the surface structure the free energy should be minimized [137]. For the most of the surfaces multiple minima can occur. The selection of one or another minima depends strongly on the preparation method [138]. In the case of the epitaxially grown nanowires the precursor fluxes may have a significant impact. However, some general rules (”principles”) of surface reconstruction which are proposed by Duke [138] can be formulated for tetrahedrally coordinated compound semiconductors as InAs:

1. **The surface structure should have a free-energy corresponding to one of the free-energy minimas accessible under the preparation conditions.**

2. **Surface tends to be autocompensated or to compensate space charge bellow it.**
   This principle restricts the stoichiometry of a surface that no electrical charge is accumulated. For the InAs nanowires, which has a two dimensional electron gas at the surface, the surface will be expected to form such a structure that the space charge bellow the surface is compensated.

3. **The surface reconstruction should lead to the structure which lower the surface electron states associated with dangling bonds and surface bonds.**
   Ideally this principle can be applied by calculating of the electronic surface state energies and comparison with the experimental spectra. Qualitatively, the predicted surface structure should be restricted by the following: (i) the valences of both cation (In) and anion (As) should be saturated; (ii) the structure should obey electron counting rule (ECR)[139].

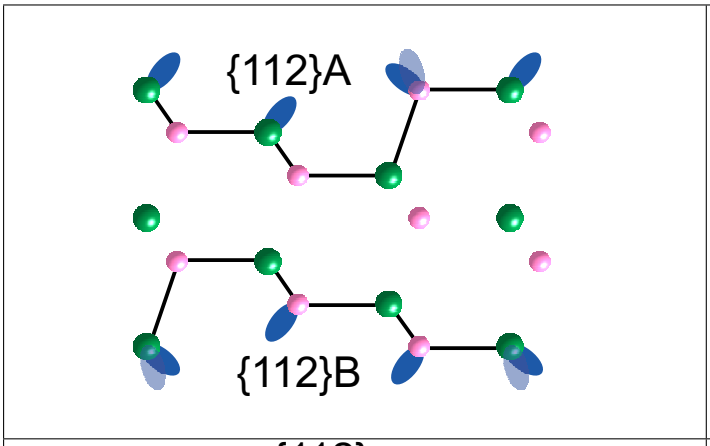

Zinc Blende {112} surface.
- High(≈ 2.5 Å) atomic steps;
- partially polar [116];
- twin defect changes polarity of the surface;
- 2 In atoms per unit cell with one DB per atom (for In terminated surface);
- 1 As atom with two DB;
- no stable reconstruction was found in GaAs [116].

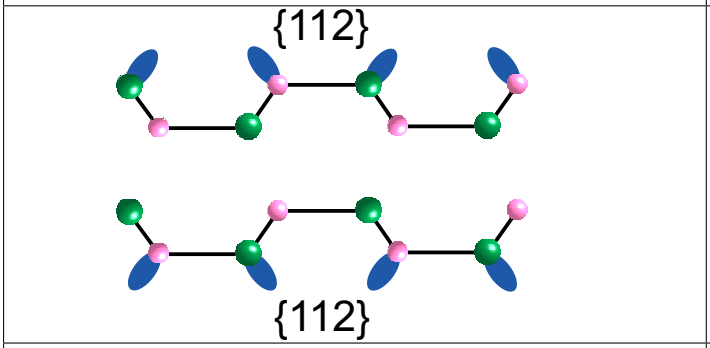

Wurtzite {112} ({10-10}) surface.
- Small (≈ 1.2 Å) atomic steps;
- not polar;
- 1 In and 1 As atom per unit cell with one DB per atom;
- no reconstruction was found in InAs nanowires [134].

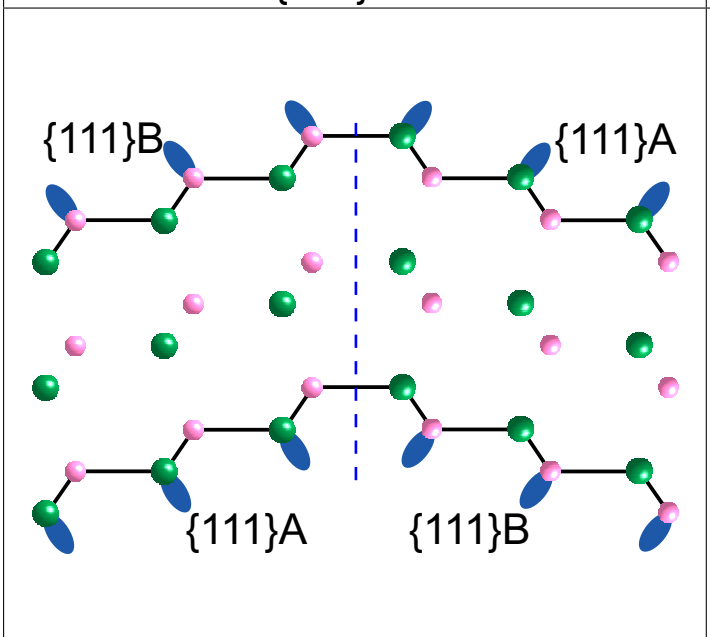

Zinc Blende {111} surface.
- Can form only in twinned nanowires, has zig-zag structure;
- smallest (≈ 0.9 Å) atomic steps;
- fully polar;
- twin defect changes the polarity of the surface;
- 1 As (or In) atom per unit cell with one DB per atom;
- (2 x 2) In vacancy structure is the most stable reconstruction of InAs {111}A surface [135];
- InAs {111}B surface possesses (2 x 2) As trimer reconstruction in As reach conditions [136].

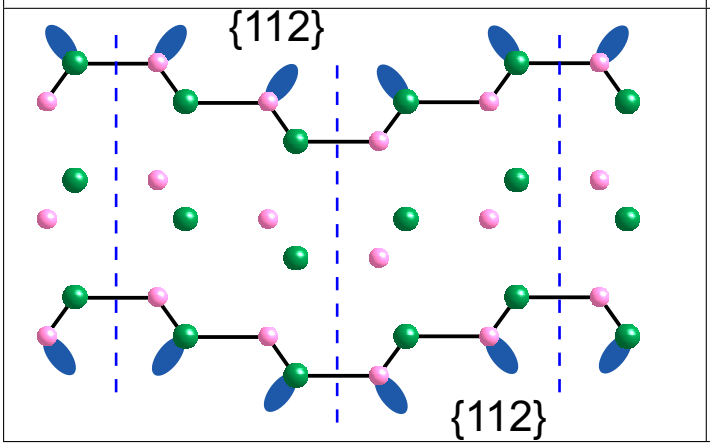

Multi-twin (4H) {112} surface.
- Small (≈ 1.2 Å) atomic steps;
- not polar;
- similar to ZB {111} surface;
- 2 In and 2 As atoms per unit cell with one DB per atom.

The rule states that the dangling bonds of cation should be empty, whereas the anion ones should be filled.

Among the surfaces, that considered in the table, {111} surfaces has the lowest free energy, and its formation is believed to be one of the driving forces for the formation of the twin structures [105, 140]. Moreover, our HR-TEM micrographs suggest the formation of zig-zag structure at the surface (figure 5.4), which is an evidence of the {111}-type facets. According to the facts listed in the table the most stable reconstructions of {111}A and {111}B surfaces are (2 x 2) In vacancy and As trimer structures respectively [135, 136]. However, the multitwin structure or nanowire segments with the high defect density (each 3-5 atomic layers) can satisfy the principles formulated above without reconstruction. The twinned morphology allow the charge transfer from a cation dangling bond (3/4 electrons) to an anion dangling bond (5/4 electrons). This rearrangement of local electron densities satisfies electron counting rule and, therefore, leads to the lowering of the surface states. This suggest that unrelaxed InAs{111} - (1 x 1) structure is also possible in the nanowires. Both reconstructed and unreconstructed surface structures affect elastic moduli only in the top 2-3 layers. For a nanowire with diameter of 30 nm the surface layer will correspond to the volume of approximately 6% of the nanowire. The change in the total Young's modulus, therfore, can not be expected greater than 5%. This findings support the statement regarding the negligeble impact of the surface made in the section 5.2. Presize knowladge of the surface structure, which can be determined experimentaly, will be helpfull to calculate the exact impact of the surface on elastic properties of the nanowires.

References

[1] Y. Wu, Y. Cui, L. Huynh, C. J. Barrelet, D. C. Bell, and C. M. Lieber. "Controlled Growth and Structures of Molecular-Scale Silicon Nanowires". In: *Nano Lett.* 4.3 (2004), pp. 433–436. DOI: 10.1021/nl035162i.

[2] J. Caram, C. Sandoval, M. Tirado, D. Comedi, J. Czaban, D. A. Thompson, and R. R. LaPierre. "Electrical characteristics of core-shell p-n GaAs nanowire structures with Te as the n-dopant". In: *Nanotechnology* 21.13 (2010), p. 134007. DOI: 10.1088/0957-4484/21/13/134007.

[3] K. Tomioka, J. Motohisa, S. Hara, K. Hiruma, and T. Fukui. "GaAs/AlGaAs Core Multishell Nanowire-Based Light-Emitting Diodes on Si". In: *Nano Lett.* 10.5 (2010), pp. 1639–1644. DOI: 10.1021/nl9041774.

[4] M. Ek, B. M. Borg, A. W. Dey, B. Ganjipour, C. Thelander, L.-E. Wernersson, and K. A. Dick. "Formation of the Axial Heterojunction in GaSb/InAs(Sb) Nanowires with High Crystal Quality". In: *Cryst. Growth Des.* 11.10 (2011), pp. 4588–4593. DOI: 10.1021/cg200829q.

[5] Ch. Gutsche, R. Niepelt, M. Gnauck, A. Lysov, W. Prost, C. Ronning, and F.-J. Tegude. "Direct Determination of Minority Carrier Diffusion Lengths at Axial GaAs Nanowire p-n Junctions". In: *Nano Lett.* 12.3 (2012), pp. 1453–1458. DOI: 10.1021/nl204126n.

[6] K. Tomioka, J. Motohisa, S. Hara, and T. Fukui. "Control of InAs Nanowire Growth Directions on Si". In: *Nano Lett.* 8.10 (2008), pp. 3475–3480. DOI: 10.1021/nl802398j.

[7] K. A. Dick, K. Deppert, L. S. Karlsson, W. Seifert, L. R. Wallenberg, and L. Samuelson. "Position-Controlled Interconnected InAs Nanowire Networks". In: *Nano Lett.* 6.12 (2006), pp. 2842–2847. DOI: 10.1021/nl062035o.

[8] H. J. Joyce, Q. Gao, H. H. Tan, C. Jagadish, Y. Kim, X. Zhang, Y. Guo, and J. Zou. "Twin-Free Uniform Epitaxial GaAs Nanowires Grown by a Two-Temperature Process". In: *Nano Lett.* 7.4 (2007), pp. 921–926. DOI: 10.1021/nl062755v.

[9] K. A. Dick, C. Thelander, L. Samuelson, and P. Caroff. "Crystal Phase Engineering in Single InAs Nanowires". In: *Nano Lett.* 10.9 (2010), pp. 3494–3499. DOI: 10.1021/nl101632a.

[10] E.P.A.M. Bakkers, R. Algra, M. Hocevar, M.T. Borgstrom, G. Immink, B. Ketelaars, L. Feiner, W.J.P. van Enckevort, E. Vlieg, and M.A. Verheijen. "Periodic nanowire structures". In: *Optoelectronic and Microelectronic Materials and Devices (COMMAD), 2010 Conference on*. 2010, pp. 33 –34. DOI: 10.1109/COMMAD.2010.5699764.

[11] Q.-T. Do, K. Blekker, I. Regolin, W. Prost, and F. J. Tegude. "High Transconductance MISFET With a Single InAs Nanowire Channel". In: *IEEE Electron Device Lett.* 28 (2007), pp. 682–684. DOI: 10.1109/LED.2007.902082.

[12] Shadi A Dayeh. "Electron transport in indium arsenide nanowires". In: *Semicond. Sci. Technol.* 25.2 (2010), p. 024004. DOI: 10.1088/0268-1242/25/2/024004.

[13] J. Salfi, I.G. Savelyev, M. Blumin, S.V. Nair, and H.E. Ruda. "Direct observation of single-charge-detection capability of nanowire field-effect transistors". In: *Nat. Nanotechnol.* 5.10 (2010), pp. 737–741. DOI: 10.1038/NNANO.2010.180.

[14] Y. Dong, G. Yu, M. C. McAlpine, W. Lu, and C. M. Lieber. "Si/a-Si Core/Shell Nanowires as Nonvolatile Crossbar Switches". In: *Nano Lett.* 8.2 (2008), pp. 386–391. DOI: 10.1021/nl073224p.

[15] H.S. Yan H.and Choe, S. Nam, Y. Hu, S. Das, J.F. Klemic, J.C. Ellenbogen, and C.M. Lieber. "Programmable nanowire circuits for nanoprocessors". In: *Nature* 470.7333 (2011), pp. 240–244. DOI: 10.1038/nature09749.

[16] J. Tang, Z. Huo, S. Brittman, H. Gao, and P. Yang. "Solution-processed core-shell nanowires for efficient photovoltaic cells". In: *Nat. Nanotechnol.* 6.9 (2011), pp. 568–572. DOI: 10.1038/nnano.2011.139.

[17] Y. Cui, Q. Wei, H. Park, and C. M. Lieber. "Nanowire Nanosensors for Highly Sensitive and Selective Detection of Biological and Chemical Species". In: *Science* 293 (2001), pp. 1289–1292. DOI: 10.1126/science.1062711.

[18] A. C. Bleszynski, F. A. Zwanenburg, R. M. Westervelt, A. L. Roest, E. P. A. M. Bakkers, and L. P. Kouwenhoven. "Scanned Probe Imaging of Quantum Dots inside InAs Nanowires". In: *Nano Lett.* 7 (2007), pp. 2559–2562. DOI: 10.1021/nl0621037.

[19] W.G. Schmidt, S. Wippermann, S. Sanna, M. Babilon, N.J. Vollmers, and U. Gerstmann. "In-Si(111)(4x1)/(8x2) nanowires: Electron transport, entropy, and metal-insulator transition". In: *Phys. Status Solidi B* 249.2 (2012), pp. 343–359. DOI: 10.1002/pssb.201100457.

[20] W. Hafez, W. Snodgrass, and M. Feng. "12.5 nm base pseudomorphic heterojunction bipolar transistors achieving f_T = 710 GHz and f_{MAX} = 340 GHz". In: *Appl. Phys. Lett.* 87.25, 252109 (2005), p. 252109. DOI: 10.1063/1.2149510.

[21] J.B. Hacker, J. Bergman, G. Nagy, G. Sullivan, C. Kadow, Heng-Kuang Lin, A.C. Gossard, M. Rodwell, and B. Brar. "An ultra-low power InAs/AlSb HEMT Ka-band low-noise amplifier". In: *IEEE Microwave Wireless Compon. Lett.* 14.4 (2004), pp. 156 – 158. ISSN: 1531-1309. DOI: 10.1109/LMWC.2004.827132.

[22] Shadi A. Dayeh, Edward T. Yu, and Deli Wang. "Transport Coefficients of InAs Nanowires as a Function of Diameter". In: *Small* 5.1 (2009), pp. 77–81. ISSN: 1613-6829. DOI: 10.1002/smll.200800969.

[23] A. A. Talin, F. Léonard, A. M. Katzenmeyer, B. S. Swartzentruber, S. T. Picraux, M. E. Toimil-Molares, J. G. Cederberg, X. Wang, S. D. Hersee, and A. Rishinaramangalum. "Transport characterization in nanowires using an electrical nanoprobe". In: *Semicond. Sci. Technol.* 25.2 (2010), p. 024015. DOI: 10.1088/0268-1242/25/2/024015.

[24] M. D. Schroer and J. R. Petta. "Correlating the Nanostructure and Electronic Properties of InAs Nanowires". In: *Nano Lett.* 10.5 (2010), pp. 1618–1622. DOI: 10.1021/nl904053j.

[25] Y.-B. Wang, L.-F. Wang, H.J. Joyce, Q. Gao, X.-Z. Liao, Y.-W. Mai, H.H. Tan, J. Zou, H.-J. Ringer S.P.and Gao, and C. Jagadish. "Super deformability and young's modulus of GaAs nanowires". In: *Adv. Mater.* 23.11 (2011), pp. 1356–1360. DOI: 10.1002/adma.201004122.

[26] C. T. Sun and Haitao Zhang. "Size-dependent elastic moduli of platelike nanomaterials". In: *J. Appl. Phys.* 93 (2003), pp. 1212–1218. DOI: 10.1063/1.1530365.

[27] H. Liang, M. Upmanyu, and H. Huang. "Size-dependent elasticity of nanowires: Nonlinear effects". In: *Phys. Rev. B* 71 (2005), 241403(R). DOI: 10.1103/PhysRevB.71.241403.

[28] J. Wang, Q.-A. Huang, and H. Yu. "Size and temperature dependence of Young's modulus of a silicon nano-plate". In: *J. Phys. D: Appl. Phys.* 41.16 (2008), p. 165406. DOI: 10.1088/0022-3727/41/16/165406.

[29] C. Q. Sun, B. K. Tay, X. T. Zeng, S. Li, T. P. Chen, Ji Zhou, H. L. Bai, and E. Y. Jiang. "Bond-order-bond-length-bond-strength (bond-OLS) correlation mechanism for shape-and-size dependence of a nanosolid". In: *J. Phys.: Condens. Matter.* 14 (2002), pp. 7781–7795. DOI: 10.1088/0953-8984/14/34/301.

[30] L. G. Zhou and Hanchen Huang. "Are surfaces softer or stiffer?" In: *Appl. Phys. Lett.* 84 (2004), pp. 1940–1942. DOI: 10.1063/1.1682698.

[31] J. He and C. Lilley. "The finite element absolute nodal coordinate formulation incorporated with surface stress effect to model elastic bending nanowires in large deformation". In: *Comput. Mech.* 44 (3 2009), pp. 395–403. ISSN: 0178-7675. DOI: 10.1007/s00466-009-0380-9.

[32] C.-Y. Nam, P. Jaroenapibal, D. Tham, D. E. Luzzi, S. Evoy, and J. E. Fischer. "Diameter-Dependent Elastical Properties of GaN Nanowires". In: *Nano Lett.* 6 (2006), pp. 153–158. DOI: 10.1021/nl051860m.

[33] M. Lexholm, I. Karlsson, F. Boxberg, and D. Hessman. "Optical determination of Young's modulus of InAs nanowires". In: *Appl. Phys. Lett.* 95 (2009), No. 113103. DOI: 10.1063/1.3225150.

[34] C. Q. Chen, Y. Shi, Y. S. Zhang, J. Zhu, and Y. J. Yan. "Size Dependance of Young's Modulus in ZnO Nanowires". In: *Phys. Rev. Lett.* 96 (2006), No. 075505. DOI: 10.1103/PhysRevLett.96.075505.

[35] E. P. S. Tan, Y. Zhu, T. Yu, L. Dai, C. H. Sow, V. B. C. Tan, and C. T. Lim. "Crystallinity and surface effects on Young's modulus of CuO nanowires". In: *Appl. Phys. Lett.* 90.16 (2007), p. 163112. DOI: 10.1063/1.2723654.

[36] K. H. Liu, W. L. Wang, Z. Xu, L. Liao, X. D. Bai, and E. G. Wang. "In situ probing mechanical properties of individual tungsten oxide nanowires girectly grown on tungsten tips inside transmission electron microscope". In: *Appl. Phys. Lett.* 89 (2006), No. 221908. DOI: 10.1063/1.2397547.

[37] M. J. Bucknum and E. A. Castro. "Towards a microscopic theory of the modulus of elasticity in crystalline covalent materials and a survey of potential superhard materials". In: *J. Math. Chem.* 38 (1 2005), pp. 27–42. ISSN: 0259-9791. DOI: 10.1007/s10910-005-4528-3.

[38] E.H. Dill. *Continuum mechanics: elasticity, plasticity, viscoelasticity*. CRC Press, 2007. ISBN: 9780849397790.

[39] E.N. Dvorkin and M.B. Goldschmit. *Nonlinear continua*. Computational fluid and solid mechanics. Springer-Verlag, Berlin Heidelberg, 2006. ISBN: 9783540249856.

[40] C. Wang and C. Truesdell. *Introduction to rational elasticity*. Mechanics of continua. Noordhoff International Pub. Co., 1973. ISBN: 9789001937102.

[41] L. D. Landau and E. M. Lifshitz. *Theory of Elasticity (Teoriya Uprugosti)*. Ed. by E. M. Lifshitz, A. M. Kosevich, and L. P. Pitaevskyi. Vol. 7. Theoretical Physics. Nauka, Moscow, 1987.

[42] L Meirovitch. *Fundamentals of Vibrations*. McGraw-Hill, New York, 2001.

[43] L. Meirovich. *Element of Vibration Analysis*. 2nd. McGraw-Hill, New York, 1986.

[44] Z. Wang, F. Gao, X. Zu, J. Li, and W. J. Weber. "Mechanical Properties of GaN Nanowires". In: *Handbook of Nanophysics: Nanotubes and Nanowires*. Ed. by K. D. Sattler. 24. CRC Press, Boca Raton, 2010.

[45] D. C. Tsui. "Observation of Surface Bound State and Two-Dimensional Energy Band by Electron Tunneling". In: *Phys. Rev. Lett.* 24 (7 1970), pp. 303–306. DOI: 10.1103/PhysRevLett.24.303.

[46] L. Olsson, C. B. M. Andersson, M. C. Hakansson, J. Kanski, L. Ilver, and U. O. Karlsson. "Charge Accumulation at InAs Surfaces". In: *Phys. Rev. Lett.* 76 (1996), pp. 3626–3629. DOI: 10.1103/PhysRevLett.76.3626.

[47] H. Reisinger, H. Schaber, and R. E. Doezema. "Magnetoconductance study of accumulation layers on n – InAs". In: *Phys. Rev. B* 24 (10 1981), pp. 5960–5969. DOI: 10.1103/PhysRevB.24.5960.

[48] J D Grange, E H C Parker, and R M King. "Relationship of MBE growth parameters with the electrical properties of thin (100) InAs epilayers". In: *J. Phys. D: Appl. Phys.* 12.9 (1979), p. 1601. DOI: 10.1088/0022-3727/12/9/023.

[49] C. Affentauschegg and H. H. Wieder. "Properties of InAs/InAlAs heterostructures". In: *Semicond. Sci. Technol.* 16.8 (2001), p. 708. DOI: 10.1088/0268-1242/16/8/313.

[50] W. Monch. "Virtual gap states and Fermi level pinning by adsorbates at semiconductor surfaces". In: *J. Vac. Sci. Technol. B* 4.4 (1986), pp. 1085–1090. DOI: 10.1116/1.583548.

[51] K. Smit, L. Koenders, and W. Monch. "Adsorption of chlorine and oxygen on cleaved InAs(110) surfaces: Raman spectroscopy, photoemission spectroscopy, and Kelvin probe measurements". In: *PROCEEDINGS OF THE 16th ANNUAL CONFERENCE ON THE PHYSICS AND CHEMISTRY OF SEMICONDUCTOR INTERFACES*. Vol. 7. 4. BOZEMAN, MONTANA, USA: AVS, 1989, pp. 888–893. DOI: 10.1116/1.584619.

[52] V. Bessolov and M. Lebedev. "Chalcogenide passivation of III-V semiconductor surfaces". In: *Semiconductors* 32 (11 1998), pp. 1141–1156. ISSN: 1063-7826. DOI: 10.1134/1.1187580.

[53] M. Shur. *Handbook Series on Semiconductor Parameters*. Vol. 1. World Scientific Publishing Company, Incorporated, 1995. ISBN: 9789810214203.

[54] Z. Zanolli, M.-E. Pistol, L. E. Fröberg, and L. Samuelson. "Quantum-confinement effects in InAs-InP core-shell nanowires". In: *J. Phys.: Condens. Matter* 19.29 (2007), p. 295219. DOI: 10.1088/0953-8984/19/29/295219.

[55] C.-Y. Yeh, S.-H. Wei, and A. Zunger. "Relationships between the band gaps of the zinc-blende and wurtzite modifications of semiconductors". In: *Phys. Rev. B* 50 (4 1994), pp. 2715–2718. DOI: 10.1103/PhysRevB.50.2715.

[56] Z. Zanolli, F. Fuchs, J. Furthmüller, U. von Barth, and F. Bechstedt. "Model GW band structure of InAs and GaAs in the wurtzite phase". In: *Phys. Rev. B* 75 (24 2007), p. 245121. DOI: 10.1103/PhysRevB.75.245121.

[57] A. De and C. E. Pryor. "Predicted band structures of III-V semiconductors in the wurtzite phase". In: *Phys. Rev. B* 81 (15 2010), p. 155210. DOI: 10.1103/PhysRevB.81.155210.

[58] Z. M. Fang, K. Y. Ma, D. H. Jaw, R. M. Cohen, and G. B. Stringfellow. "Photoluminescence of InSb, InAs, and InAsSb grown by organometallic vapor phase epitaxy". In: *J. Appl. Phys.* 67.11 (1990), pp. 7034–7039. DOI: 10.1063/1.345050.

[59] M. P. Persson and H. Q. Xu. "Electronic structure of [100]-oriented free-standing InAs and InP nanowires with square and rectangular cross sections". In: *Phys. Rev. B* 73 (12 2006), p. 125346. DOI: 10.1103/PhysRevB.73.125346.

[60] E. Lind, M.P. Persson, Y.-M. Niquet, and L.-E. Wernersson. "Band Structure Effects on the Scaling Properties of [111] InAs Nanowire MOSFETs". In: *IEEE Trans. Electron Devices* 56.2 (2009), pp. 201 –205. ISSN: 0018-9383. DOI: 10.1109/TED.2008.2010587.

[61] K. Alam and R.N. Sajjad. "Electronic Properties and Orientation-Dependent Performance of InAs Nanowire Transistors". In: *IEEE Trans. Electron Devices* 57.11 (2010), pp. 2880 –2885. ISSN: 0018-9383. DOI: 10.1109/TED.2010.2066569.

[62] J.-M. Jancu, R. Scholz, F. Beltram, and F. Bassani. "Empirical $spds^*$ tight-binding calculation for cubic semiconductors: General method and material parameters". In: *Phys. Rev. B* 57 (11 1998), pp. 6493–6507. DOI: 10.1103/PhysRevB.57.6493.

[63] F. Wang, H. Yu, S. Jeong, J. M. Pietryga, J. A. Hollingsworth, P. C. Gibbons, and W. E. Buhro. "The Scaling of the Effective Band Gaps in InAs Quantum Dots and Wires". In: *ACS Nano* 2.9 (2008), pp. 1903–1913. DOI: 10.1021/nn800356z.

[64] X. Zhou, S. A. Dayeh, D. Aplin, D. Wang, and E. T. Yu. "Direct observation of ballistic and drift carrier transport regimes in InAs nanowires". In: *Appl. Phys. Lett.* 89.5 (2006), p. 053113. DOI: 10.1063/1.2236589.

[65] A. Mavrokefalos, M.T. Pertes, S. Saha, F. Zhou, and L. Shi. "Combined thermoelectric and structure characterizations of patterned nanowires". In: 2006, pp. 234–237. DOI: 10.1109/ICT.2006.331358.

[66] D. L. Rode. "Electron Transport in InSb, InAs, and InP". In: *Phys. Rev. B* 3 (10 1971), pp. 3287–3299. DOI: 10.1103/PhysRevB.3.3287.

[67] P. D. Wang, S. N. Holmes, T. Le, R. A. Stradling, I. T. Ferguson, and A. G. de Oliveira. "Electrical and magneto-optical of MBE InAs on GaAs". In: *Semicond. Sci. Technol.* 7.6 (1992), p. 767. DOI: 10.1088/0268-1242/7/6/008.

[68] G. Moschetti, H. Zhao, P. A . Nilsson, S. Wang, A. Kalabukhov, G. Dambrine, S. Bollaert, L. Desplanque, X. Wallart, and J. Grahn. "Anisotropic transport properties in InAs/AlSb heterostructures". In: *Appl. Phys. Lett.* 97.24, 243510 (2010), p. 243510. DOI: 10.1063/1.3527971.

[69] C.-Y. Yeh, Z. W. Lu, S. Froyen, and A. Zunger. "Zinc-blende Wurtzite polytypism in semiconductors". In: *Phys. Rev. B* 46 (16 1992), pp. 10086–10097. DOI: 10.1103/PhysRevB.46.10086.

[70] M. Koguchi, H. Kakibayashi, M. Yazawa, K. Hiruma, and T. Katsuyama. "Crystal Structure Change of GaAs and InAs Whiskers from Zinc-Blende to Wurtzite Type". In: *Jpn. J. Appl. Phys.* 31 (1992), pp. 2061–2065. DOI: 10.1143/JJAP.31.2061.

[71] P. Caroff, K. Dick, J. Johansson, M. Messing, K. Deppert, and L. Samuelson. "Controlled polytypic and twin-plane superlattices in III-V nanowires". In: *Nat. Nanotechnol.* 4 (2009), pp. 50–55. DOI: 10.1038/NNANO.2008.359.

[72] M. Murayama and T. Nakayama. "Chemical trend of band offsets at wurtzite/zinc-blende heterocrystalline semiconductor interfaces". In: *Phys. Rev. B* 49 (7 1994), pp. 4710–4724. DOI: 10.1103/PhysRevB.49.4710.

[73] S.A. Dayeh, D. Susac, Peng Chen, Yi Jing, K.L. Kavanagh, S.S. Lau, E.T. Yu, and Deli Wang. "Optimal Control over the InAs Nanowire Growth for System Integration and their Structural and Transport Properties". In: *Nanotechnology, 2008. NANO '08. 8th IEEE Conference on*. 2008, pp. 576 –579. DOI: 10.1109/NANO.2008.170.

[74] P.G. Slade. *Electrical Contacts: Principles and Applications*. Electrical Engineering and Electronics. CRC Press, New York, 1999. ISBN: 9780824719340.

[75] R.S. Timsit. "Electrical contact resistance: properties of stationary interfaces". In: *IEEE Trans. Comp. Packag. Technol.* 22.1 (1999), pp. 85 –98. ISSN: 1521-3331. DOI: 10.1109/6144.759357.

[76] R.S. Timsit. "Electrical Conduction Through Small Contact Spots". In: *IEEE Trans. Comp. Packag. Technol.* 29.4 (2006), pp. 727 –734. ISSN: 1521-3331. DOI: 10.1109/TCAPT.2006.885930.

[77] F.F.Y. Wang. *Introduction to solid state electronics*. Elsevier Science, Amsterdam, 1980. ISBN: 9780444852373.

[78] M. Balkanski and R.F. Wallis. *Semiconductor Physics and Applications*. Series on Semiconductor Science and Technology. Oxford University Press, 2000. ISBN: 9780198517412.

[79] V. Migunov. "Transport properties of InAs Nanowhiskers". MA thesis. University of Duisburg-Essen, 2009.

[80] F. Glas, G. Patriarche, and J. C. Harmand. "Growth, structure and phase transitions of epitaxial nanowires of III-V semiconductors". In: *J. Phys: Conf. Ser.* 209 (2010), p. 012002. DOI: 10.1088/1742-6596/209/1/012002.

[81] M.T. Borgström, G. Immink, B. Ketelaars, R. Algra, and E.P.A.M. Bakkers. "Synergetic nanowire growth". In: *Nat. Nanotechnol.* 2.9 (2007), pp. 541–544. DOI: 10.1038/nnano.2007.263.

[82] I. M. Watt. *The principals and practice of electron microscopy*. 2nd ed. Cambridge University Press, 1997.

[83] David B. Williams and C. Barry Carter. *Transmission Electron Microscopy: A Textbook for Material Science*. Plenum Press, New York, 1996.

[84] J. W. Edington. *Practical electron microscopy in material science*. N. V. Philips, Eindhoven, 1976.

[85] P.A. Midgley and R.E. Dunin-Borkowski. "Electron tomography and holography in materials science". In: *Nat. Mater.* 8.4 (2009), pp. 271–280. DOI: 10.1038/nmat2406.

[86] Zi-An Li, Ch. Möller, V. Migunov, M. Spasova, M. Farle, A. Lysov, Ch. Gutsche, I. Regolin, W. Post, F.-J. Tegude, and P. Ercius. "Planar-defect characteristics and cross-sections of ⟨001⟩, ⟨112⟩ and ⟨111⟩ InAs nanowires". In: *J. Appl. Phys.* 109 (2011), p. 114320. DOI: 10.1063/1.3592186.

[87] A. C. Kak and M. Slaney. *Principles of Computerized Tomographic Imaging*. IEEE Press, New York, 1988.

[88] Christoph Koch. "Determination of core structure periodicity and point defect density along dislocations". PhD thesis. Arizona State University, 2002.

[89] *SPM systems for in-situ TEM*. Chalmers Science Park, Goeteborg, Sweden: Nanofactory Instruments AB, 2012.

[90] A. Nafari, D. Karlen, C. Rusu, K. Svensson, H. Olin, and P. Enoksson. "MEMS Sensor for In Situ TEM Atomic Force Microscopy". In: *JMEMS* 17 (2008), pp. 328 –333. DOI: 10.1109/JMEMS.2007.912714.

[91] M. Mukhametshin. "In situ transmission electron microscopy studies of mechanical properties of InAs nanowires". MA thesis. University of Duisburg-Essen, 2011.

[92] Thomas B. Jones. *Electromechanics of Particles*. Cambridge University Press, 1995.

[93] S. Raychaudhuri, S. A. Dayeh, D. Wang, and E. T. Yu. "Precise Semiconductor Nanowire Placement Through Dielectrophoresis". In: *Nano Lett.* 9 (2009), pp. 2260–2266. DOI: 10.1021/nl900423g.

[94] H. Lichte. "Electron image plane off-axis holography of atomic structures". In: *Adv. Opt. Electron Microsc.* 12 (1991), pp. 25–91.

[95] A. Tonomura. "Electron-holographic interference microscopy". In: *Adv. Phys.* 41 (1992), pp. 59–103. DOI: 10.1080/00018739200101473.

[96] M. R. McCartney and D. J. Smith. "Electron Holography: Phase Imaging with Nanometer Resolution". In: *Annu. Rev. Mater. Res.* 37 (2007), pp. 729–767. DOI: 10.1146/annurev.matsci.37.052506.084219.

[97] H. Lichte and M. Lehmann. "Electron holography–basics and applications". In: *Rep. Prog. Phys.* 71 (2008), p. 016102. DOI: 10.1088/0034-4885/71/1/016102.

[98] R.W. Hamming. *Digital Filters*. Dover Publications, Mineola, 1997. ISBN: 9780486650883.

[99] *DigitalMicrograph^{TM}: Image Acquisition and Processing Software*. Gatan Inc. 2007. http://www.gatan.com/imaging/dig_micrograph.php.

[100] M. de Berg, O. Cheong, M. van Kreveld, and M. Overmars. *Computational Geometry: Algorithms and Applications*. 3d. Springer, Berlin, 2008.

[101] R. S. Wagner and W. C. Ellis. "VAPOR-LIQUID-SOLID MECHANISM OF SINGLE CRYSTAL GROWTH". In: *Appl. Phys. Lett.* 4.5 (1964), pp. 89–90. DOI: 10.1063/1.1753975.

[102] D. Kriegner, Ch. Panse, B. Mandl, K. A. Dick, M. Keplinger, J. M. Persson, P. Caroff, D. Ercolani, L. Sorba, F. Bechstedt, J. Stangl, and G. Bauer. "Unit crell structure of cristal politypes in InAs and InSb nanowires". In: *Nano Lett.* 11 (2011), pp. 1483–1489. DOI: 10.1021/nl1041512.

[103] H. Gottschalk, G. Patzer, and H. Alexander. "STACKING FAULT ENERGY AND IONICITY OF CUBIC III-V COMPOUNDS." In: *Phys. Status Solidi A* 45.1 (1978), pp. 207–217. DOI: 10.1002/pssa.2210450125.

[104] F.M. Davidson, D.C. Lee, D.D. Fanfair, and B.A. Korgel. "Lamellar twinning in semiconductor nanowires". In: *J. Phys. Chem. C* 111.7 (2007), pp. 2929–2935. DOI: 10.1021/jp0672205.

[105] F. Glas, J.-C. Harmand, and G. Patriarche. "Why Does Wurtzite Form in Nanowires of III-V Zinc Blende Semiconductors?" In: *Phys. Rev. Lett.* 99 (14 2007), p. 146101. DOI: 10.1103/PhysRevLett.99.146101.

[106] A. H. Carim, K.-K. Lew, and J. M. Redwing. "Bicrystalline Silicon Nanowires". In: *Adv. Mater.* 13.19 (2001), pp. 1489–1491. ISSN: 1521-4095. DOI: 10.1002/1521-4095(200110)13:19<1489::AID-ADMA1489>3.0.CO;2-E.

[107] D. B. Holt. "Plolarity reversal and symmetry in semiconducting compounds with the sphalerite and wiurtzite structure." In: *J. Matter. Sci.* 19 (1984), pp. 439–446. DOI: 10.1007/BF00553567.

[108] S. B. Austerman and W. G. Gehman. "The inversion twin: Prototype in beryllium oxide". In: *J. Matter. Sci.* 1 (1966), pp. 249–260. DOI: 10.1007/BF00550173.

[109] D. Cohen, S. McKernan, and C. B. Carter. "Characterization of the absolute crystal polarity across twin boundaries in gallium phosphide using convergent-beam electron diffraction". In: *Microsc. Microanal.* 5 (1999), pp. 173–186. DOI: 10.1017/S1431927699000124.

[110] J. Johanson, L. S. Karlsson, C. P. T. Svensson, Th. Martensson, B. A. Wacaser, K. Deppert, L. Samuelsson, and W. Seifert. "The structure of ⟨111⟩ B oriented GaP nanowires". In: *J. Cryst. Growth* 298 (2007), pp. 635–639. DOI: 10.1016/j.jcrysgro.2006.10.175.

[111] K. Tillmann, L. Houben, and A. Thust. "Atomic-resolution imaging of lattice imperfections in semiconductors by combined aberration-corrected HRTEM and exit-plane wavefunction retrieval". In: *Philos. Mag.* 86 (2006), pp. 4589–4606. DOI: 10.1080/14786430600675763.

[112] R. Kilaas. "Optimal and near-optimal filters in high-resolution electron microscopy". In: *J. Microscopy* 190.1-2 (1998), pp. 45–51. ISSN: 1365-2818. DOI: 10.1046/j.1365-2818.1998.3070861.x.

[113] A. Mikkelsen, N. Sköld, L. Ouattara, M. Borgström, J.N. Andersen, L. Samuelson, W. Seifert, and E. Lundgren. "Direct imaging of the atomic structure inside a nanowire by scanning tunnelling microscopy". In: *Nat. Mater.* 3.8 (2004), pp. 519–523. DOI: 10.1038/nmat1164.

[114] R. E. Algra, M. A. Verheijen, L.-F. Feiner, G. G. W. Immink, R. Theissmann, W. J. P. van Enckevort, E. Vlieg, and E. P. A. M. Bakkers. "Paired Twins and {11-2} Morphology in GaP Nanowires". In: *Nano Lett.* 10.7 (2010), pp. 2349–2356. DOI: 10.1021/nl1000136.

[115] S. S. Verbridge, D. F. Shapiro, H. G. Craighead, and J. M. Parpia. "Macroscopic Tuning of Nanomechanics: Substrate Bending for Reversible Control of Frequency and Quality Factor of Nanostring Resonators". In: *Nano Lett.* 7.6 (2007), pp. 1728–1735. DOI: 10.1021/nl070716t.

[116] K. Jacobi, L. Geelhaar, and J. Marquez. "Structure of high-index GaAs surfaces - the discovery of the stable GaAs (2 5 11) surface". In: *Appl. Phys. A: Mater. Sci. Process.* 75 (1 2002), pp. 113–127. ISSN: 0947-8396. DOI: 10.1007/s003390101060.

[117] *COMSOL Multiphysics®*. COMSOL Group. 2012. http://www.comsol.com/products/multiphysics/.

[118] "Indium arsenide (InAs)". In: *Semiconductors. Group IV Elements, IV-IV and III-V Compounds. Part a - Lattice Properties*. Ed. by O. Madelung, U. Roessler, and M. Schulz. Vol. 41A1a. Springer-Verlag, 2001. DOI: 10.1007/10551045_150.

[119] A. A. Talin, F. Léonard, B. S. Swartzentruber, X. Wang, and S. D. Hersee. "Unusually Strong Space-Charge-Limited Current in Thin Wires". In: *Phys. Rev. Lett.* 101 (7 2008), p. 076802. DOI: 10.1103/PhysRevLett.101.076802.

[120] M. Scheffler, S. Nadj-Perge, L. P. Kouwenhoven, M.s T. Borgström, and E. P. A. M. Bakkers. "Diameter-dependent conductance of InAs nanowires". In: *J. Appl. Phys.* 106.12 (2009), p. 124303. DOI: 10.1063/1.3270259.

[121] C. Thelander, K. A. Dick, M. T. Borgström, L. E. Fröberg, P. Caroff, H. A. Nilsson, and L. Samuelson. "The electrical and structural properties of n-type InAs nanowires grown from metal-organic precursors". In: *Nanotechnology* 21.20 (2010), p. 205703. DOI: 10.1088/0957-4484/21/20/205703.

[122] E. Burstein and S. Lundqvist. *Tunneling phenomena in solids: lectures*. Plenum Press, New York, 1969.

[123] C. H. Champbess and R. P. Chasmar. "The Transverse Magnetoresistance Effect in Indium Arsenide". In: *Journal of Electronics and Control* 3.5 (1957), pp. 494–499. DOI: 10.1080/00207215708937110.

[124] H. Weiss. "Die magnetische Widerstandsänderung in InAs". In: *Z. Naturforsch.* 12a (1957), p. 80.

[125] S. Dhara, H. S. Solanki, V. Singh, A. Narayanan, P. Chaudhari, M.h Gokhale, A. Bhattacharya, and M. M. Deshmukh. "Magnetotransport properties of individual InAs nanowires". In: *Phys. Rev. B* 79 (12 2009), p. 121311. DOI: 10.1103/PhysRevB.79.121311.

[126] F. J. Garcia De Abajo. "Momentum transfer to small particles by passing electron beams". In: *Phys. Rev. B* 70.11 (2004), p. 115422. DOI: 10.1103/PhysRevB.70.115422.

[127] "Part a - Lattice Properties". In: *Semiconductors. Group IV Elements, IV-IV and III-V Compounds. Part b - Electronic, Transport, Optical and Other Properties*. Ed. by O. Madelung, U. Roessler, and M. Schulz. Vol. 41A1b. Springer-Verlag, 2001. DOI: 10.1007/b60136.

[128] "Part b - Electronic, Transport, Optical and Other Properties". In: *Semiconductors. Group IV Elements, IV-IV and III-V Compounds. Part b - Electronic, Transport, Optical and Other Properties*. Ed. by O. Madelung, U. Roessler, and M. Schulz. Vol. 41A1b. Springer-Verlag, 2001. DOI: 10.1007/b80447.

[129] *Semiconductors on NSM*. Ioffe Physical Technical Institute. http://www.ioffe.rssi.ru/SVA/NSM/Semicond/.

[130] K. Jensen, J. Weldon, H. Garcia, and A. Zettl. "Nanotube Radio". In: *Nano Lett.* 7.11 (2007), pp. 3508–3511. DOI: 10.1021/nl0721113.

[131] A. K. Hüttel, G. A. Steele, B. Witkamp, M.o Poot, L. P. Kouwenhoven, and H. S. J. van der Zant. "Carbon Nanotubes as Ultrahigh Quality Factor Mechanical Resonators". In: *Nano Lett.* 9.7 (2009), pp. 2547–2552. DOI: 10.1021/nl900612h.

[132] Anne-Sophie Lucier. "Preparation and Characterization of Tungsten Tips Suitable for Molecular Electronics Studies". MA thesis. McGill University, Montreal, Canada, 2004.

[133] C. T. Koch. http://www.christophtkoch.com/stem/index_formats.html.

[134] E. Hilner, U. Hakanson, L. E. Froöberg, M. Karlsson, P. Kratzer, E. Lundgren, L. Samuelson, and A. Mikkelsen. "Direct Atomic Scale Imaging of III-V Nanowire Surfaces". In: *Nano Lett.* 8.11 (2008), pp. 3978–3982. DOI: 10.1021/nl802500d.

[135] A. Taguchi and K. Kanisawa. "Stable reconstruction and adsorbates of InAs(111)A surface". In: *Appl. Surf. Sci.* 252.15 (2006), pp. 5263–5266. ISSN: 0169-4332. DOI: 10.1016/j.apsusc.2005.12.072.

[136] E. Hilner, E. Lundgren, and A. Mikkelsen. "Surface structure and morphology of InAs (111)B with/without gold nanoparticles annealed under arsenic or atomic hydrogen flux". In: *Surf. Sci.* 604.3-4 (2010), pp. 354–360. ISSN: 0039-6028. DOI: 10.1016/j.susc.2009.11.029.

[137] D. J. Chadi. "(110) surface atomic structures of covalent and ionic semiconductors". In: *Phys. Rev. B* 19 (4 1979), pp. 2074–2082. DOI: 10.1103/PhysRevB.19.2074.

[138] C. B. Duke. "Semiconductor Surface Reconstruction: The Structural Chemistry of Two-Dimensional Surface Compounds". In: *Chem. Rev.* 96.4 (1996), pp. 1237–1260. DOI: 10.1021/cr950212s.

[139] W. A. Harrison. "Theory of polar semiconductor surfaces". In: *J Vac. Sci. Technol.* 16.5 (1979), pp. 1492–1496. DOI: 10.1116/1.570229.

[140] N. Sibirev, M. Timofeeva, A. Bol'shakov, M. Nazarenko, and V. Dubrovskii. "Surface energy and crystal structure of nanowhiskers of III-V semiconductor compounds". In: *Phys. Solid State* 52 (7 2010), pp. 1531–1538. ISSN: 1063-7834. DOI: 10.1134/S1063783410070309.

Acknowledgements

I would like to thank those people who have helped me during my PhD study.

First of all, many thanks to Prof. Dr. Michael Farle for his supervision of my work, for many hours spent in discussions, for financial and other kind of support. I would like to thank Professor Farle as a leader of the group for creating a friendly working atmosphere, which encourages interest in science and contribute to professional development. It was my pleasure to be a part of his research group and work with him.

I am very grateful to Dr. Marina Spasova for the attention she paid to my work, for the supervision, support, great ideas and hours of discussions. I am very thankful for the care she took over me during the PhD time.

I highly appreciate Dr. Zi-An Li for the work on structural investigation of InAs nanowires, for the experience he shared with me, for the useful discussions. I am very grateful, since I learned a lot of TEM methods from him.

Many thanks to Horst Zähres, without whose ”golden hands” and brilliant technical solutions this work could not be done.

A special thanks to Dr. Ralf Theissman for amazing TEM lectures and practice exercises, for fruitful discussions and help to establish first STM-TEM experiments.

I highly appreciate the work and help of Marat Mukhametshin on DEP and AFM-TEM experiments.

Many thanks to Christina Möller for the work on 3D-tomography of InAs nanowires.

A special thanks to Dieter Schädel for the technical help.

Many thanks to Dr. Miguel Comesaña-Hermo, for his help in chemistry lab, for discussions and support.

I am grateful to Dr. Fedor Mushenok for help with finite element simulations.

Advice given by Prof. Mehmet Acet has been a great help in writing my thesis.

Special thanks to Dr. Florian Römer, who helped a lot in FMR-lab during Hall sensor calibrations.

I appreciate Dr. Detlef Spoddig for his help with the focused ion beam experiments.

Thanks to Dr. Oliver Prost, Christian Wirtz and Nathalie Reckers for help with SEM measurements and ex-situ transport characterizations (not included in the thesis).

I am grateful to the members of group of Prof. Dr. Franz-Josef Tegude: Andrey Lysov,

Christoph Gutsche, Ingo Regolin, Dr. Werner Prost for the supply of InAs nanowires and discussions.

I am thankful to Johannes Schaffert, who shared his experience in STM with me.

I am truly indebted and thankful to Prof. Dr. Rafal Dunin-Borkowski from Ernst Ruska-Centre, Jülich for fruitful and very helpful discussions and organization of the holography and HR-STEM experiments.

Many thanks to Dr. Takeshi Kasama and Dr.

I am very grateful to András Kovács for great help with HR-STEM experiment on the InAs nanowires and discussion of the results.

I would like to thank Prof. Dr. Erik P. A. M. Bakkers and Dr, Sébastien Plissard from Eindhoven University of Technology who supplied me with InAs nanowires.

Thanks to Nerio Fontaiña-Troitiño from University of Vigo for synthesis of ZnO nanowires, even though the study of these wires were not included in the thesis.

I am grateful to Dr. Thomas Mühl and his colleagues from Institute for Solid State and Materials Research, Dresden for preparation of Fe-filled carbon nanotubes and discussion, although the related study is not included in the thesis.

I am obliged to many of my colleagues from group of prof. Michael Farle and University of Duisburg-Essen, that are not named above. I highly appreciate their help and discussions.

Special thanks and sincere appreciation to Helga Mundt, Sabina Gruba and Rosa Abts who were in charge of administrative work and helped a lot with solving different (not only science related) problems.

I would like to thank Deutsche Forschungsgemeinschaft (DFG) for financial support in frame of project SFB 445.

Special thanks for University of Duisburg-Essen for the infrastructure I have used during my PhD.

The last but not the least, I owe sincere and earnest thankfulness to my family and friends. There is no need at all to list their contribution in my work since their support is invaluable. Here are their names:

My parents Evgeny and Elena Migunov(a);

My wife Evgenya Koptseva and here family Alexey and Svetlana Koptsev(a);

My brother Andrey Migunov and his family Irina Mysina, Sophia and Anna;

My Russian friends Ilona Abanshina, Kamil Akmaldinov, Stephan Obraztsov, Maxim Rybin, Ilya Semenov;

My former colleagues and friends Prof. Dr. Nikolay Perov, Dr. Valeriya Rodionova (Samsonova), Dr.

Our ”international Finkenkrug community” (without titles) Seda Aksoy, Yuri Aleksandrov (aka Saban Atakan), Igor Barsukov, Miguel Comesaña-Hermo, Ruzhica Djenadic, Yu Fu, Sara Liebana-Viñas, Egor Lobastov, Katharina Ollefs, Christian Schöppner;

And some more (without titles again): Denis Alyshev, Risako and Thomas Klimek, Irina Rod, Marina Spasova, Sergey Tikhonov, Anastasiya Trunova.

List of own publications and conference contributions

Publications

1. E. A. Gan'shina, N. S. Perov, S. Phonghirun, V. E. Migunov, Yu. E. Kalinin, and A. V. Sitnikov. "Enhancement of Magneto-Optical Response in Nanocomposite-Hydrogenated Amorphous Silicon Multilayers". In: *Bulletin of the Russian Academy of Sciences: Physics* 72 (2008), pp. 1379-1381. DOI: 10.3103/S1062873808100201.

2. Zi-An Li, Christina Möller, Vadim Migunov, Marina Spasova, Michael Farle, Andrey Lysov, Christoph Gutsche, Ingo Regolin, Werner Prost, Franz-Josef Tegude, and Peter Ercius. "Planar-defect characteristics and cross-sections of $\langle 001 \rangle$, $\langle 111 \rangle$, and $\langle 112 \rangle$ InAs nanowires". In: *Journal of Applied Physics* 109 (2011), 114320. DOI: 10.1063/1.3592186.

3. Vadim Migunov, Zi-An Li, Marina Spasova, and Michael Farle. "Electron transport in partially filled iron carbon nanotubes". In: *Solid State Phenomena* 190 (2012), pp 498-501. DOI: 10.4028/www.scientific.net/SSP.190.498.

4. Vadim Migunov, Zi-An Li, Christina Moller, Marina Spasova, Andrey Lysov, Ingo Regolin, Werner Prost, Franz-Josef Tegude, and Michael Farle. "Young's modulus of InAs nanowires". In press.

Selected conference contributions

- Talk at XIV International Scientific Conference for Students and Young Scientists "Lomonosov 2007", Moscow, Russia, "The modeling of drug transport in the arterial blood flow" (April 2007)

- Talk at XV International Scientific Conference for Students and Young Scientists "Lomonosov 2008", Moscow, Russia, "Magnetic Properties of Nanocomposite-Hydrogenated Amorphous Silicon Multilayers" (April 2008)

- Talk at DPG spring meeting 2010, Regensburg, Germany, ”Enhancement of Young’s modulus in InAs nanowires” (March 2010)
- Poster at Nanowire Growth Workshop 2010, Rome, Italy, ”Structural and Mechanical Properties of InAs Nanowires” (November 2010)
- Poster and mini-presentation at 22th Edgar Lüscher Seminar 2011, Klosters, Switzerland, ”Strain dependent transport in ZnO nanowires” (February 2011)
- Talk at Moscow International Symposium on Magnetism - MISM 2011, Moscow, Russia, ”Structural correlations of electron transport in iron filled carbon nanotubes” (August 2011)

Declaration of authenticity

I hereby declare that all materials presented in the thesis is my own work, otherwise rigorously cited and specifically acknowledged wherever adapted from different authors.

Vadim Migunov

Signature: Date: